

^{13}C -methyl formate: observations of a sample of high mass star-forming regions including Orion-KL and spectroscopic characterization¹

Cécile Favre

Department of Astronomy, University of Michigan, 500 Church St., Ann Arbor, MI 48109, USA;

cfavre@umich.edu

and

Miguel Carvajal

Dpto. Física Aplicada, Unidad Asociada CSIC, Facultad de Ciencias Experimentales, Universidad de Huelva, 21071, Spain

miguel.carvajal@dfa.uhu.es

and

David Field

Department of Physics and Astronomy, University of Aarhus, Ny Munkegade 120, 8000 Aarhus C, Denmark

and

Jes K. Jørgensen, Suzanne E. Bisschop

Centre for Star and Planet Formation, Niels Bohr Institute, University of Copenhagen, Juliane Maries Vej 30, 2100 Copenhagen Ø, Denmark

Natural History Museum of Denmark, University of Copenhagen, Øster Voldgade 5-7, 1350 Copenhagen K., Denmark

and

Nathalie Brouillet, Didier Despois, Alain Baudry

Univ. Bordeaux, LAB, UMR 5804, F-33270, Floirac, France

CNRS, LAB, UMR 5804, F-33270, Floirac, France

and

Isabelle Kleiner

Laboratoire Interuniversitaire des Systèmes Atmosphériques (LISA), CNRS, UMR 7583, Université de Paris-Est et Paris Diderot, 61, Av. du Général de Gaulle, 94010 Créteil Cedex, France

and

Edwin A. Bergin, Nathan R. Crockett, Justin L. Neill

Department of Astronomy, University of Michigan, 500 Church St., Ann Arbor, MI 48109, USA;
and

*Laurent Margulès, Thérèse R. Huet, Jean Demaison
Laboratoire de Physique des Lasers, Atomes et Molécules, UMR CNRS 8523, Université Lille I, 59655
Villeneuve d'Ascq Cedex, France*

ABSTRACT

We have surveyed a sample of massive star-forming regions located over a range of distances from the Galactic centre for methyl formate, HCOOCH_3 , and its isotopologues $\text{H}^{13}\text{COOCH}_3$ and $\text{HCOO}^{13}\text{CH}_3$. The observations were carried out with the APEX telescope in the frequency range 283.4–287.4 GHz. Based on the APEX observations, we report tentative detections of the ^{13}C -methyl formate isotopologue $\text{HCOO}^{13}\text{CH}_3$ towards the following four massive star-forming regions: Sgr B2(N-LMH), NGC 6334 IRS 1, W51 e2 and G19.61-0.23. In addition, we have used the 1 mm ALMA science verification observations of Orion-KL and confirm the detection of the ^{13}C -methyl formate species in Orion-KL and image its spatial distribution. Our analysis shows that the $^{12}\text{C}/^{13}\text{C}$ isotope ratio in methyl formate toward Orion-KL Compact Ridge and Hot Core-SW components (68.4 ± 10.1 and 71.4 ± 7.8 , respectively) are, for both the ^{13}C -methyl formate isotopologues, commensurate with the average $^{12}\text{C}/^{13}\text{C}$ ratio of CO derived toward Orion-KL. Likewise, regarding the other sources, our results are consistent with the $^{12}\text{C}/^{13}\text{C}$ in CO. We also report the spectroscopic characterization, which includes a complete partition function, of the complex $\text{H}^{13}\text{COOCH}_3$ and $\text{HCOO}^{13}\text{CH}_3$ species. New spectroscopic data for both isotopomers $\text{H}^{13}\text{COOCH}_3$ and $\text{HCOO}^{13}\text{CH}_3$, presented in this study, has made it possible to measure this fundamentally important isotope ratio in a large organic molecule for the first time.

Subject headings: line: identification — astrochemistry — ISM: abundances — techniques: spectroscopic — methods: laboratory: molecular — methods: data analysis

1. Introduction

Determination of elemental isotopic ratios is valuable for understanding the chemical evolution of interstellar material. In this light, carbon monoxide $^{12}\text{C}/^{13}\text{C}$, can be an important tracer of process of isotopic fractionation. Numerous measurements of the $^{12}\text{C}/^{13}\text{C}$ ratios towards Galactic sources have been carried out using simple molecules such as CO, CN and H_2CO (Langer & Penzias 1990, 1993; Wilson & Rood

1994; Wouterloot & Brand 1996; Milam et al. 2005). These studies have shown that the $^{12}\text{C}/^{13}\text{C}$ ratio becomes larger with increasing distance from the Galactic Center. More specifically, Wilson (1999) gives a mean $^{12}\text{C}/^{13}\text{C}$ ratio of 69 ± 6 in the Local ISM, 53 ± 4 at 4 kpc (the molecular ring) and of about 20 toward the Galactic center, showing a strong gradient that can be given for CO by (Milam et al. 2005):

$$^{12}\text{C}/^{13}\text{C} = 5.41(1.07)\text{D}_{\text{GC}} + 19.03(7.90) \quad (1)$$

with D_{GC} the distance from the Galactic Center in kpc. Furthermore, Milam et al. (2005) have shown that the $^{12}\text{C}/^{13}\text{C}$ gradient for the CO, CN

¹This publication is based on data acquired with the Atacama Pathfinder Experiment (APEX). APEX is a collaboration between the Max-Planck-Institut für Radioastronomie, the European Southern Observatory, and the Onsala Space Observatory (under programme ID 089.F-9319).

and H₂CO molecular species can be defined by:

$$^{12}\text{C}/^{13}\text{C} = 6.21(1.00)D_{\text{GC}} + 18.71(7.37), \quad (2)$$

with D_{GC} the distance from the Galactic Center in kpc. This makes these carbon isotopologue species valuable indicators of Galactic chemical evolution: although they are formed through different chemical pathways and present different chemical histories, they do not show significantly different $^{12}\text{C}/^{13}\text{C}$ ratios.

Until now the $^{12}\text{C}/^{13}\text{C}$ ratio has predominantly been measured in simple species that form mostly via reactions in the gas phase. In contrast, complex molecules are believed to form, for the most part, on grain surfaces, although gas phase formation cannot be ruled out (e.g. Herbst & van Dishoeck 2009; Charnley & Rodgers 2005). In this case, for complex species, the isotopic ratios might betray evidence of the grain surface formation as the ratio would differ from pure gas phase formation since gas phase processes, such as selective photodissociation and fractionation in low-temperature ion-molecule reactions, would impact the $^{12}\text{C}/^{13}\text{C}$ ratio which is then implanted in larger species (Charnley et al. 2004; Wirström et al. 2011). Indeed, Wirström et al. (2011) have shown that the isotopic $^{12}\text{C}/^{13}\text{C}$ ratio in methanol (CH₃OH) can be used to distinguish a gas-phase origin from an ice grain mantle one. Methanol is believed to be formed on dust grains from hydrogenation of CO (e.g. Cuppen et al. 2009). If this is the case, the measured $^{12}\text{C}/^{13}\text{C}$ ratios in CO and CH₃OH should be similar. Otherwise, the isotopic $^{12}\text{C}/^{13}\text{C}$ ratio in methanol should be higher than the one in CO due to fractionation of species that rely on the atomic ‘carbon isotope pool’ for formation (see Wirström et al. 2011; Langer et al. 1984).

In that light, we extend the $^{12}\text{C}/^{13}\text{C}$ investigation to interstellar methyl formate (HCOOCH₃, hereafter MF or $^{12}\text{C}-\text{MF}$), which is among the most abundant complex molecules detected in massive star-forming regions (e.g. Liu et al. 2001; Remijan et al. 2004; Bisschop et al. 2007; Demyk et al. 2008; Shiao et al. 2010; Favre et al. 2011; Friedel & Snyder 2008; Friedel & Widicus Weaver 2012). Also, the detection of both the $^{13}\text{C}-\text{MF}$ isotopologues, H¹³COOCH₃ (hereafter, $^{13}\text{C}_1-\text{MF}$) and HCOO¹³CH₃ (hereafter, $^{13}\text{C}_2-\text{MF}$) have been reported toward Orion-KL by Carvajal et al. (2009) based on

IRAM 30m-antenna observations. More specifically, we suggest that the $^{12}\text{C}/^{13}\text{C}$ ratio in methyl formate could also be used as an indicator of its formation origin. This since methyl formate may be efficiently formed close to the surface of icy grain mantles during the hot core warm up phase via reactions involving mobile radical species, such as CH₃O and HCO, that are produced by cosmic-ray induced photodissociation of methanol ices and ultimately owe their origin to hydrogenation of CO (e.g. Bennett & Kaiser 2007; Horn et al. 2004; Neill et al. 2011; Garrod & Herbst 2006; Garrod et al. 2008; Herbst & van Dishoeck 2009). In this instance and in agreement with Wirström et al. (2011), if the $^{12}\text{C}/^{13}\text{C}$ ratios in methyl formate, methanol and CO are similar, that would likely suggest a formation on grain surfaces.

In this paper we investigate the carbon isotopic ratio for methyl formate isotopologues and therefore address the issue whether the $^{12}\text{C}/^{13}\text{C}$ ratio is the same for both simple and large molecules. Our analysis is based on recent spectroscopic and laboratory measurements of both the common isotopologue and the ^{13}C isotopologues (see, Carvajal et al. 2007, 2009, 2010; Ilyushin et al. 2009; Kleiner 2010; Margulès et al. 2010; Haykal et al. 2014, and this study). We would particularly like to stress that in order to derive a $^{12}\text{C}/^{13}\text{C}$ ratio with accuracy and to significantly reduce uncertainties, homogeneous data are a necessity. In Section 2, we present the ALMA Science Verification observations of Orion-KL along with the APEX observations of our massive star-forming regions sample. Spectroscopic characterization of the ^{13}C -methyl formate molecules is presented in Section 3. Data modeling, results and analysis are presented and discussed in Sects. 4, 5 and 6, with conclusions set out in Sect. 7.

2. Observations and data reduction

2.1. ALMA Science Verification observations

Orion-KL was observed with 16 antennas (each of 12 m in diameter) on January 20, 2012, as part of the ALMA Science Verification (hereafter, ALMA-SV) program. The observations cover the frequency range 213.7 GHz to 246.6 GHz in band 6. The phase-tracking centre was $\alpha_{J2000} =$

TABLE 1
LIST OF SOURCES OBSERVED WITH THE APEX TELESCOPE.

Source	Observed Date	$\alpha_{\text{J}2000}$	$\delta_{\text{J}2000}$	V_{LSR}	Distance from the Sun	Distance from the GC
		($^{\text{h}} : ^{\text{m}} : ^{\text{s}}$)	($^{\circ} : ' : ''$)	(km s $^{-1}$)	(kpc)	(kpc)
Sgr B2(N-LMH)	2012 April 02, 03	17:47:19.9	-28:22:19.5	64.0	7.1	0.1 ^a
G24.78+0.08	2012 April 02	18:36:12.6	-07:12:11.0	111.0	7.7	3.7 ^b
G29.96-0.02	2012 April 01	18:46:04.0	-02:39:21.5	98.8	6.0	4.6 ^c
G19.61-0.23	2012 March 28	18:27:38.1	-11:56:39.0	40.0	3.5	4.8 ^d
NGC 6334 IRS 1	2012 March 28	17:20:53.0	-35:47:02.0	-8.0	1.7	6.8 ^e
	2012 August 17, 18					
W51 e2	2012 April 02	19:23:43.9	+14:30:34.8	55.3	5.41	8.3 ^f
Orion-KL	2012 April 01	05:35:14.2	-05:22:36.0	8.0	0.4	8.9 ^g
	2012 April 04, 05					

^aMilam et al. (2005).

^bBeltrán et al. (2011).

^cPratap et al. (1999).

^dRemijan et al. (2004).

^eKraemer et al. (1998).

^fSato et al. (2010).

^gRemijan et al. (2003).

$05^h35^m14\rlap{.}^s35$, $\delta_{J2000} = -05^\circ22'35\rlap{.}''00$. The observational data consist of 20 spectral windows, each with 488 kHz channel spacing resulting in 3840 channels across 1.875 GHz effective bandwidth.

We used the public release calibrated data that are available through the ALMA Science Verification Portal². Data reduction and continuum subtraction were performed using the Common Astronomy Software Applications (CASA) software³. More specifically, the continuum emission was estimated by a zeroth order fit to the line-free channels within each spectral window (hereafter spw) and subtracted. Finally, the spectral line data cleaning was performed using the Clark (1980) method and a pixel size of $0.4''$. Also, a Briggs weighting with a robustness parameter of 0.0 was applied giving a good trade-off between natural and uniform weighting (Briggs 1995). The resulting synthesized beam sizes are:

- $1.6'' \times 1.1''$ (P.A. of about $-176 - 4^\circ$) for the spw 0, 1, 4, 5, 8, 9, 12, 13, 16 and 17,
- $1.7'' \times 1.2''$ (P.A. of about $-1 - 11^\circ$) for the spw 2, 3, 6, 7, 10, 11, 14, 15, 18 and 19.

2.2. APEX observations

2.2.1. Source sample

Our survey is composed of a sample of seven high-mass star-forming regions that are listed in Table 1 together with their respective coordinates, LSR velocities and distances from the Sun as well as from the Galactic Center. The 7 sources were primarily selected upon the following criteria: *i)* the previous detection of the main HCOOCH₃ isotopologue, based on single-dish and/or interferometric observations (e.g. Liu et al. 2001; Remijan et al. 2004; Bisschop et al. 2007; Demyk et al. 2008; Friedel & Snyder 2008; Shiao et al. 2010; Favre et al. 2011; Belloche et al. 2009; Widicus Weaver & Friedel 2012; Fontani et al. 2007; Olmi et al. 2003; Beuther et al. 2007, 2009; Kalenskii & Johansson 2010; Requena-Torres 2006; Hollis et al. 2000; Mehringer et al. 1997), with a derived column density in the range 10^{16} - 10^{17} cm⁻² depending on the source and the assumed source size, and *ii)* covering a wide range

in distance from the Galactic Center, here from 0.1 kpc to 8.9 kpc (see Table 1).

2.2.2. Observations

The observations were performed with the APEX telescope on Llano de Chajnantor, Northern Chile, between March and August 2012 (see Table 1). The Swedish Heterodyne Facility Instrument (SHeFi) APEX-2 receiver, which operates with an IF range of 4–8 GHz, was used in single sideband mode in connection to the eXtended bandwidth Fast Fourier Transform Spectrometer (XFFTS) backend in the frequency range 283.4 GHz – 287.4 GHz. This frequency range was chosen from line intensity predictions based on the Orion-KL study by Carvajal et al. (2009). The half-power beam size is $22''$ for observations at 285.4 GHz. The image rejection ratio is 10 dB over the entire band⁴. Also, the XFFTS backend covers 2.5 GHz bandwidth instantaneously with a spectral resolution of about 0.08 MHz (corresponding to 0.08 km/s). However, noting that line-widths of the target lines are estimated to be between 4 and 8 km s⁻¹ based on earlier methyl formate observations referred to above, the spectra were smoothed to a spectral resolution of 1.5 km s⁻¹. Further, in this paper, the spectra are reported in units of the main beam temperature (T_{MB}), that is given by

$$T_{MB} = \frac{\eta_f}{\eta_{MB}} T_A^*, \quad (3)$$

where $\eta_f T_A^*$ is the antenna temperature outside the atmosphere, η_f the forward efficiency ($\eta_f=0.97$ for the APEX-2 instrument⁵) and η_{MB} the main beam efficiency ($\eta_{MB}=0.73$ for the APEX-2 instrument⁵).

G29.96-0.02, G19.61-0.23, NGC 6334 IRS 1 (2012 March 28) and W51 e2 observation data were taken in wobbler switching with a throw of $150''$ in azimuth and a wobbling rate of 0.5 Hz in symmetric mode. Regarding Orion-KL, NGC 6334 IRS 1 (2012 August 17 and 18), eSgr.B2(N-LMH) and G24.78+0.08, the data were performed in position switching mode using the reference OFF positions that are listed in Table 2.

The tuning frequency was set to 285.370 GHz for all the observed sources. Also, additional

²<http://almascience.eso.org/almadata/sciver/OrionKLBand6/>

³<http://casa.nrao.edu>

⁴<http://www.apex-telescope.org/heterodyne/shfi/>

⁵see <http://www.apex-telescope.org/telescope/efficiency/>

scans at a tuning frequency of 285.400 GHz were performed toward Orion-KL and Sgr B2(N-LMH) as complementary observations in order to likely identify lines that are coming from the image side-band. The three following strong contaminants have been identified:

- the sulfur monoxide line, SO $^3\Sigma$ ($v = 0, 6_{7-56}$), at 296.550 GHz,
- the sulfur monoxide line, ^{33}SO (7_{7-6_6}), at 298.246 GHz,
- and the sulfur dioxide line, SO₂ ($v = 0, 9_{2,8-8_{1,7}}$) at 298.576 GHz.

These contaminants have been identified from the detailed model of molecular emission towards Orion-KL that matched emission from ~ 100 GHz to 1.9 THz (hereafter HIFI spectral fit, see Crockett et al. 2010, 2014). Accounting for a 10 dB rejection, the lines mentioned above could contaminate the observed Orion-KL spectrum with a signal greater than 2 K in T_{MB} scale (i.e. ≥ 1.5 K in T_A^{*}). Such contamination would be significant in our observations. In addition, two unidentified lines from image side-band were present in the observed spectrum. Therefore, in each data set and for each source, the channels corresponding to the emission from all these lines have been removed. Our data should thus be free from contamination by lines which are coming from the rejected side-band. Nonetheless, we stress that other lines from the image side-band may still, unfortunately, pollute the observed spectra.

Table 2: Reference position for Position Switching mode.

Source	OFF position ^a
Orion-KL	EQ[-500'',0.0'']
NGC 6334 IRS 1	EQ[-500'',0.0'']
Sgr B2(N-LMH)	EQ[-752'',342'']
G24.78+0.08	EQ[7071'',-947'']

^aThe coordinates are given in the equatorial (EQ) system.

3. Spectral characterization for the ^{13}C -methyl formate isotopologues

The interstellar identifications of $^{13}\text{C}_1\text{-MF}$, $^{13}\text{C}_2\text{-MF}$ were carried out from their spectral predictions in the frequency range of the facilities. These predictions were computed through the Hamiltonian parameters of the $^{13}\text{C}_2\text{-MF}$ isotopologue provided by Carvajal et al. (2009) and of the $^{13}\text{C}_1\text{-MF}$ isotopologue from Carvajal et al. (2010). The dipole moments used in the intensity calculation were given by Margulès et al. (2010).

The spectroscopic characterization of ^{13}C -MF isotopologues were carried out starting with millimeter- and submillimeter-wave recordings in the laboratory and followed by their spectral analysis and the assignments of the transition lines through an established fitting procedure. The effective Hamiltonian used for the global spectroscopic analysis of both isotopologues is based in the so-called Rho-Axis Method (RAM) (Herbst et al. 1984; Hougen et al. 1994; Kleiner 2010) applicable for molecules with a CH₃ rotor. The BELGI version of the RAM code used in this study is available online⁶. Further details regarding its application to the methyl formate isotopologues are described by Carvajal et al. (2007).

The Hamiltonian parameters were fitted to the experimental data of $^{13}\text{C}_2\text{-MF}$ (~ 940 lines) which were provided only for the ground torsional state $v_t = 0$ (Carvajal et al. 2009). New experimental data for the $v_t = 0$ ground and $v_t = 1$ first excited torsional state are presently being processed (Haykal et al. 2014). A more extensive set of experimental data (~ 7500 transition lines) of the ground and first excited states of $^{13}\text{C}_1\text{-MF}$ has been used in the fit of the RAM Hamiltonian. The complete set of available experimental data (see Willaert et al. 2006; Carvajal et al. 2009; Maeda et al. 2008b,a) was compiled in Carvajal et al. (2010).

⁶The source code BELGI along with an example of input data file and a readme file are available at the Web site: <http://www.ifpan.edu.pl/~kisiel/introt/introt.htm#belgi>, managed by Dr. Zbigniew Kisiel. For extended versions of the code, please contact Isabelle Kleiner or Miguel Carvajal.

TABLE 3

ROTATIONAL-TORSIONAL-VIBRATIONAL PARTITION FUNCTION^a FOR $^{13}\text{C}_1\text{-MF}$, $^{13}\text{C}_2\text{-MF}$ AND $^{12}\text{C}\text{-MF}$.

T(K)	$^{13}\text{C}_1\text{-MF}$	$^{13}\text{C}_2\text{-MF}$	$^{12}\text{C}\text{-MF}$
300.0	252230.47	255988.58	249172.44
225.0	105303.23	106847.86	104015.96
150.0	36879.42	37442.27	36433.43
75.0	9003.31	9162.12	8894.06
37.50	2920.56	2971.20	2885.3
18.75	1027.71	1045.22	1015.31
9.375	364.76	370.95	360.33

^aThe nuclear spin degeneracy was not considered in these calculations (see Appendix A).

3.1. Partition functions

To calculate the observed intensities of the spectral lines, the populations of each level must be estimated using an accurate partition function in order to provide reliable estimates of the temperatures and column densities of the different regions in the ISM. With this goal in mind, a convergence study for the partition functions of ^{13}C -isotopologues, which ensures that high enough energy levels have been included for a particular temperature, has been carried out in this work. The partition function calculations are described in the Appendix A. Table 3 summarizes the rotational-torsional-vibrational partition function values that are used here for $^{13}\text{C}_1\text{-MF}$ and $^{13}\text{C}_2\text{-MF}$.

4. Data analysis

4.1. Database and MF, ^{13}C -MF frequencies

We used the measured and predicted transitions coming from both the table of Ilyushin et al. (2009) and the JPL database⁷ (Pickett et al. 1992, 1998) for the MF line assignments, as in Favre et al. (2011). Regarding the methyl formate isotopologue $^{13}\text{C}_1\text{-MF}$ and $^{13}\text{C}_2\text{-MF}$ line assignments, our present analysis is based on this study (see Section 3) and on the spectroscopic characterization performed by Carvajal et al. (2007,

2009, 2010). Likewise, the measured and predicted transitions of the species $^{13}\text{C}_1\text{-MF}$ species (Carvajal et al. 2010) are now available on the CDMS database⁸ (Müller et al. 2001, 2005) and at Splatatalogue⁹ (Remijan et al. 2007). Current spectroscopic data for MF and ^{13}C -MF treat both the two torsional substates – with A and E symmetries – simultaneously.

As we aim to derive accurate isotopic ratios, we should be confident with the intensity calculation of the molecular species at different temperatures. Therefore, the isotope ratio accuracy will depend, on one hand, on the spectroscopic determination of transition frequencies, assignments and line strengths and, on the other hand, on the partition function approximation considered. Accurate spectroscopic characterizations of the main isotopologue was carried out previously (Ilyushin et al. 2009) using the RAM method, while for the ^{13}C -MF isotopologues we used the same values for the electric dipole moments as for the ^{12}C -MF species (see Section 3.1). This assumption would not affect the line strengths more than $\sim 1\%$. Hence, the accurate derivation of the abundance ratio between different isotopologues will rely, as far as the spectroscopic data are concerned, on the partition function. This was computed under the same level of approxi-

⁸<http://www.astro.uni-koeln.de/cdms>

⁹www.splatalogue.net

⁷<http://spec.jpl.nasa.gov/home.html>

mation for all the molecular species under study. Table 3 shows the values of the partition function used for $\text{H}^{12}\text{COOCH}_3$. These values were computed on the basis of the new calculations in this manuscript to fuller account for the effect of vibrationally excited levels. In the JPL catalog entry, only contributions of the $v_t = 0$ and $v_t = 1$ level are incorporated into the partition function, while here we account for all torsional–vibrational energy states. This results in a higher inferred ^{12}C methyl formate abundance than would be derived using the value in the JPL catalog since the partition function is now larger than in the JPL tables. The partition function used here is higher than that in the JPL catalog by a factor of 1.2 at a temperature of 150 K, and by a factor of 2.5 at 300 K. Our more accurate partition functions yield a more accurate abundance of methyl formate than is reported in earlier publications.

It is also worthwhile to remark that the methyl formate partition function provided in the JPL catalog file has an extra factor of 2 in its formula with respect to ours. This factor arises from the product of the reduced nuclear spin and K-level degeneracy statistical weights g_I , g_k (Turner 1991; Favre et al. 2011). As for methyl formate the statistical weights are cancelled in the intensity mathematical expression (see e.g. Eq.(1) of Turner 1991), they have not been considered in the partition function calculation of this paper. This means that when the comparison between the partition function of this work and the one provided in the JPL catalog was established, this latter was divided out by the factor of 2.

Also, our spectral line analysis of the ALMA-SV observations of Orion-KL takes into account the ^{12}C methyl formate transitions that are both in the ground and first torsionally excited states since they seem to probe a similar temperature toward this region (see Favre et al. 2011; Kobayashi et al. 2007). However, regarding the sources observed with the APEX telescope, we have only considered methyl formate transitions in their ground torsional states $v_t = 0$. More specifically, the number of detected transitions in the $v_t = 1$ state (4 lines with a similar upper energy level) is insufficient to determine any trend with respect to transitions emitting in the ground state ($v_t = 0$).

4.2. XCLASS modeling and Herschel/HIFI spectral fit

Assuming local thermodynamic equilibrium (LTE), we have modeled all the methyl formate isotopologue emission by using the XCLASS¹⁰ program along with the HIFI spectral fit that are based on the observations of Orion-KL acquired with Herschel/HIFI as part of the Herschel Observations of Extra-Ordinary Sources key program (Bergin et al. 2010; Crockett et al. 2014). This allows us to make reliable line identifications and determine where potential line blends may exist. Further details regarding the XCLASS modeling of the Herschel/HIFI Orion-KL spectral scan, along with fit parameters, can be found in Crockett et al. (2014).

In the present analysis, we assumed that the $^{13}\text{C}_1\text{-MF}$ and $^{13}\text{C}_2\text{-MF}$ species emits within the same source size, at the same rotational temperature and velocity, and with the same line-width as the methyl formate molecule. The only adjustable parameter is the molecular column density. To initialize the model of the ALMA-SV observations of Orion-KL, we used as input parameters (source size, rotational temperature, column density, v_{LSR} and Δv_{LSR}), the values derived by our previous Plateau de Bure Interferometer (PdBI) observations, which were performed with a similar angular resolution ($1.8'' \times 0.8''$, see Favre et al. 2011). Regarding the APEX observations, we used previously related and reported values derived from single-dish (JCMT, IRAM-30m, Herschel) and/or interferometric observations (BIMA, CARMA) as starting values to initialize the fitting. More specifically, we used the values derived by Bisschop et al. (2007) for G24.78+0.08, by Zernickel et al. (2012) and Bisschop et al. (2007) for NGC6334I, by Demyk et al. (2008) for W51 e2, by Shiao et al. (2010) for G29.96–0.02, by Belloche et al. (2009) for SgrB2(N), by Remijan et al. (2004) and Shiao et al. (2010) for G19.61–0.23 and by Tercero et al. (2012), Carvajal et al. (2009) and Crockett et al. (2014) for Orion-KL.

¹⁰<http://www.astro.uni-koeln.de/projects/schilke/XCLASS>

TABLE 4

NUMBER OF DETECTED TRANSITIONS OF ^{12}C -MF AND ^{13}C -MF IN THE ALMA-SV DATA OF ORION-KL^a.

Spw ^b	Compact Ridge			Hot Core-SW		
	HCOOCH ₃	H ¹³ COOCH ₃	HCOO ¹³ CH ₃	HCOOCH ₃	H ¹³ COOCH ₃	HCOO ¹³ CH ₃
0	1	1	2	1	—	2
1	3	—	6	3	—	1
2	19	10	3	19	7	3
3	5	6	3	5	3	3
4	11	7	4	10	3	4
5	20	13	6	19	5	5
6	5	12	—	5	4	—
7	6	2	13	4	—	6
8	11	11	1	8	5	—
9	10	13	2	9	10	2
10	4	1	5	4	1	3
11	20	10	4	20	5	2
12	1	—	15	—	—	6
13	2	4	17	2	3	11
14	3	9	2	3	6	—
15	6	4	—	6	2	—
16	15	12	8	15	6	6
17	23	16	3	21	12	2
18	2	3	17	2	1	5
19	—	1	11	—	—	6

^aThe corresponding line frequencies are given in Figures C-1, C-2, C-3, D-1, D-2 and D-3.

^bThe ALMA-SV data consist of 20 spectral windows (see Section 2).

5. Results

In the following section we report the main results for each observing facility.

5.1. ALMA-SV observations of Orion-KL

5.1.1. Emission maps

The mean velocity for emission observed towards the Compact Ridge and Hot Core-SW regions is around 7.3 km s^{-1} for all the methyl formate isotopologues. We also observed a second velocity component around 9 km s^{-1} toward the Compact Ridge in HCOOCH_3 (as reported by Favre et al. 2011). This velocity component is not observed in ^{13}C -MF. Figure 1 shows maps of the MF, $^{13}\text{C}_1$ -MF and $^{13}\text{C}_2$ -MF emission in the 7.2 km s^{-1} channel measured at 234124 MHz, 220341 MHz and 216671 MHz, respectively. The HCOOCH_3 distribution shows an extended V-shaped molecular emission that links the radio source I to the BN object as previously observed in methyl formate by Favre et al. (2011) and Friedel & Snyder (2008). Likewise, as reported by Favre et al. (2011), the main molecular peaks are located toward the Compact Ridge and the Hot Core-SW (respectively labeled MF1 and MF2 in Fig.1; for more details see Favre et al. 2011). Also we note that from the optically thick HCOOCH_3 lines, another cold component ($T \sim 40\text{--}50 \text{ K}$) arising from the vicinity of the source IRC7 is observed. We did not analyze this component in the present study, however. Finally, the ^{13}C -MF isotopologues are mainly detected toward the Compact Ridge and the Hot Core-SW (5σ detection level, see Fig 1).

5.1.2. Spectra

Numerous transitions of ^{12}C -MF and ^{13}C -MF, with $S\mu^2 \geq 10 \text{ D}^2$ and from upper energy levels of 166 K up to 504 K for the main molecule and E_{up} of 99 K up to 330 K for the ^{13}C -MF species, are present in the ALMA data. We have modeled each spectral window individually (see Section 6.1.3). Table 4 provides the number of clearly detected MF and ^{13}C -MF transitions per spectral window toward both the Compact Ridge and the Hot Core-SW. Table B1 in Appendix B summarizes the line parameters for all detected, blended, or not detected transitions of ^{12}C -MF, $^{13}\text{C}_1$ -MF

and $^{13}\text{C}_2$ -MF in all ALMA spectral windows. Furthermore, figures C-1, C-2 and C-3 in Appendix C show the ^{12}C -MF, $^{13}\text{C}_1$ -MF and $^{13}\text{C}_2$ -MF transitions that are detected and/or partially blended in the ALMA-SV data along with our best XCLASS models toward the Compact Ridge. In addition, Figures D-1, D-2 and D-3 in the Appendix D show the emission of the same transitions, along with our models, toward the Hot Core-SW. The quality of our models is based on the reduced χ^2 , which lies in the range 0.3–2.4, depending on the fit¹¹. More specifically, the bulk of the emission is best reproduced for:

- a source size of $3''$ (in agreement with the ALMA-SV observations) towards both the Compact Ridge and the Hot-Core-SW,
- a rotation temperature of 80 K toward the Compact Ridge and of 128 K toward the Hot-Core-SW,
- a v_{LSR} of 7.3 km s^{-1} for both components,
- and a line-width of 1.2 km s^{-1} toward the Compact Ridge and of 2.4 km s^{-1} toward the Hot-Core-SW.

Only the column density differs within the different spectral windows, between the spatial components associated with Orion-KL and between the isotopologues. The ^{12}C -MF models include the observed second velocity component well reproduced for a v_{LSR} of 9.1 km s^{-1} , a source size of $3''$, a rotation temperature of 120 K and a column density of $7 \times 10^{16} \text{ cm}^{-2}$.

5.1.3. Isotopic $^{12}\text{C}/^{13}\text{C}$ ratio

Figure 2 shows the distribution of the $^{12}\text{C}/^{13}\text{C}_1$ -MF, $^{12}\text{C}/^{13}\text{C}_2$ -MF and $^{12}\text{C}/^{13}\text{C}$ -MF isotopic ratios we derived within each ALMA spectral window towards both the Compact Ridge¹² and the Hot Core-SW. The average $^{12}\text{C}/^{13}\text{C}_1$ and

¹¹The optically thick lines, although shown in appendix, are excluded from our model due to optical depth problem in the model.

¹²An outlier at $^{12}\text{C}/^{13}\text{C} \sim 100$ is seen towards the Compact Ridge in each distribution. It result from MF measurement performed in the spw #16. The outlier likely doesn't impact the derived isotopic ratio since either we include or exclude the value because the derived ratio remains the same within the uncertainties.

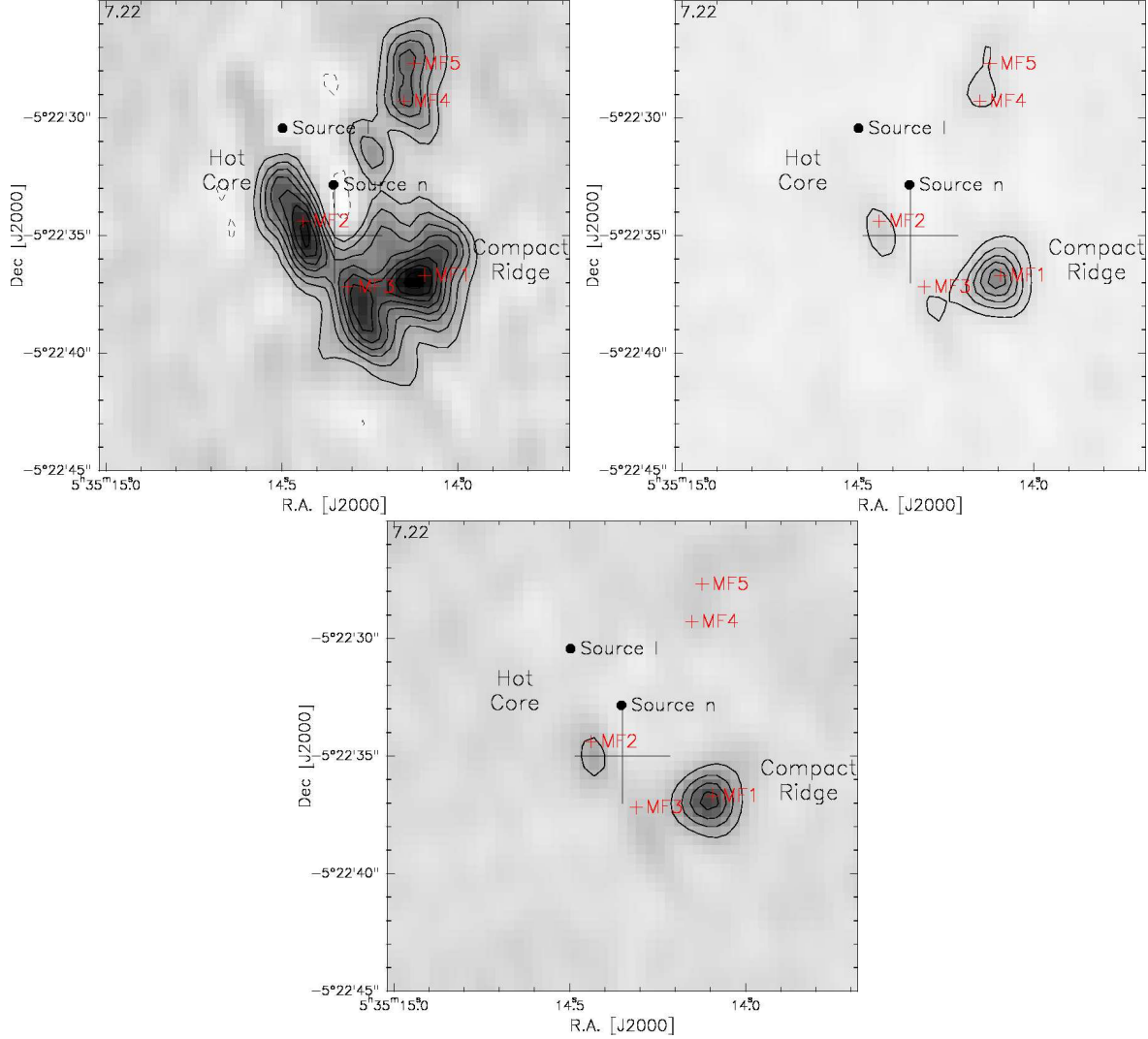


Fig. 1.— HCOOCH_3 (^{12}C -MF, 234124 MHz, $E_{up}=179$ K, $S\mu^2=35$ D 2 , top left panel), $\text{H}^{13}\text{COOCH}_3$ ($^{13}\text{C}_1$ -MF, 220341 MHz, $E_{up}=153$ K, $S\mu^2=37$ D 2 , top right panel) and $\text{HCOO}^{13}\text{CH}_3$ ($^{13}\text{C}_2$ -MF, 216671 MHz, $E_{up}=152$ K, $S\mu^2=36$ D 2 , bottom panel) emission channel maps at 7.22 km s $^{-1}$ as observed with ALMA. The first contour and level step are 500 mJy beam $^{-1}$ ($\sim 14\sigma$) and 100 mJy beam $^{-1}$ ($\sim 5\sigma$) for ^{12}C -MF and ^{13}C -MF, respectively. The synthesized beam size is 1.7'' \times 1.1''. The black cross indicates the centered position of the observations. The main HCOOCH_3 emission peaks (MF1 to MF5) identified by Favre et al. (2011) are indicated.

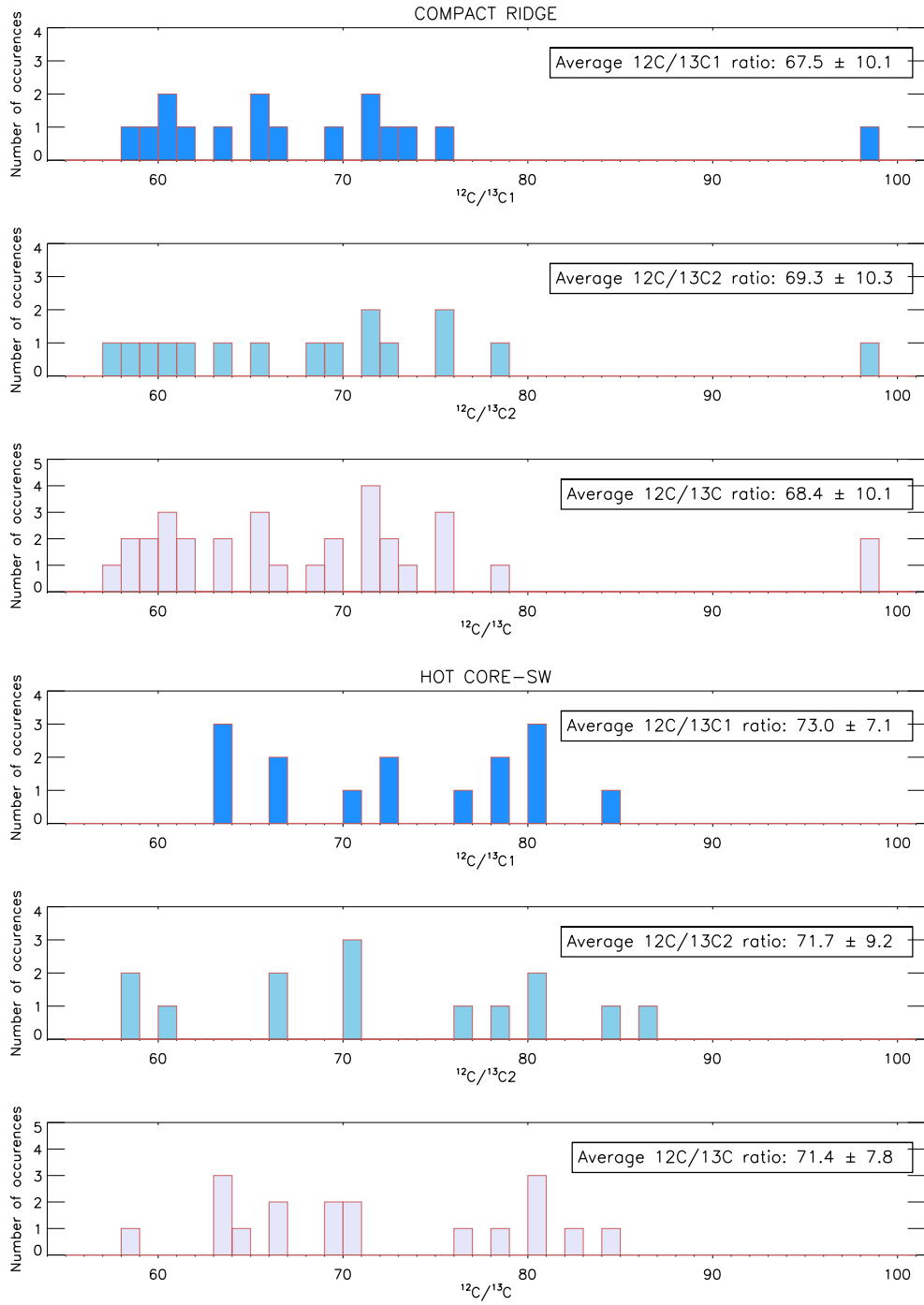


Fig. 2.— Isotopic ratio distribution of the methyl formate isotopologues within each ALMA spectral window as derived toward the Orion-KL Compact Ridge (Top panel) and Hot Core-SW (bottom panel). *Top sub-panels:* Isotopic ratio distribution for the $^{12}\text{C}/^{13}\text{C}_1$ ratio. *Middle sub-panels:* Isotopic ratio distribution for the $^{12}\text{C}/^{13}\text{C}_2$ ratio. *Bottom sub-panels:* Isotopic ratio distribution for the $^{12}\text{C}/^{13}\text{C}$ ratio, assuming the two ^{13}C -MF isotopologues have similar abundances. The derived average isotopic ratio is indicated in each sub-panel.

$^{12}\text{C}/^{13}\text{C}_2$ ratios are 67.5 ± 10.1 and 69.3 ± 10.3 in direction of the Compact Ridge, and 73.0 ± 7.1 and 71.7 ± 9.2 in direction of the Hot Core-SW. If we assume the ratio to be the same for both isotopologues, meaning there is no significant difference, we derive an average $^{12}\text{C}/^{13}\text{C}$ isotopic ratio in methyl formate of 68.4 ± 10.1 and of 71.4 ± 7.8 towards the Compact Ridge and the Hot Core-SW, respectively.

5.2. APEX observations of all the sources

Figure 3 shows the spectra observed with the APEX telescope toward our sample of 7 sources (see Tab. 1). Lines which have been identified through the Herschel/HIFI spectral fit are indicated in the Orion-KL spectrum (see bottom panel on Fig. 3). The molecular richness of the observed sources is clearly seen. Also, the different spectra illustrate the problem of the spectral confusion for the weaker emissive lines.

5.2.1. Main isotope: HCOOCH_3

Table 5 lists the detected or partially blended methyl formate transitions, with $S\mu^2 \geq 2.5 \text{ D}^2$ and E_{up} up to 304 K as observed with APEX towards the different sources. Note that for some partially blended lines, the emission arising from the contaminant has been identified through the Herschel template spectra, in which emission from 35 molecules has been modeled assuming LTE (Crockett et al. 2014). The following procedure was used: 1) superposing the Herschel resulting model to the APEX observations and identifying the potential contaminant(s) and 2), adjusting the observational parameters (e.g. velocity, typical line-width) to the model, checking the coherence over the full spectrum. The adopted parameters (source size, rotational temperature, column density, velocity and line-width) which were used to model the APEX observations are given in Table 6 for each source. The quality of our models is based on the reduced χ^2 , which lies in the range 0.23–4.75. In addition, Figure 4 shows the observed methyl formate spectrum of the transition at 285973.267 MHz ($23_{8,15} - 22_{8,14,E}$) along with our models for each source.

The main observational results for the methyl formate molecule are briefly summarized below for the individual sources.

Orion-KL: We detected sixteen HCOOCH_3 lines and observed fifteen transitions that are partially blended, with $S\mu^2 \geq 4 \text{ D}^2$ (see Table 5). The LSR velocity is 7.7 km s^{-1} and the derived column density is $9.7 \times 10^{16} \text{ cm}^{-2}$.

W51 e2: We detected eleven HCOOCH_3 lines and observed six transitions that are partially blended. Fourteen transitions (with $S\mu^2 \leq 12 \text{ D}^2$) are too faint to be detected (which is commensurate with our model of the source). The spectra display a v_{LSR} of 55.6 km s^{-1} and we derived a column density of $9.0 \times 10^{16} \text{ cm}^{-2}$.

G19.61-0.23: We detected ten HCOOCH_3 lines and observed seven transitions that are partially blended while fourteen transitions were too faint to be detected. The v_{LSR} is 39.7 km s^{-1} and the derived column density is $7.0 \times 10^{16} \text{ cm}^{-2}$.

G29.96-0.02: We detected ten HCOOCH_3 lines and observed seven transitions that are partially blended. Fourteen transitions were too faint to be detected. Spectra display a v_{LSR} of 97.8 km s^{-1} and we derived a column density of $3.5 \times 10^{15} \text{ cm}^{-2}$.

G24.78+0.08: We detected ten HCOOCH_3 lines and observed seven transitions that are partially blended while fourteen transitions were too faint to be detected. The v_{LSR} is 111 km s^{-1} and we derived column density of $6.0 \times 10^{15} \text{ cm}^{-2}$.

NGC 6334 IRS 1: We detected eleven HCOOCH_3 lines and observed six transitions that are partially blended with fourteen transitions were too faint to be detected. Spectra exhibit a v_{LSR} of -8 km s^{-1} and we derived a column density of $4.5 \times 10^{17} \text{ cm}^{-2}$.

Sgr B2(N): We detected seven HCOOCH_3 lines and observed nine transitions that are partially blended while fourteen transitions were too faint to be detected. The v_{LSR} is around 63.7 km s^{-1} . We derived a column density of $3.0 \times 10^{17} \text{ cm}^{-2}$.

5.2.2. $H^{13}\text{COOCH}_3$

The $^{13}\text{C}_1$ -MF lines all appear to be blended or just at or below the confusion limit level. We note that some transitions overlap with lines from strongly emissive molecules such as ethyl cyanide (whose presence is known through the Herschel template spectra to Orion-KL, Crockett et al. 2014), which might hide faint emission. We therefore do not detect the $^{13}\text{C}_1$ -methyl formate toward

any of the observed sources, excluding Orion-KL and that only in the supplementary ALMA data.

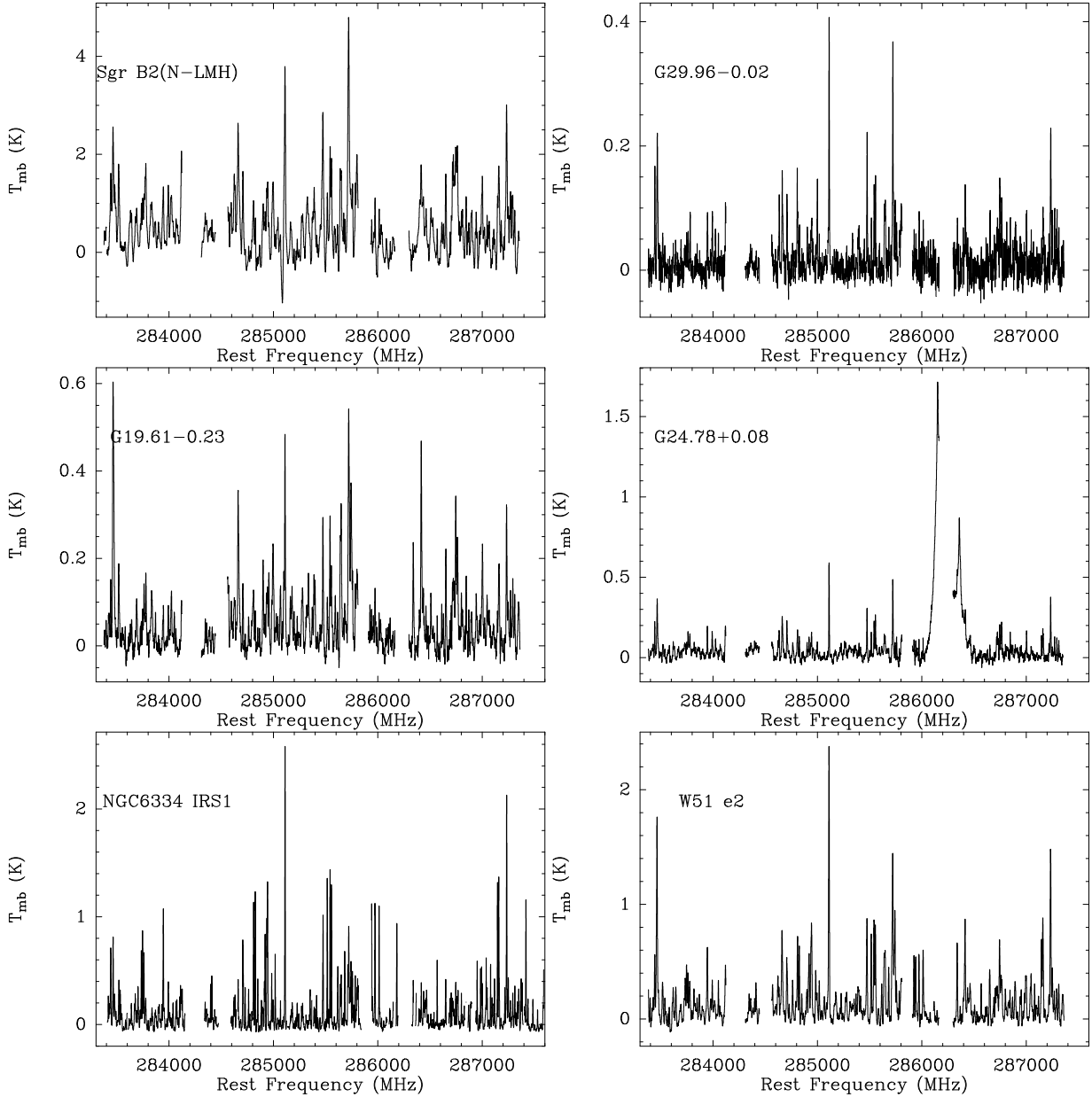


Fig. 3.— Spectra centered at 285.450 GHz as observed with the APEX telescope for all the sources. The name of each observed sources is indicated on each plot. The spectral resolution is smoothed to 1.5 km s^{-1} . Line assignment is shown in the Orion-KL spectrum (bottom panel) in red for the detected methyl formate $^{12}\text{C-MF}$ and $^{13}\text{C-MF}$ transitions and in grey for the other molecules (based on the Herschel/HIFI spectral fit to Orion-KL for the latter, see Crockett et al. 2014).

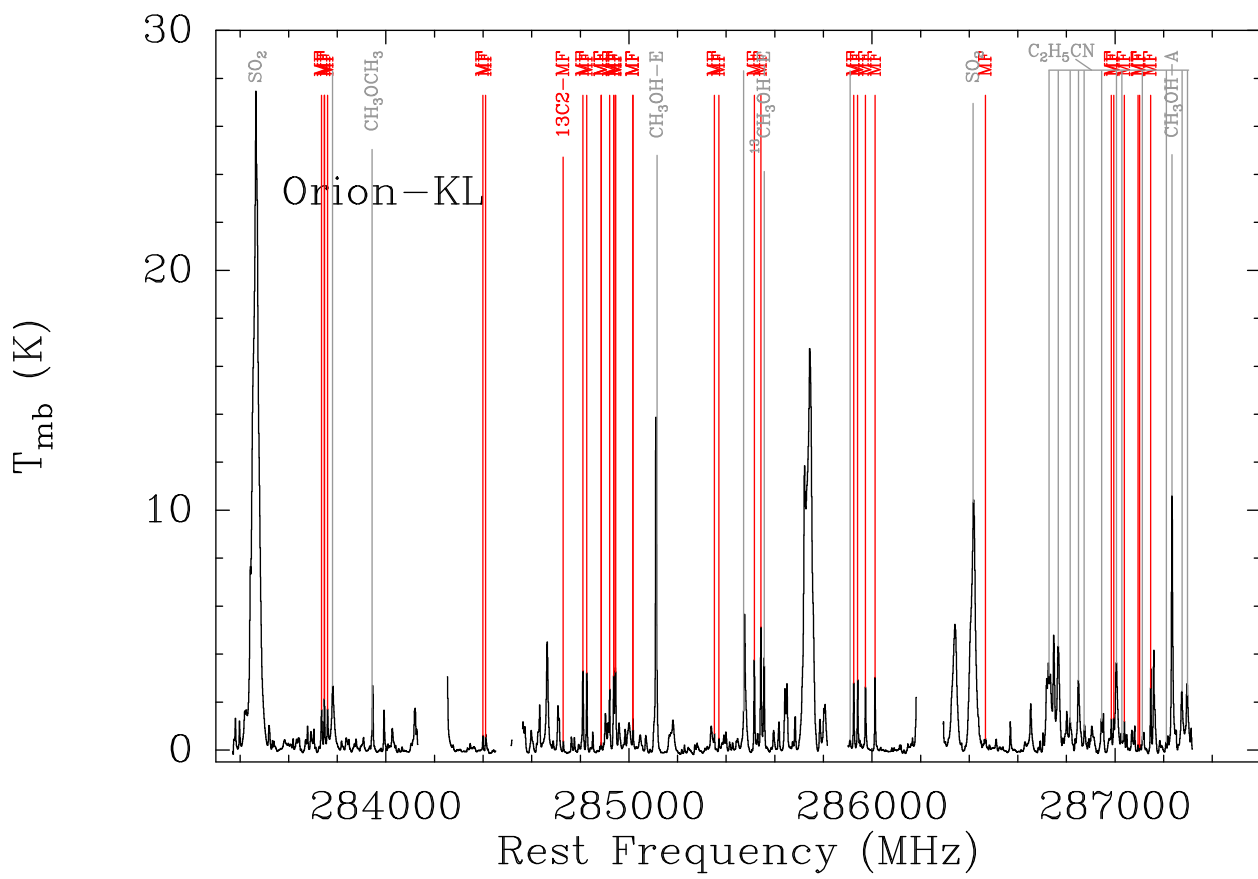


Fig. 3.— Continue.

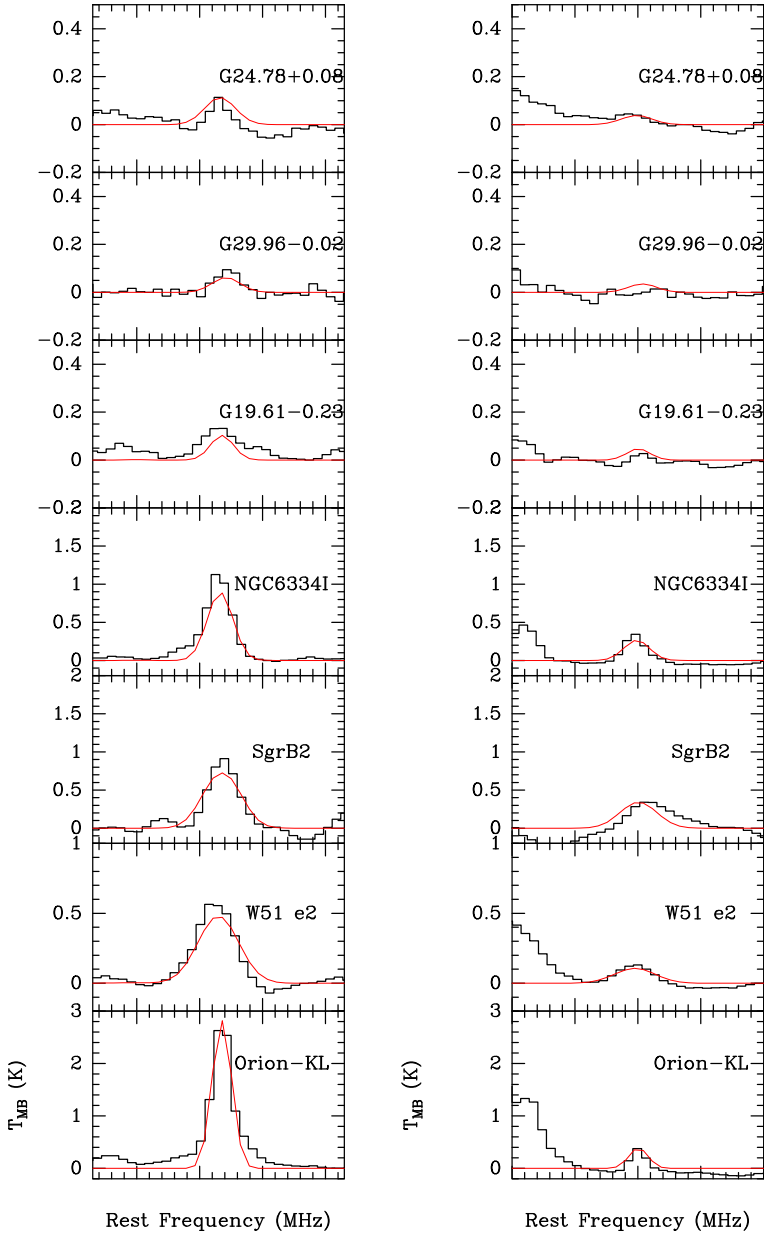


Fig. 4.— HCOOCH_3 (^{12}C -MF, transition at 285973.267 MHz, left panel) and $\text{HCOO}^{13}\text{CH}_3$ ($^{13}\text{C}_2$ -MF, transition at 284730.102 MHz, right panel) synthetic spectra (in red) overlaid on the observed spectrum (in black) as observed with APEX. The name of the sources is indicated on each plot.

TABLE 5
TRANSITIONS OF ^{12}C AND ^{13}C -METHYL FORMATE OBSERVED WITH THE APEX TELESCOPE.

Frequency (MHz)	Transition	E_{up} (K)	$S\mu^2$ (D 2)	Note ^a							
				Orion-KL	W51 e2	G19.61-0.23	G29.96-0.02	G24.78+0.08	NGC 6334 IRS 1	Sgr B2(N-LMH)	
HCOOCH_3											
283734.887	23 _{11,12} – 22 _{11,11} E	243.2	45.4	D	D	D	D	PB	D	D	D
283746.738	23 _{11,13} – 22 _{11,12} A	243.2	45.4	PB	PB	PB	PB	PB	PB	PB	PB
283746.738	23 _{11,12} – 22 _{11,11} A	243.2	45.4	PB	PB	PB	PB	PB	PB	PB	PB
283760.086	23 _{11,13} – 22 _{11,12} E	243.2	45.4	D	D	D	D	D	D	D	PB
284398.680	13 _{5,8} – 12 _{4,9} E	70.4	2.5	D	ND	ND	ND	ND	ND	ND	ND
284410.529	13 _{5,8} – 12 _{4,9} A	70.4	2.7	PB	ND	ND	ND	ND	ND	ND	ND
284810.313	23 _{5,19} – 22 _{5,18} E	180.8	55.8	PB	PB	PB	PB	PB	PB	PB	PB
284826.396	23 _{5,19} – 22 _{5,18} A	180.8	55.8	D	D	D	D	D	D	D	D
284885.531	27 _{11,16} – 27 _{10,17} A	303.7	7.6	PB	ND	ND	ND	ND	ND	ND	ND
284886.320 ^b	27 _{11,16} – 27 _{10,17} E	303.7	6.1	PB	ND	ND	ND	ND	ND	ND	ND
284920.240	23 _{9,14} – 22 _{9,13} E	217.0	49.8	D	D	D	D	D	D	D	D
284937.218	23 _{9,15} – 22 _{9,14} A	217.0	49.9	PB	PB	PB	PB	PB	PB	PB	PB
284942.751	23 _{9,14} – 22 _{9,13} A	217.0	49.9	PB	PB	PB	PB	PB	PB	PB	PB
284945.147	23 _{9,15} – 22 _{9,14} E	216.9	49.8	PB	PB	PB	PB	PB	PB	PB	PB
285016.270	23 _{4,20} – 22 _{3,19} E	173.3	6.3	PB	ND	ND	ND	ND	ND	ND	ND
285016.977	23 _{4,20} – 22 _{3,19} A	173.3	6.3	PB	ND	ND	ND	ND	ND	ND	ND
285351.819	24 _{3,21} – 23 _{4,20} E	187.0	6.8	PB	ND	ND	ND	ND	ND	ND	ND
285370.140	24 _{3,21} – 23 _{4,20} A	187.0	6.8	D	ND	ND	ND	ND	ND	ND	ND
285515.739	22 _{5,17} – 21 _{5,16} E	169.4	53.7	D	D	D	D	D	D	D	D
285542.584	22 _{5,17} – 21 _{5,16} A	169.4	53.7	D	D	PB	PB	D	D	D	PB
285924.822	23 _{8,16} – 22 _{8,15} A	205.9	51.8	D	D	D	D	D	D	D	–
285940.794	23 _{8,16} – 22 _{8,15} E	205.9	49.9	D	D	D	D	D	D	D	D
285973.267	23 _{8,15} – 22 _{8,14} E	206.0	49.9	D	D	D	D	D	D	D	D
286012.485	23 _{8,15} – 22 _{8,14} A	205.9	51.8	D	D	D	D	D	D	D	D
286467.129 ^b	25 _{11,14} – 25 _{10,15} A	272.2	5.5	PB	ND	ND	ND	ND	ND	ND	ND
286984.997	11 _{6,5} – 10 _{5,5} E	62.8	3.2	PB	ND	ND	ND	ND	ND	ND	ND
286994.417	11 _{6,6} – 10 _{5,5} A	62.8	3.2	PB	ND	ND	ND	ND	ND	ND	ND
287038.552	11 _{6,5} – 10 _{5,6} A	62.8	3.2	D	ND	ND	ND	ND	ND	ND	ND
287094.976	24 _{11,14} – 24 _{10,15} E	257.4	6.3	D	ND	ND	ND	ND	ND	ND	ND
287101.120	24 _{11,13} – 24 _{10,14} E	257.4	6.3	D	ND	ND	ND	ND	ND	ND	ND
287146.630	23 _{7,17} – 22 _{7,16} E	196.4	53.4	D	D	D	D	D	D	D	PB
$\text{H}^{13}\text{COOCH}_3$											
283853.856	23 _{8,16} – 22 _{8,15} E	204.3	52.9	ND*	ND*	ND*	ND*	ND*	ND*	ND*	ND*
286035.726	23 _{7,16} – 22 _{7,15} A	195.0	56.7	ND*	ND*	ND*	ND*	ND*	ND*	ND*	ND*

TABLE 5—*Continued*

Frequency (MHz)	Transition	E_{up} (K)	$S\mu^2$ (D ²)	Note ^a						
				Orion-KL	W51 e2	G19.61-0.23	G29.96-0.02	G24.78+0.08	NGC 6334 IRS 1	Sgr B2(N-LMH)
HCOO ¹³ CH ₃										
284729.511 ^c	27 _{1,27} – 26 _{1,26} E	194.2	71.1	D	D	TD	ND*	ND*	D	TD
284729.537 ^c	27 _{0,27} – 26 _{0,26} E	194.2	71.1	D	D	TD	ND*	ND*	D	TD
284730.102 ^c	27 _{1,27} – 26 _{1,26} A	194.2	71.1	D	D	TD	ND*	ND*	D	TD
284730.127 ^c	27 _{0,27} – 26 _{0,26} A	194.2	71.1	D	D	TD	ND*	ND*	D	TD

^aD: detected, TD: tentative detection, PB: partial blend, ND and ND*: not detected (too faint emission). Also, ND* indicates the ¹³C₁– and ¹³C₂–HCOOCH₃ transitions that are emitting with an intensity less or equal to 3 times the noise level and that we used to constrain our model. The symbol “–” indicates that part of the spectrum has been removed (see Section 2.2.2).

^bThose two transitions are predicted, i.e. not measured.

^cPile-up of these 4 lines. Also the frequencies presented in this table are only computed (i.e. not measured) because there are not experimental data for these transitions available yet.

5.2.3. $HCOO^{13}CH_3$

We report the detection of one transition of $^{13}\text{C}_2\text{-MF}$ toward Orion-KL, W51 e2, NGC 6334 IRS 1 and (tentatively) G19.61-0.23, and Sgr B2(N) (see Fig. 4 and Table 5). More specifically, the spectral feature that we assigned to $^{13}\text{C}_2\text{-HCOOCH}_3$ is a pile-up of four lines with frequencies lying in the range 284729–284730 MHz, with a line-strength of 71 D² and an upper energy level of 194 K (Table 5). Figure 4 exhibits the observed spectrum of the $HCOO^{13}CH_3$ transition emitting at 284730 MHz along with our XCLASS for each sources (reduced χ^2 of about 0.23–0.69). We infer that it is difficult to attribute this spectral feature to another molecule on the basis that:

1. The line rest frequencies of these four lines are predicted with an uncertainty of 0.012 MHz (which corresponds to 0.012 km s⁻¹).
2. Several $^{13}\text{C}_2$ -methyl formate transitions with similar $S\mu^2$ and E_{up} are detected in the ALMA-SV data of Orion-KL (see Section 5.1.). Furthermore their excitation level in Orion-KL is consistent with the emission level of this line (and non detection of other lines) in the APEX data.
3. This is the strongest line in the APEX band and the two next highest $S\mu^2$ lines (at 67 and 61 D²) are respectively blended and at the confusion limit level.

We note that given the sensitivity limit in all the sources except Orion-KL (because of the ALMA-data) we cannot claim a definitive detection of this molecule in the APEX observations.

5.2.4. Isotopic $^{12}\text{C}/^{13}\text{C}$ ratio

Since we do not have definitive detections of the ^{13}C -MF, Table 7 lists the lower limits of the isotopic $^{12}\text{C}/^{13}\text{C}$ ratio that are estimated assuming that the two ^{13}C -MF isotopologues have similar abundances. Please note that the upper limits of the ^{13}C -MF column density have been set by adjusting the observational parameters to the model with a resulting fit constrained by a 3σ upper limit. The quality of our models being still based on the reduced χ^2 calculations¹³.

¹³The reduced χ^2 roughly gives a measure of how the model fit the data over the bandpass.

6. Discussion

6.1. Measurement caveats

The analysis above relies on some assumptions. In the following section we discuss whether they could modify the interpretation of our derived $^{12}\text{C}/^{13}\text{C}$ ratio.

6.1.1. LTE and radiative pumping effects

It is important to note that the above analysis hinges upon the assumption that methyl formate is in LTE, which applies at the high densities in hot cores. We assumed that LTE is a reasonable approximation given that the model fit to the Herschel observations of methyl formate in Orion-KL contained over a thousand emissive transitions which are closely fit using an LTE model (Crockett et al. 2014). A strong IR radiation field could affect the LTE analysis. Among the observed sources, Orion-KL and SgrB2(N) have the strongest IR radiation field. Therefore, if present radiative pumping effects would be the strongest toward those sources. The Herschel observations and analysis of Orion-KL and SgrB2(N) (Crockett et al. 2014; Neill et al. 2014) have shown that **i**) pumping is not needed to fit the lines as LTE closely matches the observed emission; **ii**) there was evidence for radiative pumping in emission lines of other molecules, in particular methanol, but not for methyl formate.

6.1.2. Contamination from strong absorption lines in SgrB2(N)

Contamination from strong absorption lines in SgrB2(N) may also affect methyl formate emission. There are two potential levels of contamination that could be an issue. First is absorption of methyl formate that lies in the foreground envelope. However, all the transitions that we have detected in this study cover fairly high energy levels that are not populated in the envelope (e.g. Neill et al. 2014). Another issue would be contamination from other species with ground state transitions that have similar frequencies; we see no evidence for this in our data.

TABLE 6

^{12}C -MF AND ^{13}C -MF XCLASS MODEL PARAMETERS (SOURCE SIZE, ROTATIONAL TEMPERATURE, COLUMN DENSITY, VELOCITY AND LINE-WIDTH) WHICH REPRODUCE BEST THE APEX SPECTRA.

Source	θ_s ($''$)	T_{rot} (K)	N_{tot} (cm $^{-2}$)			v_{LSR} (km s $^{-1}$)	Δv (km s $^{-1}$)
			HCOOCH $_3$	H 13 COOCH $_3$	HCOO $^{13}\text{CH}_3$		
Sgr B2(N-LMH) ^b	4	80	3.0×10^{17}	$\leq 1.8 \times 10^{16}$	$\leq 1.8 \times 10^{16}$	63.7	7.0
G24.78+0.08 ^c	10	121	6.0×10^{15}	$\leq 3.0 \times 10^{14}$	$\leq 3.0 \times 10^{14}$	111.0	6.0
G29.96-0.02 ^c	10	150	3.5×10^{15}	$\leq 3.0 \times 10^{14}$	$\leq 3.0 \times 10^{14}$	97.8	5.5
G19.61-0.23 ^b	3.3	230	7.0×10^{16}	$\leq 5.0 \times 10^{15}$	$\leq 5.0 \times 10^{15}$	39.7	4.5
NGC 6334 IRS 1 ^a	3	115	4.5×10^{17}	$\leq 2.0 \times 10^{16}$	$\leq 2.0 \times 10^{16}$	-8.0	5.0
W51 e2 ^a	7	176	9.0×10^{16}	$\leq 3.0 \times 10^{15}$	$\leq 3.0 \times 10^{15}$	55.6	8.0
Orion-KL ^a	10	100	9.7×10^{16}	$\leq 1.82 \times 10^{15}$	$\leq 1.82 \times 10^{15}$	7.7	3.7

^aObserved sources where one transition of HCOO $^{13}\text{CH}_3$ is detected.

^bObserved sources where HCOO $^{13}\text{CH}_3$ is tentatively detected.

^cObserved sources where HCOO $^{13}\text{CH}_3$ is not detected.

6.1.3. Scattering on the isotopic ratio of the methyl formate isotopologues within each ALMA spectral window

Another possible caveat of our $^{12}\text{C}/^{13}\text{C}$ ratio estimate is the individual modeling of each sub-band of the ALMA-SV observations of Orion-KL. In our exploration of the ALMA-SV data we found that a large source of uncertainty is an about 10% difference in calibration between sub-bands; that is some sub-bands have a slightly different calibration than other sub-bands. We infer that this is due to some structure (that could be a slope, a curvature or a frequency dependence) in the calibration that affects the band pass and results in this slight measurement uncertainty that exists within a given sub-band.

Based upon this and due to the fact that different sub-bands have different number of lines (see Table 4) we have chosen to fit the $^{12}\text{C}/^{13}\text{C}$ ratio in each sub-band individually and to use the relative errors in the fit from those bands to set the absolute uncertainty to our measurement. Nevertheless, it is important to note that a single set of parameters (not shown here) also fit all the data and give rise, within the uncertainties, to a similar isotopic abundance ratio.

6.2. Comparison of the derived column densities with previous studies

In this section we relate our results to previous studies performed towards our source sample. Our models are not unique and some differences with previously reported result can appear. This is in part due to the different (and more accurate) ^{12}C -MF partition functions used here (see discussion in Section 4. 1). Also, we note that for all the observed sources, the observed v_{LSR} and Δv_{LSR} are also consistent with those in the literature.

Orion-KL: From the ALMA-SV observations of Orion-KL we derived a methyl formate column density over all the spectral windows of $5\text{--}8.5 \times 10^{17}$ cm $^{-2}$ toward the Compact Ridge and of $3.3\text{--}4.3 \times 10^{17}$ cm $^{-2}$ toward the Hot Core-SW. These results are higher by a factor 2–5 with our reported values obtained from observations using the Plateau de Bure Interferometer and performed with a similar synthesized beam ($1.8'' \times 0.8''$, see Favre et al. 2011). This discrepancy can be explained by the fact that in this study we used a different partition function that, as discussed in Section 4. 1, results in a higher inferred ^{12}C -MF abundance compared to the ^{12}C -MF abundance derived using the JPL catalog partition

TABLE 7

 $^{12}\text{C}/^{13}\text{C}-\text{HCOOCH}_3$ RATIO AS MEASURED WITH ALMA AND APEX, RESPECTIVELY.

Source	$^{12}\text{C}/^{13}\text{C}$ for CO CN and $\text{H}_2\text{CO}^{\text{a}}$	$^{12}\text{C}/^{13}\text{C}$ for CO only ^b	$^{12}\text{C}/^{13}\text{C}-\text{HCOOCH}_3^{\text{c}}$
ALMA observations			
Orion-KL – Compact Ridge	74±16	67±17	68.4±10.1
Orion-KL – Hot Core-SW	74±16	67±17	71.4±7.8
APEX observations			
Sgr B2(N-LMH) ^e	19±7	20±8	≥17
G24.78+0.08 ^f	42±11	39±12	≥20
G29.96-0.02 ^f	47±12	44±13	≥11
G19.61-0.23 ^e	49±12	45±13	≥14
NGC 6334 IRS 1 ^d	61±14	56±15	≥23
W51 e2 ^d	70±16	64±17	≥30
Orion-KL ^d	74±16	67±17	≥53

^aBased on the following equation for CO, CN and H_2CO $^{12}\text{C}/^{13}\text{C} = 6.21(1.00)\text{D}_{\text{GC}} + 18.71(7.37)$ from Milam et al. (2005) (see Eq.2).

^bBased on the following equation for CO $^{12}\text{C}/^{13}\text{C} = 5.41(1.07)\text{D}_{\text{GC}} + 19.03(7.90)$ from Milam et al. (2005) (see Eq.1).

^cThis study, assuming that both $^{13}\text{C}_1-\text{MF}$ and $^{13}\text{C}_2-\text{MF}$ isotopologues have similar abundances (i.e. $\frac{^{12}\text{C}-\text{MF}}{^{13}\text{C}_1-\text{MF}} = \frac{^{12}\text{C}-\text{MF}}{^{13}\text{C}_2-\text{MF}}$, see Sec. 5.1 and Fig. 2).

^dObserved sources where one transition of $\text{HCOO}^{13}\text{CH}_3$ is detected.

^eObserved sources where $\text{HCOO}^{13}\text{CH}_3$ is tentatively detected.

^fObserved sources where $\text{HCOO}^{13}\text{CH}_3$ is not detected.

function used by Favre et al. (2011). The spatial and the velocity distribution are in agreement with previous observations (Favre et al. 2011; Friedel & Snyder 2008). We refer to Favre et al. (2011) for a detailed comparison with previous related interferometric and single-dish studies performed by Friedel & Snyder (2008); Beuther et al. (2005); Liu et al. (2002); Remijan et al. (2003); Hollis et al. (2003); Blake et al. (1996, 1987); Schilke et al. (1997); Ziurys & McGonagle (1993).

For the Orion-KL observations carried out with the APEX telescope, the bulk of the HCOOCH_3 emission is well reproduced by a single component model with a rotational temperature of 100 K, a source size of $10''$ and a column density of $9.6 \times 10^{16} \text{ cm}^{-2}$. Our derived APEX rotational temperature and column density agree with the Herschel/HIFI observations (Crockett et al. 2014) as well as with Favre et al. (2011) in which the authors do not separate the two HCOOCH_3 velocity components (T_{rot} of 101 K, $N_{\text{HCOOCH}_3} = 1.5 \times 10^{17} \text{ cm}^{-2}$).

Regarding the $\text{H}^{13}\text{COOCH}_3$ and $\text{HCOO}^{13}\text{CH}_3$ species, their detection towards Orion-KL has previously been reported by Carvajal et al. (2009) based on IRAM-30m observations. The authors used a source size of $15''$, a column density of $7 \times 10^{14} \text{ cm}^{-2}$ and rotational temperature of 110 K to reproduce the emission arising from the Compact Ridge component associated with Orion-KL. The $^{13}\text{C}_2\text{-MF}$ column density, derived from the APEX observations, lies in the range $7\text{--}9.8 \times 10^{15} \text{ cm}^{-2}$ and differs from the one derived by Carvajal et al. (2009). This is likely due to the fact we use a different partition function (see above) along with different assumptions with regard to the beam filling factor (source size of $3''$ and a T_{rot} of 80 K for our best models).

W51 e2: From the APEX observations, we derived a slightly lower (factor 1.8) methyl formate column density in comparison to the measured column density reported by Demyk et al. (2008).

G19.61-0.23: Using CARMA observations ($2''$ resolution), Shiao et al. (2010) have reported a derived column density of $(9\pm2) \times 10^{16} \text{ cm}^{-2}$ given a rotation temperature of 161 K. Likewise, BIMA observations, Remijan et al. (2004) derived from a source average of $2.8''$ a column density in methyl formate of $3.4 \times 10^{17} \text{ cm}^{-2}$ given a temperature of 230 K. In our analysis, we have

adopted the HCOOCH_3 rotation temperature derived by Remijan et al. (2004) rather than the one reported by Shiao et al. (2010). This choice is based upon the fact that Shiao et al. (2010) used a temperature derived from ethyl cyanide observations whereas Remijan et al. (2004) used a rotation temperature based on methyl formate observations themselves. Our best fit results in a methyl formate column density of $7 \times 10^{16} \text{ cm}^{-2}$ with is commensurate with the value derived from the CARMA observations. Regarding the BIMA observations, the difference between the derived column densities is likely due to beam dilution.

G29.96-0.02: Using $2''$ resolution CARMA observations, Shiao et al. (2010) have reported a derived column density of $(4\pm1) \times 10^{16} \text{ cm}^{-2}$ which is in agreement with our results (see Table 6) taking into account the different assumptions on the source size with respect to beam.

G24.78+0.08: The HCOOCH_3 column density derived from the APEX observations (see Table 6) differs from the one derived by Bisschop et al. (2007) likely due to different assumptions with regard to the beam filling factor.

NGC 6334 IRS 1: The deviation observed with values reported by Bisschop et al. (2007) are also likely due to different assumptions with regard to the beam filling factor. Nonetheless, our value of $4.5 \times 10^{17} \text{ cm}^{-2}$ is consistent with the value reported by Zernickel et al. (2012) ($N=7 \times 10^{17} \text{ cm}^{-2}$ for a $3''$ source size) from Herschel/HIFI observations of this region.

Sgr B2(N): Using IRAM-30m observations of SgrB2(N), Belloche et al. (2009) modeled methyl formate emission using two velocity components associated with two sources separated by only $5.3''$ (based on PdBI and ATCA observations, see Belloche et al. 2008). These components differ by about 9 km s^{-1} . Our best model includes only the component emitting at the systemic velocity of the source (i.e. 63.7 km s^{-1}) and our derived parameters are in agreement with the study performed by Belloche et al. (2009).

6.3. Isotopologue detection and sensitivity

Our analysis points out the need for high sensitivity to detect isotopologues of complex molecules. Indeed, due to lack of sensitivity in our APEX observations only one $^{13}\text{C}_2\text{-MF}$ line (pile-

up of four $^{13}\text{C}_2$ transitions with $S\mu^2$ of 71 D²) is detected and, most of the $^{13}\text{C}_1$ -MF transitions emit below and/or at the confusion limit level. In contrast, both ^{13}C -MF isotopologues are detected in observations performed with higher sensitivity (e.g. Carvajal et al. 2009, and this study for the supplementary ALMA data.).

6.4. The ^{13}C budget in the galaxy

From Equation 1 for CO and Equation 2 for CO, CN and H₂CO (Milam et al. 2005) we have calculated the $^{12}\text{C}/^{13}\text{C}$ ratio in CO for each sources observed with the APEX telescope and for ALMA-SV observations of Orion-KL. These values are given in Table 7. Our study shows that the derived lower limits for the APEX $^{12}\text{C}/^{13}\text{C}$ -methyl formate ratios are consistent within the uncertainties with the $^{12}\text{C}/^{13}\text{C}$ ratio in CO for each source. The same conclusion applies for the isotopic ratios derived towards the Orion-KL hot core-SW and compact ridge positions (ALMA-SV data).

6.5. Implications

Numerous measurements of the $^{12}\text{C}/^{13}\text{C}$ isotopic ratio have been performed through several molecular tracers, such as CO and OCS, toward Orion-KL. For example, from OCS and H₂CS isotopologue observations Tercero et al. (2005) have reported an average ratio of 45±20. Using methanol observations, Persson et al. (2007) have found a $^{12}\text{C}/^{13}\text{C}$ isotopic ratio 57±14. Savage et al. (2002) derived a ratio of 43±7 in CN. From ^{13}CO observations, Snell et al. (1984) have reported an average $^{12}\text{CO}/^{13}\text{CO}$ isotopic ratio of 74±9 in the high-velocity outflow of Orion-KL. Likewise, from infrared measurement performed with the Kitt peak Mayall 4m telescope, Scoville et al. (1983) obtained a $^{12}\text{CO}/^{13}\text{CO}$ isotopic ratio of 96±5. Using C¹⁸O observations, Langer & Penzias (1990) and Langer & Penzias (1993) derived ratios of 63±6 and 74±9 according to the observed position. These finding suggest that the gas in Orion-KL does not seem to be heavily fractionated since the $^{12}\text{C}/^{13}\text{C}$ ratio in most simple species is almost the same. Our results are consistent with this finding since:

1. for each ^{13}C -MF isotopologues, the derived isotopic ratios (68.4±10.1 toward the Com-

pact Ridge and of 71.4±7.8 toward the Hot Core-SW, see Fig. 2) are consistent with each other.

2. These results are consistent within the error bars with the values derived for CH₃OH and for CO by Persson et al. (2007), Snell et al. (1984) and Scoville et al. (1983) toward Orion-KL.

Therefore, the present observations do not support methyl formate formation in gas-phase formation from $^{12}\text{C}/^{13}\text{C}$ fractionated gas. In addition, regarding methyl formate gas-phase formation mechanisms, Horn et al. (2004) have shown that there are no very efficient gas-phase pathways to form methyl formate, meaning that there are no efficient primary pathways to form the ^{13}C -MF isotopologues either. One possibility that could lead to the gas phase formation of the ^{13}C -MF isotopologues would be secondary fractionation process involving the ^{12}C -methyl formate itself and $^{13}\text{C}^+$ (E. Herbst, private communication). Such reaction, however are unlikely to occur since high barriers are expected. This would also argue against the possibility of methyl formate gas-phase formation from $^{12}\text{C}/^{13}\text{C}$ fractionated gas. This finding combines with the hypothesis of Wirstrom et al. (2011) strongly suggests that grain surface reactions are likely the main pathways to form methyl formate (^{12}C and ^{13}C).

7. Conclusions

We have investigated the $^{12}\text{C}/^{13}\text{C}$ isotopic ratio in methyl formate toward a sample of massive star-forming regions located over a range of distances from the Galactic center, through observations performed with the APEX telescope. In addition, we have measured the $^{12}\text{C}/^{13}\text{C}$ -methyl formate ratio towards Orion-KL using the ALMA-SV observations. Also, we reported new spectroscopic measurements of the H¹³COOCH₃ and HCOO¹³CH₃ species. Our study is based on this laboratory spectral characterization and points out the importance of these data in deriving accurate partition functions and therefore abundances of methyl formate. Our analysis also points out that to accurately derive a reliable abundance ratio between different species, it is necessary use a homogeneous observational database.

We have performed LTE modeling of the observational data. A multitude of $^{13}\text{C}_1\text{-MF}$ and $^{13}\text{C}_2\text{-MF}$ transitions have been detected in the ALMA-SV observations carried out toward Orion-KL, *i)* confirming the previous detection of the ^{13}C -MF isotopologues reported by Carvajal et al. (2009) and, *ii)* imaging their spatial distribution for the first time. Assuming that the two ^{13}C -MF isotopologues have similar abundances, we reported a $^{12}\text{C}/^{13}\text{C}$ isotopic ratio in methyl formate of 68.4 ± 10.1 and 71.4 ± 7.8 toward the Compact Ridge and Hot Core-SW components, respectively. A salient result is that those measurements are consistent with the $^{12}\text{C}/^{13}\text{C}$ ratio measured in CO and in CH_3OH . Our findings suggest that grain surface chemistry very likely prevails in the formation of methyl formate main and ^{13}C isotopologues.

Regarding the APEX observations, we have reported a tentative detection ($\geq 3\sigma$ level) of the $^{13}\text{C}_2\text{-MF}$ isotopologue towards the following four massive star-forming regions: Sgr B2(N-LMH), NGC 6334 IRS 1, W51 e2 and G19.61-0.23. The derived lower limits for the $^{12}\text{C}/^{13}\text{C}$ -methyl formate ratio are consistent with the $^{12}\text{C}/^{13}\text{C}$ ratio measured in CO showing a increasing ratio with distance from the Galactic centre. A larger source sample and further observations with high sensitivity are essential to confirm this trend.

In addition, we used the Herschel/HIFI spectral tools, that are available to the community (Crockett et al. 2014), to make reliable line identifications and to appreciate where potential line blends may exist. The current work illustrates how to we can merge the legacy of Herschel with other telescopes such as ALMA.

This work was supported by the National Science Foundation under grant 1008800. We are grateful to the *Ministerio de Economía y Competitividad* of Spain by the financial support through the Grant No. FIS2011-28738-C02-02 and to the French Government through the Grant No. ANR-08-BLAN-0054 and the French PCMI (Programme National de Physique Chimie du Milieu Interstellaire). This paper makes use of the following ALMA data: ADS/JAO.ALMA#2011.0.00009.SV. ALMA is a partnership of ESO (representing its member states), NSF (USA) and NINS (Japan), together with NRC (Canada) and NSC and

ASIAA (Taiwan), in cooperation with the Republic of Chile. The Joint ALMA Observatory is operated by ESO, AUI/NRAO and NAOJ. C. F. thanks Dahbia Talbi, Eric Herbst and Anthony Remijan for enlightening discussions. Finally, we thank the anonymous referee for the helpful comments.

Facilities: APEX, Herschel/HIFI, ALMA

A. Partition functions calculations

Several approximations for the partition function have been used, following e.g., Blake et al. (1987), Turner (1991), Oesterling et al. (1999), Groner et al. (2007), Demyk et al. (2008), Maeda et al. (2008b), Favre et al. (2011) and Tudorie et al. (2012). In the present work, the partition function was approximated as the product of the rotational (Q_{rot}), torsional (Q_{tor}) and vibrational (without the torsional contribution, Q_{vib}) contributions (Herzberg 1991) and, is given by:

$$Q = g_{ns} \sum_i (2J_i + 1) e^{-\frac{E_i}{k_B T}} \approx g_{ns} Q_{rot} Q_{tor} Q_{vib}, \quad (\text{A1})$$

where J_i stands for the rotational angular momentum of level i , k_B is the Boltzmann constant, T is the temperature, and E_i is the vibrational-torsional-rotational energy which is referred to the ground vibrational-torsional state as the zero point energy. The nuclear spin degeneracy g_{ns} does not need to be taken into account in the calculations of the partition function because g_{ns} is the same for all MF symmetry states (A_1 , A_2 and E). Based on the $C_{3v}(M)$ symmetry (Bunker & Jensen 1998) $g_{ns} = 16$ for both ^{13}C -MF isotopologues of methyl formate.

When observed intensities are estimated, g_{ns} in the numerator is canceled with that of the denominator inside the partition function. Thus g_{ns} will henceforth be ignored and excluded in the comparisons of partition functions of ^{13}C -MF isotopologues.

A.1. Rotational partition function

The rotational partition function Q_{rot} was obtained using equation 9 of Groner et al. (2007), that is:

$$Q_{rot} = \sum_{J, K_a, K_c} (2J + 1) e^{-\frac{E_i^{(rot)}}{k_B T}}, \quad (\text{A2})$$

where $E_i^{(rot)}$ are the rotational energies, that is, those for the rotational states only in the A -symmetry ground torsional state. The RAM model (Herbst et al. 1984; Hougen et al. 1994; Kleiner 2010) was used to predict the torsional-rotational states as explained before. Also, the torsional-rotational states ($v_t = 0$ and A-symmetry) up to $J = 79$ were included in Eq. (A2), which is enough for the convergence study mentioned above.

A comparison was done with the asymmetric top approximation for the rotational partition function of Herzberg (1991). For sufficiently high temperatures (or small rotational constants):

$$Q_{rot}^{appr} \approx \sqrt{\frac{\pi}{A^{PAM} B^{PAM} C^{PAM}}} \left(\frac{k_B T}{h}\right)^3 \quad (\text{A3})$$

where the rotational constants are referred to the principal axis system, not to the Rho-Axis System. Therefore, an appropriate transformation was performed from the rotational parameters given in Carvajal et al. (2009, 2010).

The rotational partition function computed as a direct sum (Eq. A2) is in general, for both ^{13}C -MF isotopologues, slightly larger than the one for the approximated partition function (Eq. A3), as shown in Table A1. For this reason, we used here the rotational partition function as a direct summation instead of using the approximated partition function (Eq. A3). In Table A1 it can be seen that the differences between Q_{rot} and Q_{rot}^{appr} can be around 1% for $T = 9.375$ K, decreasing for higher temperature to the error range estimated by Herzberg (1991).

TABLE A1

COMPARISON BETWEEN THE ROTATIONAL PARTITION FUNCTION^a COMPUTED AS A DIRECT SUM Q_{rot} (A2) AND AS THE APPROXIMATED EXPRESSION Q_{rot}^{appr} (A3) FOR $^{13}\text{C}_1\text{-MF}$ AND $^{13}\text{C}_2\text{-MF}$.

T(K)	$^{13}\text{C}_1\text{-MF}$		$^{13}\text{C}_2\text{-MF}$	
	Q_{rot}^{appr}	Q_{rot}^b	Q_{rot}^{appr}	Q_{rot}^b
300.0	32682.30	32737.70	33291.76	33289.35
225.0	21227.78	21308.82	21623.63	21672.46
150.0	11554.94	11599.33	11770.41	11797.70
75.0	4085.29	4100.86	4161.47	4170.92
37.50	1444.37	1451.06	1471.30	1475.82
18.75	510.66	514.10	520.18	522.86
9.375	180.55	182.57	183.91	185.67

^aThe nuclear spin degeneracy was not considered in these calculations.

^bThe rotational partition function obtained as a direct sum of energy levels up to $J = 79$ is the used in the final result.

A.2. Torsional partition function

The torsional contribution Q_{tor} to the partition function was obtained through the following formula:

$$Q_{tor}^{v_t \max} = \sum_{v_t=0}^{v_t \max} \left(e^{-\frac{E^{(tor)}(v_t, A)}{k_B T}} + e^{-\frac{E^{(tor)}(v_t, E)}{k_B T}} \right), \quad (\text{A4})$$

where $E^{(tor)}(v_t, A)$ and $E^{(tor)}(v_t, E)$ are the energies of the torsional states with quantum number v_t for the A (A_1 or A_2) and E symmetries, respectively, referred to the $v_t = 0$ ground torsional state, i.e. $E^{(tor)}(v_t = 0, A) = 0 \text{ cm}^{-1}$. Different approximations can be carried out depending on the maximum value v_t^{\max} considered in the equation. The torsional energies used in Eq.(A4) are the following:

- Torsional energies from $v_t = 0$ to $v_t = 2$ computed from the Hamiltonian parameters of the RAM model. The torsional energies of $^{13}\text{C}_1$ -MF are computed with the parameters of Carvajal et al. (2010) and of $^{13}\text{C}_2$ -MF are computed with the parameters of Carvajal et al. (2009). These torsional energies are expected to be very reliable for the $^{13}\text{C}_1$ -MF.
- Torsional energies from $v_t = 3$ to $v_t = 4$ of main species of methyl formate given by Senent et al. (2005) and considered as a good approximation for both ^{13}C -MF isotopologues.
- Torsional energies from $v_t = 5$ to $v_t = 6$ were roughly estimated in the present work, where $E^{(tor)}(v_t = m, A) = m \times E^{(tor)}(v_t = 1, A)$ and $E^{(tor)}(v_t = m, E) = m \times E^{(tor)}(v_t = 1, E)$ and m will take values as 5 or 6. This is only an estimate to understand the contribution of these torsional levels to the torsional partition function, whose contribution is of 3% for $T = 300 \text{ K}$, 1.2% for $T = 225 \text{ K}$, 0.2% for 150 K, etc ... (see Tables A2 and A3).

As the torsional mode is very anharmonic, we cannot use the harmonic approximation for the torsional partition function. From our results (Tables A2 and A3), when computing the torsional partition function, the harmonic approximation could be assumed only for temperatures $T < 100 \text{ K}$. Above $T = 100 \text{ K}$, the anharmonicity has the natural effect of increasing the estimated torsional partition function. This effect can be around 5% at 300 K.

In Tables A2 and A3 the torsional partition function at different approximations are shown for $^{13}\text{C}_1$ -MF and $^{13}\text{C}_2$ -MF isotopologues respectively. It can be noted that for $T = 300 \text{ K}$ the convergence is reached to within 1% when the torsional states above $v_t = 6$ are included. For temperatures $T < 200 \text{ K}$, the contribution of the torsional states above $v_t = 4$ is insignificant. In fact, at temperatures close to 100 K and below, the convergence is reached (within 0.9% at $T = 100 \text{ K}$) when only $v_t = 0, 1$ and 2 are considered.

A.3. Vibrational partition function

In the calculation of the vibrational partition function Q_{vib} , it is expected that for ISM temperatures only the information of the vibrational frequencies at lower energies ($\approx 300 \text{ cm}^{-1}$) is necessary. In order to check the convergence of the vibrational partition function, the contribution of the remaining vibrational modes has been taken into consideration. For this purpose, the harmonic approximation of the vibrational partition function is considered in general as:

$$Q_{vib} = \prod_{i=1}^{3N-7} \frac{1}{1 - e^{E_i^{(vib)} / k_B T}} \quad (\text{A7})$$

where N is the number of atoms of the molecule, and $E_i^{(vib)}$ is the vibrational fundamental frequencies of each vibrational mode of the molecule. As the torsion is treated apart, the product in Eq. (A7) will only expand to the $3N - 7$ small amplitude vibrational modes. It is important to note that no experimental vibrational frequencies exist for the ^{13}C -MF species. Therefore, to take into account the vibrational contribution of

TABLE A2
TORSIONAL PARTITION FUNCTION FOR $^{13}\text{C}_1$ -MF AT DIFFERENT APPROXIMATIONS^a.

T(K)	Q_{tor}^0	Q_{tor}^1	Q_{tor}^2	Q_{tor}^4	Q_{tor}^6 ^b	$Q_{\text{tor}}^{\text{harm}}$ ^c
300.0	1.99994	3.06540	3.71217	4.39180	4.52333	4.28020
225.0	1.99991	2.86364	3.30761	3.68701	3.73003	3.52028
150.0	1.99987	2.56748	2.77670	2.89625	2.90098	2.79253
75.0	1.99974	2.16083	2.18274	2.18678	2.18679	2.17520
37.50	1.99948	2.01246	2.01270	2.01270	2.01270	2.01306
18.75	1.99896	1.99905	1.99905	1.99905	1.99905	2.00008
9.375	1.99793	1.99793	1.99793	1.99793	1.99793	2.00000

^aThe approximations are carried out by considering a number of torsional states up to a maximum quantum number v_t^{\max} in Eq. (A4).

^bComputed torsional partition function used as a final result in the present work.

^cHarmonic approximation for the torsional partition function:

$$Q_{\text{tor}}^{\text{harm}} = \frac{1}{1 - e^{-\frac{E(\text{tor})(v_t=1, A)}{k_B T}}} + \frac{1}{1 - e^{-\frac{E(\text{tor})(v_t=1, E)}{k_B T}}} \quad (\text{A5})$$

TABLE A3
TORSIONAL PARTITION FUNCTION FOR $^{13}\text{C}_2$ -MF AT DIFFERENT APPROXIMATIONS^a.

T(K)	Q_{tor}^0	Q_{tor}^1	Q_{tor}^2	Q_{tor}^4	Q_{tor}^6 ^b	$Q_{\text{tor}}^{\text{harm}}$ ^c
300.0	1.99994	3.07133	3.69952	4.37914	4.51465	4.30756
225.0	1.99991	2.87006	3.29709	3.67650	3.72124	3.54028
150.0	1.99987	2.57382	2.77116	2.89072	2.89573	2.80495
75.0	1.99974	2.16445	2.18394	2.18798	2.18798	2.17949
37.50	1.99948	2.01305	2.01324	2.01324	2.01324	2.01366
18.75	1.99896	1.99906	1.99906	1.99906	1.99906	2.00009
9.375	1.99793	1.99793	1.99793	1.99793	1.99793	2.00000

^aThe approximations are carried out by considering a number of torsional states up to a maximum quantum number v_t^{\max} in Eq. (A4).

^bComputed torsional partition function used as a final result in the present work.

^cHarmonic approximation for the torsional partition function:

$$Q_{\text{tor}}^{\text{harm}} = \frac{1}{1 - e^{-\frac{E(\text{tor})(v_t=1, A)}{k_B T}}} + \frac{1}{1 - e^{-\frac{E(\text{tor})(v_t=1, E)}{k_B T}}} \quad (\text{A6})$$

the partition function, we assumed that the vibrational fundamental frequencies of $^{13}\text{C}_1\text{-MF}$ and $^{13}\text{C}_2\text{-MF}$ are approximately the same as for the main isotopologue, given the large experimental uncertainties (mostly of 6–15 cm^{-1} , Chao et al. 1986). In this instance, the experimental vibrational energies for the main isotopologue taken from Chao et al. (1986) are also valid for their other isotopologues. The vibrational partition function computed with Eq. (A7) is given in Table A4.

In this work, for the temperature ranges considered, all the small amplitude vibrational fundamentals in Eq. (A7) are included. Nevertheless, when the temperatures are around $T = 200$ K, all vibrational fundamentals could be omitted in the vibrational partition function except those of ν_{14} and ν_1 modes (around 300 cm^{-1}). Below $T = 100$ K, inclusively ν_{14} and ν_1 modes could be neglected.

A.4. Rotational-torsional-vibrational partition function

In addition, we have assessed that the partition function separated into functions of each rotational, torsional and vibrational contribution is a good enough approximation for temperatures at least under 300 K. This assessment was set up after comparing our partition function calculation with that derived from its general expression, Eq. 3, for $v_t = 0$ and 1. Finally, Table 3 summarizes the rotational-torsional-vibrational partition function values that are used here for $^{13}\text{C}_1\text{-MF}$ and $^{13}\text{C}_2\text{-MF}$.

TABLE A4
VIBRATIONAL PARTITION FUNCTION FOR $^{13}\text{C}_1\text{-MF}$ AND $^{13}\text{C}_2\text{-MF}$.

T(K)	Q_{vib}
300.0	1.70330
225.0	1.32486
150.0	1.09599
75.0	1.00397
37.50	1.00001
18.75	1.00000
9.375	1.00000

B. Transitions of ^{12}C and ^{13}C -methyl formate observed with the ALMA telescope toward Orion-KL

Table B1 summarizes the line parameters for all detected, blended, or not detected transitions of ^{12}C -MF, $^{13}\text{C}_1$ -MF and $^{13}\text{C}_2$ -MF in all ALMA spectral windows.

TABLE B1

TRANSITIONS OF ^{12}C AND ^{13}C -METHYL FORMATE OBSERVED WITH THE ALMA TELESCOPE.

Frequency (MHz)	Transition	E_{up} (K)	$S\mu^2$ (D 2)
HCOOCH ₃ ^a			
214631.77 *	17 _{5,12} – 16 _{5,11} (E, v _t =0)	108	41
214652.63 *	17 _{5,12} – 16 _{5,11} (A, v _t =0)	108	41
214782.36 *	18 _{3,16} – 17 _{3,15} (E, v _t =0)	106	46
214792.55 *	18 _{3,16} – 17 _{3,15} (A, v _t =0)	106	46
214816.95	19 _{2,18} – 18 _{2,17} (A, v _t =1)	296	49
214942.87	19 _{1,18} – 18 _{1,17} (A, v _t =1)	296	49
215073.92	19 _{2,18} – 18 _{2,17} (E, v _t =1)	296	49
215193.55	19 _{1,18} – 18 _{1,17} (E, v _t =1)	296	49
215579.61	18 _{2,16} – 17 _{2,15} (A, v _t =1)	293	46
215837.59	20 _{1,20} – 19 _{1,19} (A, v _t =1)	299	53
215839.54	20 _{0,20} – 19 _{0,19} (A, v _t =1)	299	53
215891.90	20 _{1,20} – 19 _{1,19} (E, v _t =1)	298	53
215893.71	20 _{0,20} – 19 _{0,19} (E, v _t =1)	298	53
215979.94	18 _{2,16} – 17 _{2,15} (E, v _t =1)	292	46
216109.78 *	19 _{2,18} – 18 _{2,17} (E, v _t =0)	109	49
216115.57 *	19 _{2,18} – 18 _{2,17} (A, v _t =0)	109	49
216210.91 *	19 _{1,18} – 18 _{1,17} (E, v _t =0)	109	49
216216.54 *	19 _{1,18} – 18 _{1,17} (A, v _t =0)	109	49
216327.07	17 _{3,14} – 16 _{3,13} (A, v _t =1)	286	44
216830.20 *	18 _{2,16} – 17 _{2,15} (E, v _t =0)	106	46
216838.89 *	18 _{2,16} – 17 _{2,15} (A, v _t =0)	106	46
216958.83	17 _{3,14} – 16 _{3,13} (E, v _t =1)	286	44
216964.77 *	20 _{1,20} – 19 _{1,19} (E, v _t =0)	111	53
216965.90 *	20 _{1,20} – 19 _{1,19} (A, v _t =0)	111	53
216966.25 *	20 _{0,20} – 19 _{0,19} (E, v _t =0)	111	53
216967.42 *	20 _{0,20} – 19 _{0,19} (A, v _t =0)	111	53
217262.88	37 _{10,27} – 37 _{9,28} (A, v _t =0)	485	10
217312.63	17 _{4,13} – 16 _{4,12} (A, v _t =1)	290	43
217337.97	37 _{10,27} – 37 _{9,28} (E, v _t =0)	485	10
218108.44	17 _{4,13} – 16 _{4,12} (E, v _t =1)	290	43
218280.90 *	17 _{3,14} – 16 _{3,13} (E, v _t =0)	100	44
218297.89 *	17 _{3,14} – 16 _{3,13} (A, v _t =0)	100	44
218654.67	18 _{16,2} – 17 _{16,1} (E, v _t =1)	460	10
218680.78	18 _{15,3} – 17 _{15,2} (E, v _t =1)	439	15
218737.73	18 _{14,4} – 17 _{14,3} (E, v _t =1)	419	19
218830.59	18 _{13,5} – 17 _{13,4} (E, v _t =1)	401	23
218966.15	18 _{12,6} – 17 _{12,5} (E, v _t =1)	384	27
219154.53	18 _{11,7} – 17 _{11,6} (E, v _t =1)	369	30
219194.67	18 _{16,3} – 17 _{16,2} (E, v _t =1)	459	10
219331.19	18 _{15,4} – 17 _{15,3} (E, v _t =1)	438	15
219411.70	18 _{10,8} – 17 _{10,7} (E, v _t =1)	355	33
219479.12	18 _{14,5} – 17 _{14,4} (E, v _t =1)	419	19
219566.24	18 _{15,3} – 17 _{15,2} (A, v _t =1)	438	15
219566.24	18 _{15,4} – 17 _{15,3} (A, v _t =1)	438	15
219568.48	18 _{14,4} – 17 _{14,3} (A, v _t =1)	419	19
219568.48	18 _{14,5} – 17 _{14,4} (A, v _t =1)	419	19
219571.20	18 _{16,2} – 17 _{16,1} (A, v _t =1)	459	10

TABLE B1—*Continued*

Frequency (MHz)	Transition	E_{up} (K)	$S\mu^2$ (D ²)
219571.20	1816,3 – 17 _{16,2} (A, v _t =1)	459	10
219584.38	1813,5 – 17 _{13,4} (A, v _t =1)	401	23
219584.38	1813,6 – 17 _{13,5} (A, v _t =1)	401	23
219622.69	1812,6 – 17 _{12,5} (A, v _t =1)	384	27
219622.69	1812,7 – 17 _{12,6} (A, v _t =1)	384	27
219642.40	1813,6 – 17 _{13,5} (E, v _t =1)	401	23
219695.83	1811,7 – 17 _{11,6} (A, v _t =1)	369	30
219695.83	1811,8 – 17 _{11,7} (A, v _t =1)	369	30
219705.13	184,15 – 17 _{4,14} (A, v _t =1)	299	45
219763.95	189,9 – 17 _{9,8} (E, v _t =1)	342	36
219822.13	1810,9 – 17 _{10,8} (A, v _t =1)	355	33
219822.13	1810,8 – 17 _{10,7} (A, v _t =1)	355	33
219827.15	1812,7 – 17 _{12,6} (E, v _t =1)	384	27
220030.34	189,10 – 17 _{9,9} (A, v _t =1)	342	36
220030.34	189,9 – 17 _{9,8} (A, v _t =1)	342	36
220043.34	1811,8 – 17 _{11,7} (E, v _t =1)	368	30
220166.89 *	174,13 – 16 _{4,12} (E, v _t =0)	103	43
220190.29 *	174,13 – 16 _{4,12} (A, v _t =0)	103	43
220307.38	1810,9 – 17 _{10,8} (E, v _t =1)	354	33
220368.33	188,11 – 17 _{8,10} (A, v _t =1)	331	38
220369.88	188,10 – 17 _{8,9} (A, v _t =1)	331	38
220408.75	184,15 – 17 _{4,14} (E, v _t =1)	299	45
220646.82	189,10 – 17 _{9,9} (E, v _t =1)	342	36
220913.95	187,12 – 17 _{7,11} (A, v _t =1)	321	41
220926.36	1816,3 – 17 _{16,2} (A, v _t =0)	271	10
220926.36	1816,2 – 17 _{16,1} (A, v _t =0)	271	10
220935.45	1816,2 – 17 _{16,1} (E, v _t =0)	271	10
220946.35	187,11 – 17 _{7,10} (A, v _t =1)	321	41
220946.87	379,29 – 37 _{8,30} (A, v _t =0)	473	10
220947.42	1816,3 – 17 _{16,2} (E, v _t =0)	271	10
220966.61	379,29 – 37 _{8,30} (E, v _t =0)	473	10
220977.98	1815,4 – 17 _{15,3} (A, v _t =0)	250	15
220977.98	1815,3 – 17 _{15,2} (A, v _t =0)	250	15
220983.67	1815,3 – 17 _{15,2} (E, v _t =0)	250	15
220985.33	187,11 – 17 _{7,10} (E, v _t =1)	321	41
220998.33	1815,4 – 17 _{15,3} (E, v _t =0)	250	15
221047.79 *	1814,5 – 17 _{14,4} (A, v _t =0)	231	19
221047.79 *	1814,4 – 17 _{14,3} (A, v _t =0)	231	19
221049.99 *	1814,4 – 17 _{14,3} (E, v _t =0)	231	19
221066.93	1814,5 – 17 _{14,4} (E, v _t =0)	231	19
221110.67	188,11 – 17 _{8,10} (E, v _t =1)	330	39
221139.73 *	1813,5 – 17 _{13,4} (E, v _t =0)	213	23
221141.13 *	1813,6 – 17 _{13,5} (A, v _t =0)	213	23
221141.13 *	1813,5 – 17 _{13,4} (A, v _t =0)	213	23
221158.54 *	1813,6 – 17 _{13,5} (E, v _t =0)	213	23
221260.77 *	1812,6 – 17 _{12,5} (E, v _t =0)	196	27
221265.70 *	1812,7 – 17 _{12,6} (A, v _t =0)	196	27
221265.70 *	1812,6 – 17 _{12,5} (A, v _t =0)	196	27
221280.90 *	1812,7 – 17 _{12,6} (E, v _t =0)	196	27

TABLE B1—*Continued*

Frequency (MHz)	Transition	E_{up} (K)	$S\mu^2$ (D ²)
221424.64 *	1811,7 – 1711,6 (E, v _t =0)	181	30
221433.02 *	1811,7 – 1711,6 (A, v _t =0)	181	30
221433.02 *	1811,8 – 1711,7 (A, v _t =0)	181	30
221445.64 *	1811,8 – 1711,7 (E, v _t =0)	181	30
221649.41 *	1810,8 – 1710,7 (E, v _t =0)	167	33
221660.48 *	184,15 – 174,14 (E, v _t =0)	112	45
221661.04 *	1810,8 – 1710,7 (A, v _t =0)	167	33
221661.04 *	1810,9 – 1710,8 (A, v _t =0)	167	33
221670.77 *	1810,9 – 1710,8 (E, v _t =0)	167	33
221674.67 *	184,15 – 174,14 (A, v _t =0)	112	45
221692.34	186,13 – 176,12 (A, v _t =1)	312	43
221794.42	187,12 – 177,11 (E, v _t =1)	320	41
221964.42 *	189,9 – 179,8 (E, v _t =0)	155	36
221964.42 *	189,9 – 179,8 (E, v _t =0)	155	36
221979.38 *	189,10 – 179,9 (A, v _t =0)	155	36
221979.38 *	189,9 – 179,8 (A, v _t =0)	155	36
221985.72 *	189,10 – 179,9 (E, v _t =0)	155	36
222025.96	185,14 – 175,13 (A, v _t =1)	305	44
222148.84	186,12 – 176,11 (A, v _t =1)	312	43
222177.10	186,12 – 176,11 (E, v _t =1)	312	43
222421.49 *	188,10 – 178,9 (E, v _t =0)	143	38
222438.29 *	188,11 – 178,10 (A, v _t =0)	143	38
222440.39 *	188,10 – 178,9 (A, v _t =0)	143	38
222442.09 *	188,11 – 178,10 (E, v _t =0)	143	38
222899.49	186,13 – 176,12 (E, v _t =1)	312	43
223119.27 *	187,12 – 177,11 (A, v _t =0)	134	41
223125.09 *	187,11 – 177,10 (E, v _t =0)	134	40
223135.02 *	187,12 – 177,11 (E, v _t =0)	134	40
223162.74 *	187,11 – 177,10 (A, v _t =0)	134	41
223534.73	185,14 – 175,13 (E, v _t =1)	305	43
224021.87 *	186,13 – 176,12 (E, v _t =0)	125	42
224024.10 *	186,13 – 176,12 (A, v _t =0)	125	43
224056.67	193,17 – 183,16 (A, v _t =1)	304	49
224296.04	389,30 – 388,31 (A, v _t =0)	496	10
224313.15 *	185,14 – 175,13 (E, v _t =0)	118	44
224313.15	389,30 – 388,31 (E, v _t =0)	496	10
224328.31 *	185,14 – 175,13 (A, v _t =0)	118	44
224491.31	193,17 – 183,16 (E, v _t =1)	303	49
224582.35 *	186,12 – 176,11 (E, v _t =0)	125	42
224609.38 *	186,12 – 176,11 (A, v _t =0)	125	43
225372.22	202,19 – 192,18 (A, v _t =1)	307	52
225448.62	201,19 – 191,18 (A, v _t =1)	307	52
225608.82 *	193,17 – 183,16 (E, v _t =0)	117	49
225618.73 *	193,17 – 183,16 (A, v _t =0)	117	49
225624.90	202,19 – 192,18 (E, v _t =1)	307	52
225648.42	185,13 – 175,12 (A, v _t =1)	306	44
225696.84	201,19 – 191,18 (E, v _t =1)	307	52
225702.86	192,17 – 182,16 (A, v _t =1)	303	49
225756.20	185,13 – 175,12 (E, v _t =1)	305	43

TABLE B1—Continued

Frequency (MHz)	Transition	E_{up} (K)	$S\mu^2$ (D ²)
226090.30	19 _{2,17} – 18 _{2,16} (E, v _t =1)	303	49
226382.72 *	21 _{1,21} – 20 _{1,20} (A, v _t =1)	310	55
226383.86 *	21 _{0,21} – 20 _{0,20} (A, v _t =1)	310	55
226434.47 *	21 _{1,21} – 20 _{1,20} (E, v _t =1)	309	56
226435.52 *	21 _{0,21} – 20 _{0,20} (E, v _t =1)	309	56
226713.06 *	20 _{2,19} – 19 _{2,18} (E, v _t =0)	120	52
226718.69 *	20 _{2,19} – 19 _{2,18} (A, v _t =0)	120	52
226773.13 *	20 _{1,19} – 19 _{1,18} (E, v _t =0)	120	52
226778.79 *	20 _{1,19} – 19 _{1,18} (A, v _t =0)	120	52
227019.55 *	19 _{2,17} – 18 _{2,16} (E, v _t =0)	117	49
227028.12 *	19 _{2,17} – 18 _{2,16} (A, v _t =0)	116	49
227560.94 *	21 _{1,21} – 20 _{1,20} (E, v _t =0)	122	55
227561.74 *	21 _{0,21} – 20 _{0,20} (E, v _t =0)	122	55
227561.99 *	21 _{1,21} – 20 _{1,20} (A, v _t =0)	122	55
227562.79 *	21 _{0,21} – 20 _{0,20} (A, v _t =0)	122	55
227599.26	18 _{3,15} – 17 _{3,14} (A, v _t =1)	297	46
228211.29	18 _{3,15} – 17 _{3,14} (E, v _t =1)	297	46
228628.88 *	18 _{5,13} – 17 _{5,12} (E, v _t =0)	119	44
228651.40 *	18 _{5,13} – 17 _{5,12} (A, v _t =0)	119	44
229405.02 *	18 _{3,15} – 17 _{3,14} (E, v _t =0)	111	46
229420.34 *	18 _{3,15} – 17 _{3,14} (A, v _t =0)	111	46
230844.49	19 _{17,2} – 18 _{17,1} (E, v _t =1)	493	10
230851.69	19 _{16,3} – 18 _{16,2} (E, v _t =1)	471	15
230878.81	18 _{4,14} – 17 _{4,13} (A, v _t =1)	301	46
230888.68	19 _{15,4} – 18 _{15,3} (E, v _t =1)	450	19
230959.93	19 _{14,5} – 18 _{14,4} (E, v _t =1)	430	23
231071.20	19 _{13,6} – 18 _{13,5} (E, v _t =1)	412	27
231230.68	19 _{12,7} – 18 _{12,6} (E, v _t =1)	395	30
231245.42	19 _{4,16} – 18 _{4,15} (A, v _t =1)	310	48
231278.96	19 _{17,3} – 18 _{17,2} (E, v _t =1)	492	10
231418.46	19 _{16,4} – 18 _{16,3} (E, v _t =1)	470	15
231450.50	19 _{11,8} – 18 _{11,7} (E, v _t =1)	380	34
231569.55	19 _{15,5} – 18 _{15,4} (E, v _t =1)	449	19
231724.16	18 _{4,14} – 17 _{4,13} (E, v _t =1)	301	46
231734.86	19 _{14,6} – 18 _{14,5} (E, v _t =1)	430	23
231749.76	19 _{10,9} – 18 _{10,8} (E, v _t =1)	366	37
231800.93	19 _{16,4} – 18 _{16,3} (A, v _t =1)	470	15
231800.93	19 _{16,3} – 18 _{16,2} (A, v _t =1)	470	15
231801.95	19 _{17,3} – 18 _{17,2} (A, v _t =1)	492	10
231801.95	19 _{17,2} – 18 _{17,1} (A, v _t =1)	492	10
231804.11	19 _{15,5} – 18 _{15,4} (A, v _t =1)	449	19
231804.11	19 _{15,4} – 18 _{15,3} (A, v _t =1)	449	19
231816.99	19 _{14,6} – 18 _{14,5} (A, v _t =1)	430	23
231816.99	19 _{14,5} – 18 _{14,4} (A, v _t =1)	430	23
231846.82	19 _{13,6} – 18 _{13,5} (A, v _t =1)	412	27
231846.82	19 _{13,7} – 18 _{13,6} (A, v _t =1)	412	27
231896.06	19 _{4,16} – 18 _{4,15} (E, v _t =1)	310	48
231903.90	19 _{12,7} – 18 _{12,6} (A, v _t =1)	395	30
231903.90	19 _{12,8} – 18 _{12,7} (A, v _t =1)	395	30

TABLE B1—*Continued*

Frequency (MHz)	Transition	E_{up} (K)	$S\mu^2$ (D ²)
231918.95	19 _{13,7} – 18 _{13,6} (E, v _t =1)	412	27
232002.60	19 _{11,9} – 18 _{11,8} (A, v _t =1)	380	34
232002.60	19 _{11,8} – 18 _{11,7} (A, v _t =1)	380	34
232129.22	19 _{12,8} – 18 _{12,7} (E, v _t =1)	395	31
232160.19	19 _{9,10} – 18 _{9,9} (E, v _t =1)	353	39
232164.44	19 _{10,10} – 18 _{10,9} (A, v _t =1)	366	37
232164.44	19 _{10,9} – 18 _{10,8} (A, v _t =1)	366	37
232377.70	19 _{11,9} – 18 _{11,8} (E, v _t =1)	379	34
232423.45	19 _{9,10} – 18 _{9,9} (A, v _t =1)	353	39
232423.45	19 _{9,11} – 18 _{9,10} (A, v _t =1)	353	39
232683.93	19 _{10,10} – 18 _{10,9} (E, v _t =1)	365	37
232738.62	19 _{8,11} – 18 _{8,10} (E, v _t =1)	342	42
232836.17	19 _{8,12} – 18 _{8,11} (A, v _t =1)	342	42
232839.68	19 _{8,11} – 18 _{8,10} (A, v _t =1)	342	42
233080.84	19 _{9,11} – 18 _{9,10} (E, v _t =1)	353	39
233200.21	19 _{17,3} – 18 _{17,2} (A, v _t =0)	304	10
233200.21	19 _{17,2} – 18 _{17,1} (A, v _t =0)	304	10
233212.77 *	19 _{4,16} – 18 _{4,15} (E, v _t =0)	123	48
233212.77 *	19 _{17,2} – 18 _{17,1} (E, v _t =0)	304	10
233222.22	19 _{17,3} – 18 _{17,2} (E, v _t =0)	304	10
233226.79 *	19 _{4,16} – 18 _{4,15} (A, v _t =0)	123	48
233246.79	19 _{16,4} – 18 _{16,3} (A, v _t =0)	282	15
233246.79	19 _{16,3} – 18 _{16,2} (A, v _t =0)	282	15
233256.01	19 _{16,3} – 18 _{16,2} (E, v _t =0)	282	15
233268.59	19 _{16,4} – 18 _{16,3} (E, v _t =0)	282	15
233310.12 *	19 _{15,5} – 18 _{15,4} (A, v _t =0)	261	19
233310.12 *	19 _{15,4} – 18 _{15,3} (A, v _t =0)	261	19
233315.78	19 _{15,4} – 18 _{15,3} (E, v _t =0)	261	19
233331.21	19 _{15,5} – 18 _{15,4} (E, v _t =0)	261	19
233394.65 *	19 _{14,5} – 18 _{14,4} (A, v _t =0)	242	23
233394.65 *	19 _{14,6} – 18 _{14,5} (A, v _t =0)	242	23
233396.68 *	19 _{14,5} – 18 _{14,4} (E, v _t =0)	242	23
233414.43	19 _{14,6} – 18 _{14,5} (E, v _t =0)	242	23
233487.68	19 _{7,13} – 18 _{7,12} (A, v _t =1)	332	44
233504.98 *	19 _{13,6} – 18 _{13,5} (E, v _t =0)	224	27
233506.69 *	19 _{13,6} – 18 _{13,5} (A, v _t =0)	224	27
233506.69 *	19 _{13,7} – 18 _{13,6} (A, v _t =0)	224	27
233524.63 *	19 _{13,7} – 18 _{13,6} (E, v _t =0)	224	27
233553.23	19 _{7,12} – 18 _{7,11} (A, v _t =1)	332	44
233598.10	19 _{7,12} – 18 _{7,11} (E, v _t =1)	332	44
233627.48	19 _{8,12} – 18 _{8,11} (E, v _t =1)	341	42
233649.88 *	19 _{12,7} – 18 _{12,6} (E, v _t =0)	208	30
233655.34 *	19 _{12,8} – 18 _{12,7} (A, v _t =0)	208	30
233655.34 *	19 _{12,7} – 18 _{12,6} (A, v _t =0)	208	30
233670.98 *	19 _{12,8} – 18 _{12,7} (E, v _t =0)	208	30
233753.96 *	18 _{4,14} – 17 _{4,13} (E, v _t =0)	114	46
233777.52 *	18 _{4,14} – 17 _{4,13} (A, v _t =0)	114	46
233845.23 *	19 _{11,8} – 18 _{11,7} (E, v _t =0)	192	34
233854.29 *	19 _{11,8} – 18 _{11,7} (A, v _t =0)	192	34

TABLE B1—*Continued*

Frequency (MHz)	Transition	E_{up} (K)	$S\mu^2$ (D ²)
233854.29 *	19 _{11,9} – 18 _{11,8} (A, v _t =0)	192	34
233867.19 *	19 _{11,9} – 18 _{11,8} (E, v _t =0)	192	34
234112.33 *	19 _{10,9} – 18 _{10,8} (E, v _t =0)	178	37
234124.88 *	19 _{10,10} – 18 _{10,9} (A, v _t =0)	178	37
234124.88 *	19 _{10,9} – 18 _{10,8} (A, v _t =0)	178	37
234134.60 *	19 _{10,10} – 18 _{10,9} (E, v _t =0)	178	37
234336.11	19 _{6,14} – 18 _{6,13} (A, v _t =1)	323	45
234381.27	19 _{5,15} – 18 _{5,14} (A, v _t =1)	316	47
234441.26	19 _{7,13} – 18 _{7,12} (E, v _t =1)	331	44
234486.39 *	19 _{9,10} – 18 _{9,9} (E, v _t =0)	166	39
234502.24 *	19 _{9,11} – 18 _{9,10} (A, v _t =0)	166	39
234502.43 *	19 _{9,10} – 18 _{9,9} (A, v _t =0)	166	39
234508.61 *	19 _{9,11} – 18 _{9,10} (E, v _t =0)	166	39
234778.92	20 _{3,18} – 19 _{3,17} (A, v _t =1)	315	51
235029.95 *	19 _{8,11} – 18 _{8,10} (E, v _t =0)	155	42
235046.49 *	19 _{8,12} – 18 _{8,11} (A, v _t =0)	155	42
235051.38 *	19 _{8,12} – 18 _{8,11} (E, v _t =0)	155	42
235051.38 *	19 _{8,11} – 18 _{8,10} (A, v _t =0)	155	42
235084.74	19 _{6,13} – 18 _{6,12} (E, v _t =1)	323	45
235135.91	19 _{6,13} – 18 _{6,12} (A, v _t =1)	324	45
235200.42	20 _{3,18} – 19 _{3,17} (E, v _t =1)	314	51
235633.06	19 _{5,15} – 18 _{5,14} (E, v _t =1)	316	46
235732.08	19 _{6,14} – 18 _{6,13} (E, v _t =1)	323	45
235844.54 *	19 _{7,13} – 18 _{7,12} (A, v _t =0)	145	44
235865.97 *	19 _{7,13} – 18 _{7,12} (E, v _t =0)	145	43
235887.11 *	19 _{7,12} – 18 _{7,11} (E, v _t =0)	145	43
235904.65	20 _{2,18} – 19 _{2,17} (A, v _t =1)	315	51
235919.35	21 _{2,20} – 20 _{2,19} (A, v _t =1)	319	55
235932.38 *	19 _{7,12} – 18 _{7,11} (A, v _t =0)	145	44
235965.22	21 _{1,20} – 20 _{1,19} (A, v _t =1)	319	55
236168.16	21 _{2,20} – 20 _{2,19} (E, v _t =1)	318	55
236210.97	21 _{1,20} – 20 _{1,19} (E, v _t =1)	318	55
236284.77	20 _{2,18} – 19 _{2,17} (E, v _t =1)	314	52
236355.95 *	20 _{3,18} – 19 _{3,17} (E, v _t =0)	128	51
236365.57 *	20 _{3,18} – 19 _{3,17} (A, v _t =0)	128	51
236743.70 *	19 _{5,15} – 18 _{5,14} (E, v _t =0)	130	47
236759.69 *	19 _{5,15} – 18 _{5,14} (A, v _t =0)	130	47
236800.59 *	19 _{6,14} – 18 _{6,13} (E, v _t =0)	137	45
236810.31 *	19 _{6,14} – 18 _{6,13} (A, v _t =0)	137	46
236926.61 *	22 _{1,22} – 21 _{1,21} (A, v _t =1)	321	58
236927.21 *	22 _{0,22} – 21 _{0,21} (A, v _t =1)	321	58
236975.84 *	22 _{1,22} – 21 _{1,21} (E, v _t =1)	320	58
236976.39 *	22 _{0,22} – 21 _{0,21} (E, v _t =1)	320	58
237297.48 *	20 _{2,18} – 19 _{2,17} (E, v _t =0)	128	51
237305.97 *	20 _{2,18} – 19 _{2,17} (A, v _t =0)	128	51
237309.54 *	21 _{2,20} – 20 _{2,19} (E, v _t =0)	132	55
237315.08 *	21 _{2,20} – 20 _{2,19} (A, v _t =0)	132	55
237344.87 *	21 _{1,20} – 20 _{1,19} (E, v _t =0)	132	55
237350.39 *	21 _{1,20} – 20 _{1,19} (A, v _t =0)	132	55

TABLE B1—Continued

Frequency (MHz)	Transition	E_{up} (K)	$S\mu^2$ (D ²)
237807.63 *	19 _{6,13} – 18 _{6,12} (E, v _t =0)	137	45
237829.83 *	19 _{6,13} – 18 _{6,12} (A, v _t =0)	137	46
238155.88 *	22 _{1,22} – 21 _{1,21} (E, v _t =0)	134	58
238156.31 *	22 _{0,22} – 21 _{0,21} (E, v _t =0)	134	58
238156.86 *	22 _{1,22} – 21 _{1,21} (A, v _t =0)	134	58
238157.30 *	22 _{0,22} – 21 _{0,21} (A, v _t =0)	134	58
238368.80	19 _{3,16} – 18 _{3,15} (A, v _t =1)	309	49
238947.23	19 _{3,16} – 18 _{3,15} (E, v _t =1)	309	49
239240.92	37 _{10,28} – 37 _{9,29} (A, v _t =0)	485	10
239278.43	37 _{10,28} – 37 _{9,29} (E, v _t =0)	485	10
239610.15	19 _{5,14} – 18 _{5,13} (A, v _t =1)	317	47
240021.14 *	19 _{3,16} – 18 _{3,15} (E, v _t =0)	122	49
240034.67 *	19 _{3,16} – 18 _{3,15} (A, v _t =0)	122	49
240089.52	19 _{5,14} – 18 _{5,13} (E, v _t =1)	317	47
242610.07	20 _{4,17} – 19 _{4,16} (A, v _t =1)	322	51
242871.57 *	19 _{5,14} – 18 _{5,13} (E, v _t =0)	130	47
242896.02 *	19 _{5,14} – 18 _{5,13} (A, v _t =0)	130	47
243039.91	20 _{17,3} – 19 _{17,2} (E, v _t =1)	504	15
243056.77	20 _{16,4} – 19 _{16,3} (E, v _t =1)	482	19
243106.25	20 _{15,5} – 19 _{15,4} (E, v _t =1)	462	23
243193.52	20 _{14,6} – 19 _{14,5} (E, v _t =1)	442	27
243223.38	20 _{4,17} – 19 _{4,16} (E, v _t =1)	321	51
243325.37	20 _{13,7} – 19 _{13,6} (E, v _t =1)	424	31
243496.50	20 _{17,4} – 19 _{17,3} (E, v _t =1)	504	15
243511.47	20 _{12,8} – 19 _{12,7} (E, v _t =1)	407	34
243649.49	20 _{16,5} – 19 _{16,4} (E, v _t =1)	482	19
243766.26	20 _{11,9} – 19 _{11,8} (E, v _t =1)	392	37
243816.35	20 _{15,6} – 19 _{15,5} (E, v _t =1)	461	23
244000.39	20 _{14,7} – 19 _{14,6} (E, v _t =1)	442	27
244029.18	20 _{17,3} – 19 _{17,2} (A, v _t =1)	504	15
244029.18	20 _{17,4} – 19 _{17,3} (A, v _t =1)	504	15
244035.70	20 _{16,5} – 19 _{16,4} (A, v _t =1)	482	19
244035.70	20 _{16,4} – 19 _{16,3} (A, v _t =1)	482	19
244048.44	20 _{15,5} – 19 _{15,4} (A, v _t =1)	461	23
244048.44	20 _{15,6} – 19 _{15,5} (A, v _t =1)	461	23
244066.67	19 _{4,15} – 18 _{4,14} (A, v _t =1)	313	48
244073.58	20 _{14,6} – 19 _{14,5} (A, v _t =1)	441	27
244073.58	20 _{14,7} – 19 _{14,6} (A, v _t =1)	441	27
244112.42	20 _{10,10} – 19 _{10,9} (E, v _t =1)	378	40
244119.66	20 _{13,7} – 19 _{13,6} (A, v _t =1)	423	31
244119.66	20 _{13,8} – 19 _{13,7} (A, v _t =1)	423	31
244198.30	20 _{12,9} – 19 _{12,8} (A, v _t =1)	407	34
244198.30	20 _{12,8} – 19 _{12,7} (A, v _t =1)	407	34
244207.14	20 _{13,8} – 19 _{13,7} (E, v _t =1)	423	31
244326.23	20 _{11,9} – 19 _{11,8} (A, v _t =1)	391	37
244326.23	20 _{11,10} – 19 _{11,9} (A, v _t =1)	391	37
244445.53	20 _{12,9} – 19 _{12,8} (E, v _t =1)	407	34
244528.54	20 _{10,10} – 19 _{10,9} (A, v _t =1)	377	40
244528.54	20 _{10,11} – 19 _{10,10} (A, v _t =1)	377	40

TABLE B1—*Continued*

Frequency (MHz)	Transition	E_{up} (K)	$S\mu^2$ (D ²)
244580.34 *	20 _{4,17} – 19 _{4,16} (E, v _t =0)	135	51
244588.04	20 _{9,11} – 19 _{9,10} (E, v _t =1)	365	42
244594.05 *	20 _{4,17} – 19 _{4,16} (A, v _t =0)	135	51
244729.66	20 _{11,10} – 19 _{11,9} (E, v _t =1)	391	37
244845.34	20 _{9,11} – 19 _{9,10} (A, v _t =1)	365	42
244845.34	20 _{9,12} – 19 _{9,11} (A, v _t =1)	365	42
244902.13 *	19 _{4,15} – 18 _{4,14} (E, v _t =1)	312	49
245261.74	20 _{8,12} – 19 _{8,11} (E, v _t =1)	354	45
245342.55	20 _{8,13} – 19 _{8,12} (A, v _t =1)	354	45
245350.23	20 _{8,12} – 19 _{8,11} (A, v _t =1)	354	45
245437.31	21 _{3,19} – 20 _{3,18} (A, v _t =1)	327	54
245475.96	20 _{18,2} – 19 _{18,1} (A, v _t =0)	339	10
245475.96	20 _{18,3} – 19 _{18,2} (A, v _t =0)	339	10
245491.82	20 _{18,2} – 19 _{18,1} (E, v _t =0)	339	10
245498.36	20 _{18,3} – 19 _{18,2} (E, v _t =0)	339	10
245517.55	20 _{17,4} – 19 _{17,3} (A, v _t =0)	315	15
245517.55	20 _{17,3} – 19 _{17,2} (A, v _t =0)	315	15
245530.30	20 _{17,3} – 19 _{17,2} (E, v _t =0)	315	15
245540.34	20 _{17,4} – 19 _{17,3} (E, v _t =0)	315	15
245543.88	20 _{9,12} – 19 _{9,11} (E, v _t =1)	364	43
245574.71 *	20 _{16,4} – 19 _{16,3} (A, v _t =0)	294	19
245574.71 *	20 _{16,5} – 19 _{16,4} (A, v _t =0)	294	19
245583.97	20 _{16,4} – 19 _{16,3} (E, v _t =0)	294	19
245597.30	20 _{16,5} – 19 _{16,4} (E, v _t =0)	294	19
245651.21 *	20 _{15,6} – 19 _{15,5} (A, v _t =0)	273	23
245651.21 *	20 _{15,5} – 19 _{15,4} (A, v _t =0)	273	23
245656.78	20 _{15,5} – 19 _{15,4} (E, v _t =0)	273	23
245672.98	20 _{15,6} – 19 _{15,5} (E, v _t =0)	273	23
245752.27 *	20 _{14,6} – 19 _{14,5} (A, v _t =0)	254	27
245752.27 *	20 _{14,7} – 19 _{14,6} (A, v _t =0)	254	27
245754.10 *	20 _{14,6} – 19 _{14,5} (E, v _t =0)	254	27
245772.69 *	20 _{14,7} – 19 _{14,6} (E, v _t =0)	254	27
245846.91	21 _{3,19} – 20 _{3,18} (E, v _t =1)	326	54
245883.18 *	20 _{13,7} – 19 _{13,6} (E, v _t =0)	236	31
245885.24 *	20 _{13,7} – 19 _{13,6} (A, v _t =0)	236	31
245885.24 *	20 _{13,8} – 19 _{13,7} (A, v _t =0)	236	31
245903.68 *	20 _{13,8} – 19 _{13,7} (E, v _t =0)	236	31
246054.82 *	20 _{12,8} – 19 _{12,7} (E, v _t =0)	219	34
246060.83 *	20 _{12,8} – 19 _{12,7} (A, v _t =0)	219	34
246060.83 *	20 _{12,9} – 19 _{12,8} (A, v _t =0)	219	34
246076.86 *	20 _{12,9} – 19 _{12,8} (E, v _t =0)	219	34
246106.85	20 _{7,14} – 19 _{7,13} (A, v _t =1)	344	47
246184.18	20 _{8,13} – 19 _{8,12} (E, v _t =1)	353	45
246187.02	21 _{2,19} – 20 _{2,18} (A, v _t =1)	327	54
246233.58	20 _{7,13} – 19 _{7,12} (A, v _t =1)	344	47
246274.89	20 _{7,13} – 19 _{7,12} (E, v _t =1)	344	47
246285.40 *	20 _{11,9} – 19 _{11,8} (E, v _t =0)	204	37
246295.14 *	20 _{11,10} – 19 _{11,9} (A, v _t =0)	204	37
246295.14 *	20 _{11,9} – 19 _{11,8} (A, v _t =0)	204	37

TABLE B1—Continued

Frequency (MHz)	Transition	E_{up} (K)	$S\mu^2$ (D ²)
$\text{H}^{13}\text{COOCH}_3$			
246308.27 *	20 _{11,10} – 19 _{11,9} (E, $v_t=0$)	204	37
246461.17	22 _{2,21} – 21 _{2,20} (A, $v_t=1$)	330	57
246488.43	22 _{1,21} – 21 _{1,20} (A, $v_t=1$)	330	57
246562.88	21 _{2,19} – 20 _{2,18} (E, $v_t=1$)	326	54
246600.01 *	20 _{10,10} – 19 _{10,9} (E, $v_t=0$)	190	40
246613.39 *	20 _{10,10} – 19 _{10,9} (A, $v_t=0$)	190	40
246613.39 *	20 _{10,11} – 19 _{10,10} (A, $v_t=0$)	190	40
246615.13 *	20 _{5,16} – 19 _{5,15} (A, $v_t=1$)	328	50
246623.19 *	20 _{10,11} – 19 _{10,10} (E, $v_t=0$)	190	40
$\text{H}^{13}\text{COOCH}_3$			
213882.01	18 _{2,16} – 17 _{2,15} (A, $v_t=1$)	293	47
214142.41	20 _{1,20} – 19 _{1,19} (A, $v_t=1$)	299	54
214144.27	20 _{0,20} – 19 _{0,19} (A, $v_t=1$)	299	54
214195.70	20 _{1,20} – 19 _{1,19} (E, $v_t=1$)	299	54
214197.43	20 _{0,20} – 19 _{0,19} (E, $v_t=1$)	299	54
214277.81	18 _{2,16} – 17 _{2,15} (E, $v_t=1$)	293	47
214414.15	19 _{2,18} – 18 _{2,17} (E, $v_t=0$)	108	50
214419.83	19 _{2,18} – 18 _{2,17} (A, $v_t=0$)	108	50
214511.90	19 _{1,18} – 18 _{1,17} (E, $v_t=0$)	108	50
214517.43	19 _{1,18} – 18 _{1,17} (A, $v_t=0$)	108	50
214705.26	17 _{3,14} – 16 _{3,13} (A, $v_t=1$)	287	44
215115.64	18 _{2,16} – 17 _{2,15} (E, $v_t=0$)	105	47
215124.26	18 _{2,16} – 17 _{2,15} (A, $v_t=0$)	105	47
215253.79	20 _{1,20} – 19 _{1,19} (E, $v_t=0$)	111	54
215254.90	20 _{1,20} – 19 _{1,19} (A, $v_t=0$)	111	54
215255.19	20 _{0,20} – 19 _{0,19} (E, $v_t=0$)	111	54
215256.30	20 _{0,20} – 19 _{0,19} (A, $v_t=0$)	111	54
215322.04	17 _{3,14} – 16 _{3,13} (E, $v_t=1$)	287	45
215792.63	17 _{4,13} – 16 _{4,12} (A, $v_t=1$)	291	44
216560.30	17 _{4,13} – 16 _{4,12} (E, $v_t=1$)	290	44
216621.17	17 _{3,14} – 16 _{3,13} (E, $v_t=0$)	99	44
216637.79	17 _{3,14} – 16 _{3,13} (A, $v_t=0$)	99	44
218060.27	18 _{4,15} – 17 _{4,14} (A, $v_t=1$)	299	46
218601.70	17 _{4,13} – 16 _{4,12} (E, $v_t=0$)	102	44
218624.43	17 _{4,13} – 16 _{4,12} (A, $v_t=0$)	102	44
218750.28	18 _{4,15} – 17 _{4,14} (E, $v_t=1$)	299	46
219305.48	18 _{7,12} – 17 _{7,11} (A, $v_t=1$)	321	41
219336.91	18 _{15,3} – 17 _{15,3} (A, $v_t=0$)	248	15
219336.91	18 _{15,4} – 17 _{15,2} (A, $v_t=0$)	248	15
219338.83	18 _{7,11} – 17 _{7,10} (A, $v_t=1$)	321	41
219342.46	18 _{15,3} – 17 _{15,2} (E, $v_t=0$)	248	15
219356.73	18 _{15,4} – 17 _{15,3} (E, $v_t=0$)	248	15
219374.77	18 _{7,11} – 17 _{7,10} (E, $v_t=1$)	321	42
219407.14	18 _{14,5} – 17 _{14,3} (A, $v_t=0$)	229	19
219407.14	18 _{14,4} – 17 _{14,4} (A, $v_t=0$)	229	19
219409.28	18 _{14,4} – 17 _{14,3} (E, $v_t=0$)	229	19
219425.77	18 _{14,5} – 17 _{14,4} (E, $v_t=0$)	229	19
219481.75	18 _{8,11} – 17 _{8,10} (E, $v_t=1$)	330	39
219499.54	18 _{13,5} – 17 _{13,4} (E, $v_t=0$)	211	23

TABLE B1—Continued

Frequency (MHz)	Transition	E_{up} (K)	$S\mu^2$ (D ²)
219500.88	18 _{13,6} – 17 _{13,4} (A, v _t =0)	211	23
219500.88	18 _{13,5} – 17 _{13,5} (A, v _t =0)	211	23
219517.84	18 _{13,6} – 17 _{13,5} (E, v _t =0)	211	23
219621.06	18 _{12,6} – 17 _{12,5} (E, v _t =0)	195	27
219625.86	18 _{12,6} – 17 _{12,5} (A, v _t =0)	195	25
219625.86	18 _{12,7} – 17 _{12,6} (A, v _t =0)	195	25
219640.69	18 _{12,7} – 17 _{12,6} (E, v _t =0)	195	27
219785.45	18 _{11,7} – 17 _{11,6} (E, v _t =0)	180	31
219793.64	18 _{11,7} – 17 _{11,6} (A, v _t =0)	180	31
219793.64	18 _{11,8} – 17 _{11,7} (A, v _t =0)	180	31
219805.93	18 _{11,8} – 17 _{11,7} (E, v _t =0)	180	31
219984.12	18 _{4,15} – 17 _{4,14} (E, v _t =0)	111	46
219997.96	18 _{4,15} – 17 _{4,14} (A, v _t =0)	111	46
220010.78	18 _{10,8} – 17 _{10,7} (E, v _t =0)	166	34
220022.21	18 _{10,8} – 17 _{10,7} (A, v _t =0)	166	34
220022.21	18 _{10,9} – 17 _{10,8} (A, v _t =0)	166	34
220031.61	18 _{10,9} – 17 _{10,8} (E, v _t =0)	166	34
220084.21	18 _{6,13} – 17 _{6,12} (A, v _t =1)	313	43
220166.69	18 _{7,12} – 17 _{7,11} (E, v _t =1)	321	42
220326.52	18 _{9,9} – 17 _{9,8} (E, v _t =0)	153	37
220341.01	18 _{9,10} – 17 _{9,9} (A, v _t =0)	153	37
220341.08	18 _{9,9} – 17 _{9,8} (A, v _t =0)	153	37
220347.23	18 _{9,10} – 17 _{9,9} (E, v _t =0)	153	37
220404.83	18 _{5,14} – 17 _{5,13} (A, v _t =1)	306	45
220551.30	18 _{6,12} – 17 _{6,11} (A, v _t =1)	313	43
220567.31	18 _{6,12} – 17 _{6,11} (E, v _t =1)	313	44
220784.32	18 _{8,10} – 17 _{8,9} (E, v _t =0)	142	39
220800.67	18 _{8,11} – 17 _{8,10} (A, v _t =0)	142	39
220802.86	18 _{8,10} – 17 _{8,9} (A, v _t =0)	142	39
220804.46	18 _{8,11} – 17 _{8,10} (E, v _t =0)	142	39
221274.41	18 _{6,13} – 17 _{6,12} (E, v _t =1)	312	43
221482.38	18 _{7,12} – 17 _{7,11} (A, v _t =0)	133	42
221489.49	18 _{7,11} – 17 _{7,10} (E, v _t =0)	133	41
221498.59	18 _{7,12} – 17 _{7,11} (E, v _t =0)	133	41
221527.04	18 _{7,11} – 17 _{7,10} (A, v _t =0)	133	42
221898.13	18 _{5,14} – 17 _{5,13} (E, v _t =1)	305	44
222327.33	19 _{3,17} – 18 _{3,16} (A, v _t =1)	304	50
222382.86	18 _{6,13} – 17 _{6,12} (E, v _t =0)	124	43
222384.79	18 _{6,13} – 17 _{6,12} (A, v _t =0)	124	43
222658.46	18 _{5,14} – 17 _{5,13} (E, v _t =0)	117	45
222673.23	18 _{5,14} – 17 _{5,13} (A, v _t =0)	117	45
222753.71	19 _{3,17} – 18 _{3,16} (E, v _t =1)	304	50
222955.47	18 _{6,12} – 17 _{6,11} (E, v _t =0)	124	43
222982.05	18 _{6,12} – 17 _{6,11} (A, v _t =0)	124	43
223612.37	20 _{2,19} – 19 _{2,18} (A, v _t =1)	308	53
223685.92	20 _{1,19} – 19 _{1,18} (A, v _t =1)	308	53
223855.00	19 _{3,17} – 18 _{3,16} (E, v _t =0)	116	50
223860.35	20 _{2,19} – 19 _{2,18} (E, v _t =1)	307	53
223864.72	19 _{3,17} – 18 _{3,16} (A, v _t =0)	116	50

TABLE B1—Continued

Frequency (MHz)	Transition	E_{up} (K)	$S\mu^2$ (D ²)
223928.05	19 _{2,17} – 18 _{2,16} (A, v _t =1)	304	50
223929.86	20 _{1,19} – 19 _{1,18} (E, v _t =1)	307	53
224076.48	18 _{5,13} – 17 _{5,12} (A, v _t =1)	306	45
224161.64	18 _{5,13} – 17 _{5,12} (E, v _t =1)	306	44
224311.33	19 _{2,17} – 18 _{2,16} (E, v _t =1)	304	50
224604.66	21 _{1,21} – 20 _{1,20} (A, v _t =1)	310	56
224605.70	21 _{0,21} – 20 _{0,20} (A, v _t =1)	310	56
224655.45	21 _{1,21} – 20 _{1,20} (E, v _t =1)	309	57
224656.40	21 _{0,21} – 20 _{0,20} (E, v _t =1)	309	57
224933.48	20 _{2,19} – 19 _{2,18} (E, v _t =0)	119	53
224939.06	20 _{2,19} – 19 _{2,18} (A, v _t =0)	119	53
224991.47	20 _{1,19} – 19 _{1,18} (E, v _t =0)	119	53
224996.96	20 _{1,19} – 19 _{1,18} (A, v _t =0)	119	53
225227.63	19 _{2,17} – 18 _{2,16} (E, v _t =0)	116	50
225236.12	19 _{2,17} – 18 _{2,16} (A, v _t =0)	116	50
225766.36	21 _{1,21} – 20 _{1,20} (E, v _t =0)	121	57
225767.12	21 _{0,21} – 20 _{0,20} (E, v _t =0)	121	57
225767.40	21 _{1,21} – 20 _{1,20} (A, v _t =0)	121	57
225768.16	21 _{0,21} – 20 _{0,20} (A, v _t =0)	121	57
225864.59	18 _{3,15} – 17 _{3,14} (A, v _t =1)	298	47
226464.48	18 _{3,15} – 17 _{3,14} (E, v _t =1)	298	47
227022.02	18 _{5,13} – 17 _{5,12} (E, v _t =0)	118	45
227043.97	18 _{5,13} – 17 _{5,12} (A, v _t =0)	118	45
227634.21	18 _{3,15} – 17 _{3,14} (E, v _t =0)	110	47
227649.24	18 _{3,15} – 17 _{3,14} (A, v _t =0)	110	47
229246.35	18 _{4,14} – 17 _{4,13} (A, v _t =1)	302	47
229503.97	19 _{4,16} – 18 _{4,15} (A, v _t =1)	310	49
230063.58	18 _{4,14} – 17 _{4,13} (E, v _t =1)	301	47
230141.83	19 _{4,16} – 18 _{4,15} (E, v _t =1)	310	49
231439.43	19 _{4,16} – 18 _{4,15} (E, v _t =0)	122	49
231453.13	19 _{4,16} – 18 _{4,15} (A, v _t =0)	122	49
231467.47	19 _{17,2} – 18 _{17,2} (A, v _t =0)	301	10
231467.47	19 _{17,3} – 18 _{17,1} (A, v _t =0)	301	10
231479.64	19 _{17,2} – 18 _{17,1} (E, v _t =0)	301	10
231488.89	19 _{17,3} – 18 _{17,2} (E, v _t =0)	301	10
231514.55	19 _{16,3} – 18 _{16,3} (A, v _t =0)	279	15
231514.55	19 _{16,4} – 18 _{16,2} (A, v _t =0)	279	15
231523.51	19 _{16,3} – 18 _{16,2} (E, v _t =0)	279	15
231535.82	19 _{16,4} – 18 _{16,3} (E, v _t =0)	279	15
231578.36	19 _{15,5} – 18 _{15,3} (A, v _t =0)	259	19
231578.36	19 _{15,4} – 18 _{15,4} (A, v _t =0)	259	19
231583.89	19 _{15,4} – 18 _{15,3} (E, v _t =0)	259	19
231598.91	19 _{15,5} – 18 _{15,4} (E, v _t =0)	259	19
231663.36	19 _{14,5} – 18 _{14,4} (A, v _t =0)	240	24
231663.36	19 _{14,6} – 18 _{14,5} (A, v _t =0)	240	24
231665.32	19 _{14,5} – 18 _{14,4} (E, v _t =0)	240	24
231682.65	19 _{14,6} – 18 _{14,5} (E, v _t =0)	240	24
231774.17	19 _{13,6} – 18 _{13,5} (E, v _t =0)	222	27
231775.84	19 _{13,6} – 18 _{13,6} (A, v _t =0)	222	27

TABLE B1—Continued

Frequency (MHz)	Transition	E_{up} (K)	$S\mu^2$ (D ²)
231775.84	19 _{13,7} – 18 _{13,5} (A, $v_t=0$)	222	27
231793.36	19 _{13,7} – 18 _{13,6} (E, $v_t=0$)	222	27
231919.66	19 _{12,7} – 18 _{12,6} (E, $v_t=0$)	206	31
231924.95	19 _{12,8} – 18 _{12,7} (A, $v_t=0$)	206	31
231924.95	19 _{12,7} – 18 _{12,6} (A, $v_t=0$)	206	31
231940.22	19 _{12,8} – 18 _{12,7} (E, $v_t=0$)	206	31
232073.37	18 _{4,14} – 17 _{4,13} (E, $v_t=0$)	113	47
232096.29	18 _{4,14} – 17 _{4,13} (A, $v_t=0$)	113	47
232115.55	19 _{11,8} – 18 _{11,7} (E, $v_t=0$)	191	34
232124.38	19 _{11,8} – 18 _{11,7} (A, $v_t=0$)	191	34
232124.38	19 _{11,9} – 18 _{11,8} (A, $v_t=0$)	191	34
232136.97	19 _{11,9} – 18 _{11,8} (E, $v_t=0$)	191	34
232383.30	19 _{10,9} – 18 _{10,8} (E, $v_t=0$)	177	37
232395.54	19 _{10,10} – 18 _{10,9} (A, $v_t=0$)	177	37
232395.55	19 _{10,9} – 18 _{10,8} (A, $v_t=0$)	177	37
232405.07	19 _{10,10} – 18 _{10,9} (E, $v_t=0$)	177	37
232637.36	19 _{6,14} – 18 _{6,13} (A, $v_t=1$)	324	46
232664.08	19 _{5,15} – 18 _{5,14} (A, $v_t=1$)	317	48
232758.18	19 _{9,10} – 18 _{9,9} (E, $v_t=0$)	165	40
232773.58	19 _{9,11} – 18 _{9,10} (A, $v_t=0$)	165	40
232773.77	19 _{9,10} – 18 _{9,9} (A, $v_t=0$)	165	40
232779.80	19 _{9,11} – 18 _{9,10} (E, $v_t=0$)	165	40
232961.84	20 _{3,18} – 19 _{3,17} (A, $v_t=1$)	315	52
233302.69	19 _{8,11} – 18 _{8,10} (E, $v_t=0$)	153	42
233318.71	19 _{8,12} – 18 _{8,11} (A, $v_t=0$)	153	42
233323.61	19 _{8,12} – 18 _{8,11} (E, $v_t=0$)	153	42
233323.76	19 _{8,11} – 18 _{8,10} (A, $v_t=0$)	153	42
233375.70	20 _{3,18} – 19 _{3,17} (E, $v_t=1$)	315	53
233388.18	19 _{6,13} – 18 _{6,12} (E, $v_t=1$)	324	46
233455.09	19 _{6,13} – 18 _{6,12} (A, $v_t=1$)	324	46
233901.15	19 _{5,15} – 18 _{5,14} (E, $v_t=1$)	316	47
234018.31	19 _{6,14} – 18 _{6,13} (E, $v_t=1$)	323	46
234053.35	20 _{2,18} – 19 _{2,17} (A, $v_t=1$)	315	52
234076.35	21 _{2,20} – 20 _{2,19} (A, $v_t=1$)	319	56
234117.33	19 _{7,13} – 18 _{7,12} (A, $v_t=0$)	144	45
234120.40	21 _{1,20} – 20 _{1,19} (A, $v_t=1$)	319	56
234139.26	19 _{7,13} – 18 _{7,12} (E, $v_t=0$)	144	43
234162.36	19 _{7,12} – 18 _{7,11} (E, $v_t=0$)	144	43
234207.54	19 _{7,12} – 18 _{7,11} (A, $v_t=0$)	144	45
234320.61	21 _{2,20} – 20 _{2,19} (E, $v_t=1$)	318	56
234361.88	21 _{1,20} – 20 _{1,19} (E, $v_t=1$)	318	56
234429.33	20 _{2,18} – 19 _{2,17} (E, $v_t=1$)	315	53
234514.45	20 _{3,18} – 19 _{3,17} (E, $v_t=0$)	127	52
234523.90	20 _{3,18} – 19 _{3,17} (A, $v_t=0$)	127	52
234991.22	19 _{5,15} – 18 _{5,14} (E, $v_t=0$)	129	48
235006.81	19 _{5,15} – 18 _{5,14} (A, $v_t=0$)	129	48
235064.98	22 _{0,22} – 21 _{1,21} (A, $v_t=1$)	321	10
235065.69	22 _{1,22} – 21 _{1,21} (A, $v_t=1$)	321	59
235066.27	22 _{0,22} – 21 _{0,21} (A, $v_t=1$)	321	59

TABLE B1—Continued

Frequency (MHz)	Transition	E_{up} (K)	$S\mu^2$ (D ²)
235066.98	22 _{1,22} – 21 _{0,21} (A, v _t =1)	321	10
235069.01	19 _{6,14} – 18 _{6,13} (E, v _t =0)	136	46
235078.39	19 _{6,14} – 18 _{6,13} (A, v _t =0)	136	46
235113.39	22 _{0,22} – 21 _{1,21} (E, v _t =1)	321	10
235114.01	22 _{1,22} – 21 _{1,21} (E, v _t =1)	321	59
235114.54	22 _{0,22} – 21 _{0,21} (E, v _t =1)	321	59
235115.17	22 _{1,22} – 21 _{0,21} (E, v _t =1)	321	10
235428.18	20 _{2,18} – 19 _{2,17} (E, v _t =0)	127	52
235436.62	20 _{2,18} – 19 _{2,17} (A, v _t =0)	127	52
235446.18	21 _{2,20} – 20 _{2,19} (E, v _t =0)	131	56
235451.69	21 _{2,20} – 20 _{2,19} (A, v _t =0)	131	56
235480.23	21 _{1,20} – 20 _{1,19} (E, v _t =0)	131	56
235485.67	21 _{1,20} – 20 _{1,19} (A, v _t =0)	131	56
236096.20	19 _{6,13} – 18 _{6,12} (E, v _t =0)	136	46
236117.98	19 _{6,13} – 18 _{6,12} (A, v _t =0)	136	46
236277.24	22 _{0,22} – 21 _{1,21} (E, v _t =0)	133	10
236277.73	22 _{1,22} – 21 _{1,21} (E, v _t =0)	133	59
236278.15	22 _{0,22} – 21 _{0,21} (E, v _t =0)	133	59
236278.23	22 _{0,22} – 21 _{1,21} (A, v _t =0)	133	10
236278.64	22 _{1,22} – 21 _{0,21} (E, v _t =0)	133	10
236278.71	22 _{1,22} – 21 _{1,21} (A, v _t =0)	133	59
236279.13	22 _{0,22} – 21 _{0,21} (A, v _t =0)	133	59
236279.62	22 _{1,22} – 21 _{0,21} (A, v _t =0)	133	10
236524.71	19 _{3,16} – 18 _{3,15} (A, v _t =1)	309	50
237093.81	19 _{3,16} – 18 _{3,15} (E, v _t =1)	309	50
237953.24	19 _{5,14} – 18 _{5,13} (A, v _t =1)	317	48
238144.27	19 _{3,16} – 18 _{3,15} (E, v _t =0)	121	50
238157.56	19 _{3,16} – 18 _{3,15} (A, v _t =0)	121	50
238406.69	19 _{5,14} – 18 _{5,13} (E, v _t =1)	317	48
240772.60	20 _{4,17} – 19 _{4,16} (A, v _t =1)	322	52
241174.56	19 _{5,14} – 18 _{5,13} (E, v _t =0)	129	48
241198.37	19 _{5,14} – 18 _{5,13} (A, v _t =0)	129	48
241374.05	20 _{4,17} – 19 _{4,16} (E, v _t =1)	322	52
242316.68	19 _{4,15} – 18 _{4,14} (A, v _t =1)	313	49
242710.87	20 _{4,17} – 19 _{4,16} (E, v _t =0)	134	52
242724.28	20 _{4,17} – 19 _{4,16} (A, v _t =0)	134	52
243126.27	19 _{4,15} – 18 _{4,14} (E, v _t =1)	313	50
243533.71	21 _{3,19} – 20 _{3,18} (A, v _t =1)	327	55
243694.15	20 _{17,3} – 19 _{17,2} (A, v _t =0)	313	15
243694.15	20 _{17,4} – 19 _{17,3} (A, v _t =0)	313	15
243706.54	20 _{17,3} – 19 _{17,2} (E, v _t =0)	313	15
243716.34	20 _{17,4} – 19 _{17,3} (E, v _t =0)	313	15
243751.84	20 _{16,4} – 19 _{16,4} (A, v _t =0)	291	20
243751.84	20 _{16,5} – 19 _{16,3} (A, v _t =0)	291	20
243760.88	20 _{16,4} – 19 _{16,3} (E, v _t =0)	291	20
243773.84	20 _{16,5} – 19 _{16,4} (E, v _t =0)	291	20
243828.84	20 _{15,6} – 19 _{15,5} (A, v _t =0)	271	24
243828.84	20 _{15,5} – 19 _{15,4} (A, v _t =0)	271	24
243834.32	20 _{15,5} – 19 _{15,4} (E, v _t =0)	271	24

TABLE B1—Continued

Frequency (MHz)	Transition	E_{up} (K)	$S\mu^2$ (D ²)
243850.07	20 _{15,6} – 19 _{15,5} (E, v _t =0)	271	24
243930.38	20 _{14,6} – 19 _{14,5} (A, v _t =0)	252	28
243930.38	20 _{14,7} – 19 _{14,6} (A, v _t =0)	252	28
243932.14	20 _{14,6} – 19 _{14,5} (E, v _t =0)	252	28
243936.25	21 _{3,19} – 20 _{3,18} (E, v _t =1)	327	55
243950.27	20 _{14,7} – 19 _{14,6} (E, v _t =0)	252	28
244061.81	20 _{13,7} – 19 _{13,6} (E, v _t =0)	234	31
244063.84	20 _{13,7} – 19 _{13,6} (A, v _t =0)	234	14
244063.84	20 _{13,7} – 19 _{13,7} (A, v _t =0)	234	18
244063.84	20 _{13,8} – 19 _{13,7} (A, v _t =0)	234	14
244063.84	20 _{13,8} – 19 _{13,6} (A, v _t =0)	234	18
244081.86	20 _{13,8} – 19 _{13,7} (E, v _t =0)	234	31
244234.13	20 _{12,8} – 19 _{12,7} (E, v _t =0)	217	35
244239.94	20 _{12,8} – 19 _{12,7} (A, v _t =0)	217	35
244239.94	20 _{12,9} – 19 _{12,8} (A, v _t =0)	217	35
244255.58	20 _{12,9} – 19 _{12,8} (E, v _t =0)	217	35
244258.67	21 _{2,19} – 20 _{2,18} (A, v _t =1)	327	55
244465.29	20 _{11,9} – 19 _{11,8} (E, v _t =0)	202	38
244474.79	20 _{11,10} – 19 _{11,9} (A, v _t =0)	202	38
244474.80	20 _{11,9} – 19 _{11,8} (A, v _t =0)	202	38
244487.62	20 _{11,10} – 19 _{11,9} (E, v _t =0)	202	38
244630.26	21 _{2,19} – 20 _{2,18} (E, v _t =1)	327	55
244776.10	22 _{2,21} – 21 _{2,20} (E, v _t =1)	330	59
244780.64	20 _{10,10} – 19 _{10,9} (E, v _t =0)	189	41
244793.70	20 _{10,11} – 19 _{10,10} (A, v _t =0)	189	41
244793.71	20 _{10,10} – 19 _{10,9} (A, v _t =0)	189	41
244800.36	22 _{1,21} – 21 _{1,20} (E, v _t =1)	330	59
244800.37	20 _{5,16} – 19 _{5,15} (A, v _t =1)	329	51
244803.30	20 _{10,11} – 19 _{10,10} (E, v _t =0)	189	41
245091.87	19 _{4,15} – 18 _{4,14} (E, v _t =0)	125	50
245114.32	19 _{4,15} – 18 _{4,14} (A, v _t =0)	125	50
245116.09	21 _{3,19} – 20 _{3,18} (E, v _t =0)	139	55
245125.31	21 _{3,19} – 20 _{3,18} (A, v _t =0)	139	55
245222.14	20 _{9,11} – 19 _{9,10} (E, v _t =0)	176	43
245238.38	20 _{9,12} – 19 _{9,11} (A, v _t =0)	176	43
245238.88	20 _{9,11} – 19 _{9,10} (A, v _t =0)	176	43
245244.63	20 _{9,12} – 19 _{9,11} (E, v _t =0)	176	43
245709.27	21 _{2,19} – 20 _{2,18} (E, v _t =0)	139	55
245717.70	21 _{2,19} – 20 _{2,18} (A, v _t =0)	139	55
245807.84	20 _{5,16} – 19 _{5,15} (E, v _t =1)	328	51
245865.47	20 _{8,12} – 19 _{8,11} (E, v _t =0)	165	46
245879.34	20 _{8,13} – 19 _{8,12} (A, v _t =0)	165	46
245886.65	20 _{8,13} – 19 _{8,12} (E, v _t =0)	165	46
245890.46	20 _{8,12} – 19 _{8,11} (A, v _t =0)	165	46
245954.67	22 _{2,21} – 21 _{2,20} (E, v _t =0)	142	59
245960.11	22 _{2,21} – 21 _{2,20} (A, v _t =0)	142	59
245974.47	22 _{1,21} – 21 _{1,20} (E, v _t =0)	142	58
245979.86	22 _{1,21} – 21 _{1,20} (A, v _t =0)	142	58

TABLE B1—*Continued*

Frequency (MHz)	Transition	E_{up} (K)	$S\mu^2$ (D ²)
HCOO ¹³ CH ₃			
215660.48	18 _{17,1} – 17 17, ₀ (A, v _t =0)	289	10
215693.64	18 _{16,2} – 17 16, ₁ (A, v _t =0)	267	20
215702.37	18 _{16,2} – 17 16, ₁ (E, v _t =0)	267	10
215713.19	18 _{16,3} – 17 16, ₂ (E, v _t =0)	267	10
215740.43	18 _{15,3} – 17 15, ₂ (A, v _t =0)	247	29
215746.04	18 _{15,3} – 17 15, ₂ (E, v _t =0)	247	15
215759.41	18 _{15,4} – 17 15, ₃ (E, v _t =0)	247	15
215804.38	18 _{14,4} – 17 14, ₃ (A, v _t =0)	228	38
215806.74	18 _{14,4} – 17 14, ₃ (E, v _t =0)	228	19
215822.28	18 _{14,5} – 17 14, ₄ (E, v _t =0)	228	19
215889.52	18 _{13,5} – 17 13, ₄ (E, v _t =0)	210	23
215890.48	18 _{13,5} – 17 13, ₄ (A, v _t =0)	210	46
215906.83	18 _{13,6} – 17 13, ₅ (E, v _t =0)	210	23
216001.68	18 _{12,6} – 17 12, ₅ (E, v _t =0)	193	27
216005.97	18 _{12,6} – 17 12, ₅ (A, v _t =0)	193	53
216020.32	18 _{12,7} – 17 12, ₆ (E, v _t =0)	193	27
216154.11	18 _{11,7} – 17 11, ₆ (E, v _t =0)	178	30
216161.65	18 _{11,7} – 17 11, ₆ (A, v _t =0)	178	60
216173.61	18 _{11,8} – 17 11, ₇ (E, v _t =0)	178	30
216363.67	18 _{10,8} – 17 10, ₇ (E, v _t =0)	164	33
216374.34	18 _{10,8} – 17 10, ₇ (A, v _t =0)	164	66
216383.56	18 _{10,9} – 17 10, ₈ (E, v _t =0)	164	33
216566.07	18 _{4,15} – 17 4, ₁₄ (E, v _t =0)	110	45
216579.52	18 _{4,15} – 17 4, ₁₄ (A, v _t =0)	110	45
216657.87	18 _{9,9} – 17 9, ₈ (E, v _t =0)	152	36
216671.50	18 _{9,10} – 17 9, ₉ (A, v _t =0)	152	36
216671.55	18 _{9,9} – 17 9, ₈ (A, v _t =0)	152	36
216677.69	18 _{9,10} – 17 9, ₉ (E, v _t =0)	152	36
217084.75	18 _{8,10} – 17 8, ₉ (E, v _t =0)	141	38
217100.39	18 _{8,11} – 17 8, ₁₀ (A, v _t =0)	141	38
217102.05	18 _{8,10} – 17 8, ₉ (A, v _t =0)	141	38
217104.07	18 _{8,11} – 17 8, ₁₀ (E, v _t =0)	141	38
217738.48	18 _{7,12} – 17 7, ₁₁ (A, v _t =0)	131	41
217740.08	18 _{7,11} – 17 7, ₁₀ (E, v _t =0)	131	40
217752.37	18 _{7,12} – 17 7, ₁₁ (E, v _t =0)	131	40
217773.89	18 _{7,11} – 17 7, ₁₀ (A, v _t =0)	131	41
218602.65	18 _{6,13} – 17 6, ₁₂ (A, v _t =0)	123	42
218604.51	18 _{6,13} – 17 6, ₁₂ (E, v _t =0)	123	42
218953.96	18 _{5,14} – 17 5, ₁₃ (E, v _t =0)	116	44
218967.86	18 _{5,14} – 17 5, ₁₃ (A, v _t =0)	116	44
219068.15	18 _{6,12} – 17 6, ₁₁ (E, v _t =0)	123	42
219096.72	18 _{6,12} – 17 6, ₁₁ (A, v _t =0)	123	42
220638.01	19 _{3,17} – 18 3, ₁₆ (E, v _t =0)	114	49
220647.57	19 _{3,17} – 18 3, ₁₆ (A, v _t =0)	114	49
221756.83	20 _{2,19} – 19 2, ₁₈ (E, v _t =0)	118	52
221762.29	20 _{2,19} – 19 2, ₁₈ (A, v _t =0)	118	52
221825.54	20 _{1,19} – 19 1, ₁₈ (E, v _t =0)	118	52
221830.89	20 _{1,19} – 19 1, ₁₈ (A, v _t =0)	118	52

TABLE B1—Continued

Frequency (MHz)	Transition	E_{up} (K)	$S\mu^2$ (D ²)
222175.71	19 _{2,17} – 18 _{2,16} (E, v _t =0)	114	49
222184.09	19 _{2,17} – 18 _{2,16} (A, v _t =0)	114	49
222574.02	21 _{1,21} – 20 _{1,20} (E, v _t =0)	120	55
222574.96	21 _{0,21} – 20 _{0,20} (E, v _t =0)	120	55
222574.97	21 _{1,21} – 20 _{1,20} (A, v _t =0)	120	55
222575.92	21 _{0,21} – 20 _{0,20} (A, v _t =0)	120	55
222781.26	18 _{5,13} – 17 _{5,12} (E, v _t =0)	116	44
222801.91	18 _{5,13} – 17 _{5,12} (A, v _t =0)	116	44
224348.10	18 _{3,15} – 17 _{3,14} (E, v _t =0)	108	46
224363.32	18 _{3,15} – 17 _{3,14} (A, v _t =0)	108	46
227678.06	19 _{17,2} – 18 _{17,1} (A, v _t =0)	300	20
227689.99	19 _{17,2} – 18 _{17,1} (E, v _t =0)	300	10
227698.46	19 _{17,3} – 18 _{17,2} (E, v _t =0)	300	10
227719.93	19 _{16,3} – 18 _{16,2} (A, v _t =0)	278	29
227728.82	19 _{16,3} – 18 _{16,2} (E, v _t =0)	278	15
227740.26	19 _{16,4} – 18 _{16,3} (E, v _t =0)	278	15
227777.62	19 _{15,4} – 18 _{15,3} (A, v _t =0)	258	38
227783.25	19 _{15,4} – 18 _{15,3} (E, v _t =0)	258	19
227797.33	19 _{15,5} – 18 _{15,4} (E, v _t =0)	258	19
227855.30	19 _{14,5} – 18 _{14,4} (A, v _t =0)	239	46
227857.52	19 _{14,5} – 18 _{14,4} (E, v _t =0)	239	23
227873.86	19 _{14,6} – 18 _{14,5} (E, v _t =0)	239	23
227900.91	19 _{4,16} – 18 _{4,15} (E, v _t =0)	120	48
227914.29	19 _{4,16} – 18 _{4,15} (A, v _t =0)	120	48
227957.60	19 _{13,6} – 18 _{13,5} (E, v _t =0)	221	27
227958.86	19 _{13,6} – 18 _{13,5} (A, v _t =0)	221	54
227972.09	18 _{4,14} – 17 _{4,13} (E, v _t =0)	112	46
227975.78	19 _{13,7} – 18 _{13,6} (E, v _t =0)	221	27
227994.32	18 _{4,14} – 17 _{4,13} (A, v _t =0)	112	46
228092.11	19 _{12,7} – 18 _{12,6} (E, v _t =0)	204	30
228096.85	19 _{12,7} – 18 _{12,6} (A, v _t =0)	204	61
228111.65	19 _{12,8} – 18 _{12,7} (E, v _t =0)	204	30
228273.92	19 _{11,8} – 18 _{11,7} (E, v _t =0)	189	34
228282.07	19 _{11,8} – 18 _{11,7} (A, v _t =0)	189	67
228294.35	19 _{11,9} – 18 _{11,8} (E, v _t =0)	189	34
228523.06	19 _{10,9} – 18 _{10,8} (E, v _t =0)	175	36
228534.50	19 _{10,9} – 18 _{10,8} (A, v _t =0)	175	73
228543.88	19 _{10,10} – 18 _{10,9} (E, v _t =0)	175	36
228872.40	19 _{9,10} – 18 _{9,9} (E, v _t =0)	163	39
228886.91	19 _{9,11} – 18 _{9,10} (A, v _t =0)	163	39
228887.06	19 _{9,10} – 18 _{9,9} (A, v _t =0)	163	39
228893.13	19 _{9,11} – 18 _{9,10} (E, v _t =0)	163	39
229379.94	19 _{8,11} – 18 _{8,10} (E, v _t =0)	152	41
229395.55	19 _{8,12} – 18 _{8,11} (A, v _t =0)	152	41
229399.42	19 _{8,11} – 18 _{8,10} (A, v _t =0)	152	41
229400.08	19 _{8,12} – 18 _{8,11} (E, v _t =0)	152	41
230144.56	19 _{7,13} – 18 _{7,12} (A, v _t =0)	142	44
230165.46	19 _{7,13} – 18 _{7,12} (E, v _t =0)	142	43
230173.61	19 _{7,12} – 18 _{7,11} (E, v _t =0)	142	43

TABLE B1—Continued

Frequency (MHz)	Transition	E_{up} (K)	$S\mu^2$ (D ²)
230216.23	19 _{7,12} – 18 _{7,11} (A, v _t =0)	142	44
231070.34	19 _{6,14} – 18 _{6,13} (E, v _t =0)	134	45
231077.35	19 _{6,14} – 18 _{6,13} (A, v _t =0)	134	45
231119.58	19 _{5,15} – 18 _{5,14} (E, v _t =0)	127	47
231134.45	19 _{5,15} – 18 _{5,14} (A, v _t =0)	127	47
231166.48	20 _{3,18} – 19 _{3,17} (E, v _t =0)	125	51
231175.80	20 _{3,18} – 19 _{3,17} (A, v _t =0)	125	51
231919.25	19 _{6,13} – 18 _{6,12} (E, v _t =0)	134	45
231941.42	19 _{6,13} – 18 _{6,12} (A, v _t =0)	134	45
232122.06	21 _{2,20} – 20 _{2,19} (E, v _t =0)	129	54
232127.44	21 _{2,20} – 20 _{2,19} (A, v _t =0)	129	54
232162.92	21 _{1,20} – 20 _{1,19} (E, v _t =0)	129	54
232168.22	21 _{1,20} – 20 _{1,19} (A, v _t =0)	129	54
232207.36	20 _{2,18} – 19 _{2,17} (E, v _t =0)	125	51
232215.67	20 _{2,18} – 19 _{2,17} (A, v _t =0)	125	51
232936.45	22 _{1,22} – 21 _{1,21} (E, v _t =0)	131	58
232936.96	22 _{0,22} – 21 _{0,21} (E, v _t =0)	131	58
232937.34	22 _{1,22} – 21 _{1,21} (A, v _t =0)	131	58
232937.86	22 _{0,22} – 21 _{0,21} (A, v _t =0)	131	58
234852.29	19 _{3,16} – 18 _{3,15} (E, v _t =0)	119	48
234865.90	19 _{3,16} – 18 _{3,15} (A, v _t =0)	119	48
236612.04	19 _{5,14} – 18 _{5,13} (E, v _t =0)	127	47
236634.46	19 _{5,14} – 18 _{5,13} (A, v _t =0)	127	47
239057.88	20 _{4,17} – 19 _{4,16} (E, v _t =0)	132	51
239071.05	20 _{4,17} – 19 _{4,16} (A, v _t =0)	132	51
239701.49	20 _{17,3} – 19 _{17,2} (A, v _t =0)	312	29
239713.67	20 _{17,3} – 19 _{17,2} (E, v _t =0)	312	15
239722.66	20 _{17,4} – 19 _{17,3} (E, v _t =0)	311	15
239753.19	20 _{16,4} – 19 _{16,3} (A, v _t =0)	290	38
239762.20	20 _{16,4} – 19 _{16,3} (E, v _t =0)	290	19
239774.25	20 _{16,5} – 19 _{16,4} (E, v _t =0)	290	19
239823.13	20 _{15,5} – 19 _{15,4} (A, v _t =0)	269	46
239828.73	20 _{15,5} – 19 _{15,4} (E, v _t =0)	269	23
239843.52	20 _{15,6} – 19 _{15,5} (E, v _t =0)	269	23
239916.19	20 _{14,6} – 19 _{14,5} (A, v _t =0)	250	54
239918.24	20 _{14,6} – 19 _{14,5} (E, v _t =0)	250	27
239935.36	20 _{14,7} – 19 _{14,6} (E, v _t =0)	250	27
240037.71	20 _{13,7} – 19 _{13,6} (E, v _t =0)	232	31
240039.29	20 _{13,7} – 19 _{13,6} (A, v _t =0)	232	61
240056.72	20 _{13,8} – 19 _{13,7} (E, v _t =0)	232	31
240197.23	20 _{12,8} – 19 _{12,7} (E, v _t =0)	216	34
240202.45	20 _{12,8} – 19 _{12,7} (A, v _t =0)	216	68
240217.65	20 _{12,9} – 19 _{12,8} (E, v _t =0)	216	34
240411.94	20 _{11,9} – 19 _{11,8} (E, v _t =0)	201	37
240420.72	20 _{11,9} – 19 _{11,8} (A, v _t =0)	201	74
240433.26	20 _{11,10} – 19 _{11,9} (E, v _t =0)	201	37
240705.48	20 _{10,10} – 19 _{10,9} (E, v _t =0)	187	40
240717.70	20 _{10,11} – 19 _{10,10} (A, v _t =0)	187	40
240717.71	20 _{10,10} – 19 _{10,9} (A, v _t =0)	187	40

TABLE B1—*Continued*

Frequency (MHz)	Transition	E_{up} (K)	$S\mu^2$ (D ²)
240727.18	20 _{10,11} – 19 10, ₁₀ (E, v _t =0)	187	40
240913.49	19 _{4,15} – 18 4, ₁₄ (E, v _t =0)	123	48
240935.52	19 _{4,15} – 18 4, ₁₄ (A, v _t =0)	123	48
241116.89	20 _{9,11} – 19 9, ₁₀ (E, v _t =0)	175	42
241132.23	20 _{9,12} – 19 9, ₁₁ (A, v _t =0)	175	42
241132.60	20 _{9,11} – 19 9, ₁₀ (A, v _t =0)	175	42
241138.48	20 _{9,12} – 19 9, ₁₁ (E, v _t =0)	175	42
241633.54	21 _{3,19} – 20 3, ₁₈ (E, v _t =0)	137	54
241642.63	21 _{3,19} – 20 3, ₁₈ (A, v _t =0)	137	54
241716.12	20 _{8,12} – 19 8, ₁₁ (E, v _t =0)	163	45
241730.37	20 _{8,13} – 19 8, ₁₂ (A, v _t =0)	163	45
241736.77	20 _{8,13} – 19 8, ₁₂ (E, v _t =0)	163	45
241738.89	20 _{8,12} – 19 8, ₁₁ (A, v _t =0)	163	45
242319.95	21 _{2,19} – 20 2, ₁₈ (E, v _t =0)	137	54
242328.23	21 _{2,19} – 20 2, ₁₈ (A, v _t =0)	137	54
242482.49	22 _{2,21} – 21 2, ₂₀ (E, v _t =0)	140	57
242487.79	22 _{2,21} – 21 2, ₂₀ (A, v _t =0)	140	57
242506.56	22 _{1,21} – 21 1, ₂₀ (E, v _t =0)	140	57
242511.81	22 _{1,21} – 21 1, ₂₀ (A, v _t =0)	140	57
242596.37	20 _{7,14} – 19 7, ₁₃ (A, v _t =0)	154	47
242616.50	20 _{7,14} – 19 7, ₁₃ (E, v _t =0)	154	45
242691.15	20 _{7,13} – 19 7, ₁₂ (E, v _t =0)	154	45
242734.89	20 _{7,13} – 19 7, ₁₂ (A, v _t =0)	154	47
243156.72	20 _{5,16} – 19 5, ₁₅ (E, v _t =0)	138	50
243172.14	20 _{5,16} – 19 5, ₁₅ (A, v _t =0)	138	50
243297.31	23 _{0,23} – 22 1, ₂₂ (E, v _t =0)	143	10
243297.65	23 _{1,23} – 22 1, ₂₂ (E, v _t =0)	143	60
243297.94	23 _{0,23} – 22 0, ₂₂ (E, v _t =0)	143	61
243298.14	23 _{0,23} – 22 1, ₂₂ (A, v _t =0)	143	10
243298.28	23 _{1,23} – 22 0, ₂₂ (E, v _t =0)	143	10
243298.48	23 _{1,23} – 22 1, ₂₂ (A, v _t =0)	143	60
243298.77	23 _{0,23} – 22 0, ₂₂ (A, v _t =0)	143	60
243299.11	23 _{1,23} – 22 0, ₂₂ (A, v _t =0)	143	10
243542.01	20 _{6,15} – 19 6, ₁₄ (E, v _t =0)	145	48
243553.64	20 _{6,15} – 19 6, ₁₄ (A, v _t =0)	145	48
244947.97	20 _{3,17} – 19 3, ₁₆ (E, v _t =0)	131	51
244960.05	20 _{3,17} – 19 3, ₁₆ (A, v _t =0)	131	51
244976.72	20 _{6,14} – 19 6, ₁₃ (E, v _t =0)	146	48
244996.93	20 _{6,14} – 19 6, ₁₃ (A, v _t =0)	146	48

^aThis Table lists the detected, blended, partially blended and optically thin lines of HCOOCH₃. Transitions that are emitting with an intensity less or equal to 3 times the noise level and that we used to constrain our model are also listed. Transitions with the * symbol, are transitions we estimate to be optically thick.

C. Methyl formate emission towards the Orion-KL Compact Ridge as observed with ALMA

Figures C-1, C-2 and C-3 show the respective spectra of the detected HCOOCH_3 , $\text{H}^{13}\text{COOCH}_3$ and $\text{HCOO}^{13}\text{CH}_3$ transitions observed with ALMA toward the Orion-KL Compact Ridge during the science verification program, along with our best models achieved using the XCLASS program.

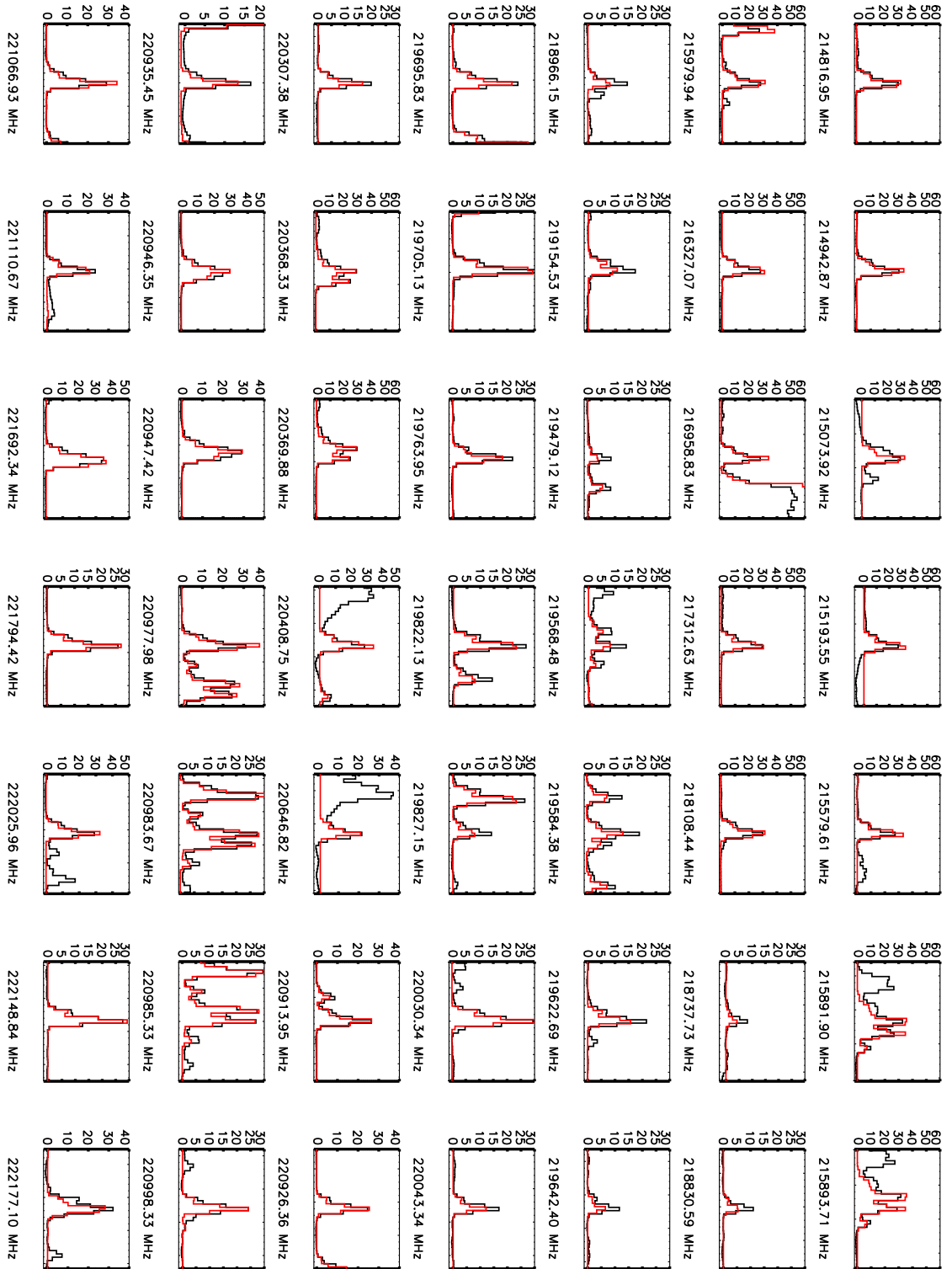


Fig. C-1.— HCOOCH₃ spectra (black) towards the Compact Ridge component associated with Orion-KL and model (red), as observed with ALMA. The intensity scale is in T_{MB} (K). The x-axis scale is about ± 9.5 MHz centered on the line rest frequency, which is indicated below each plot.

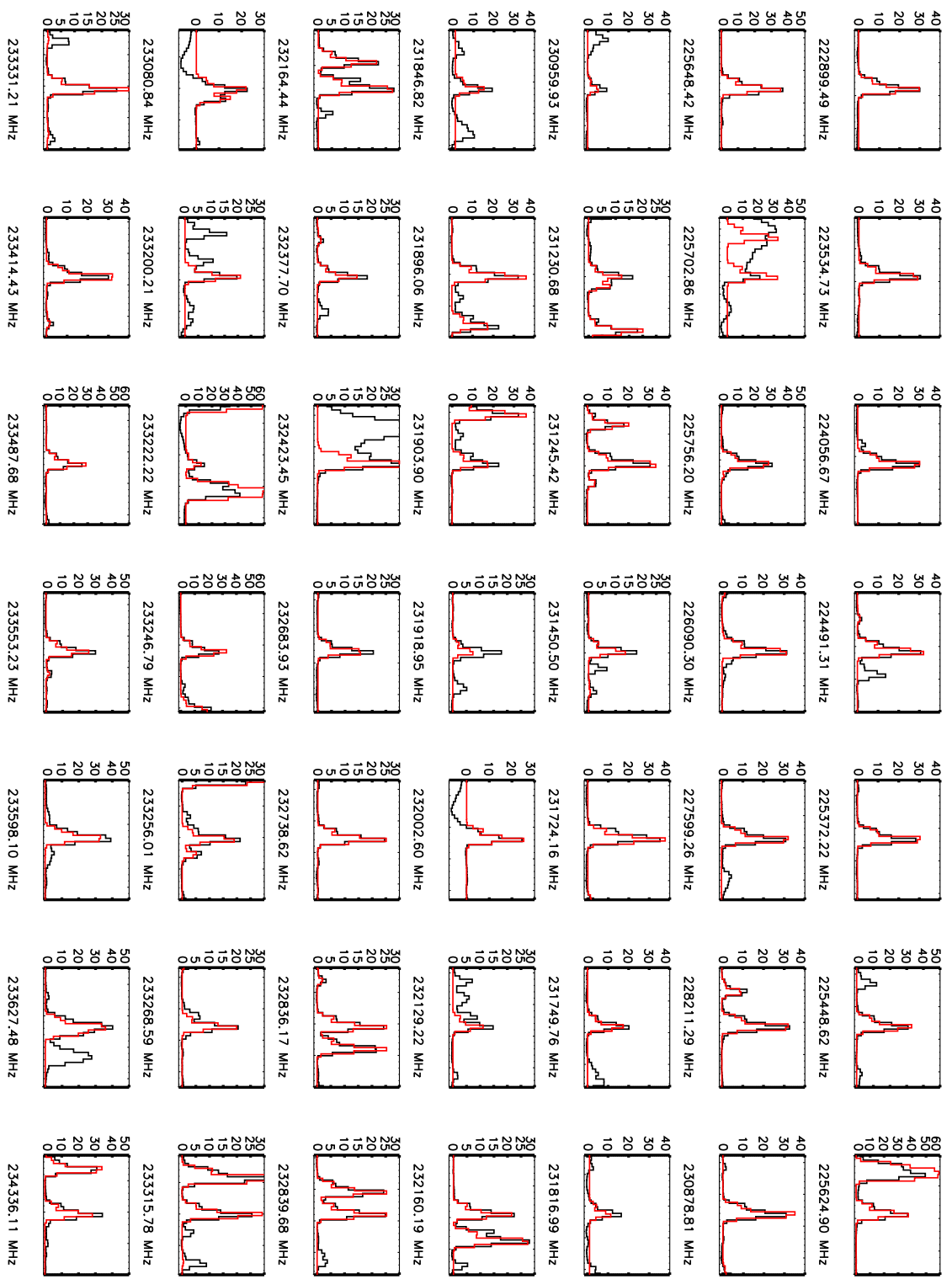


Fig. C-1.— Continue

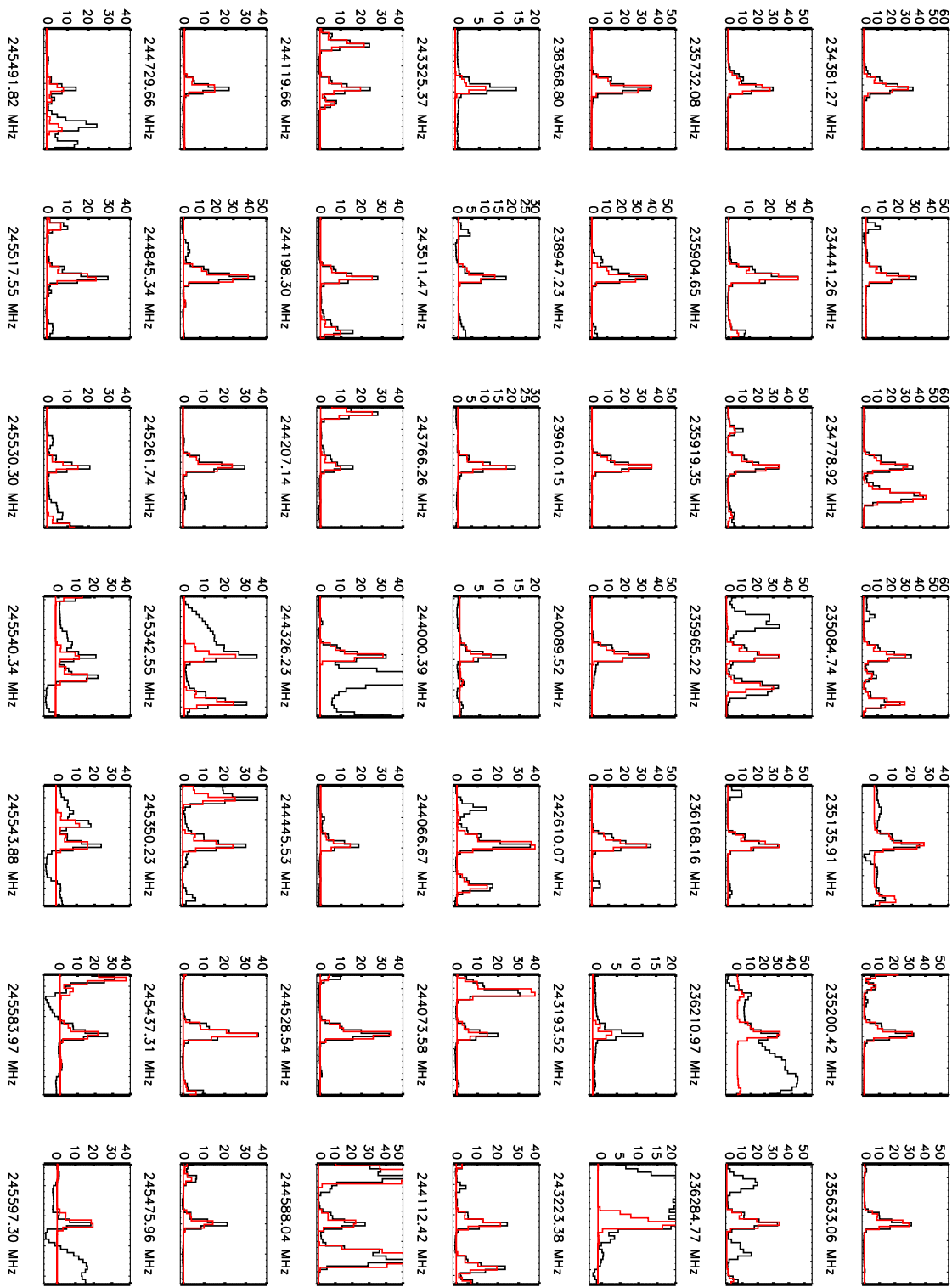


Fig. C-1.— Continue.

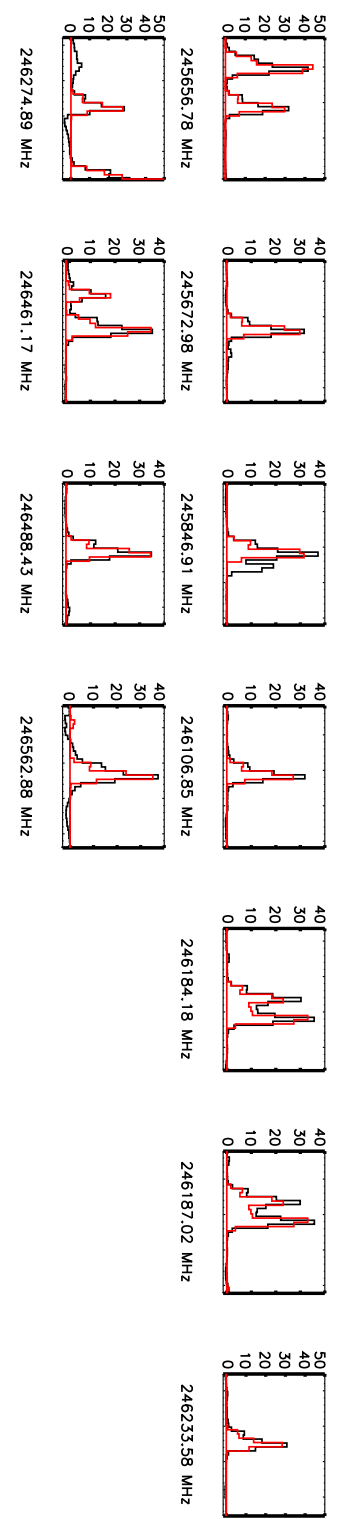


Fig. C-1.— Continue.

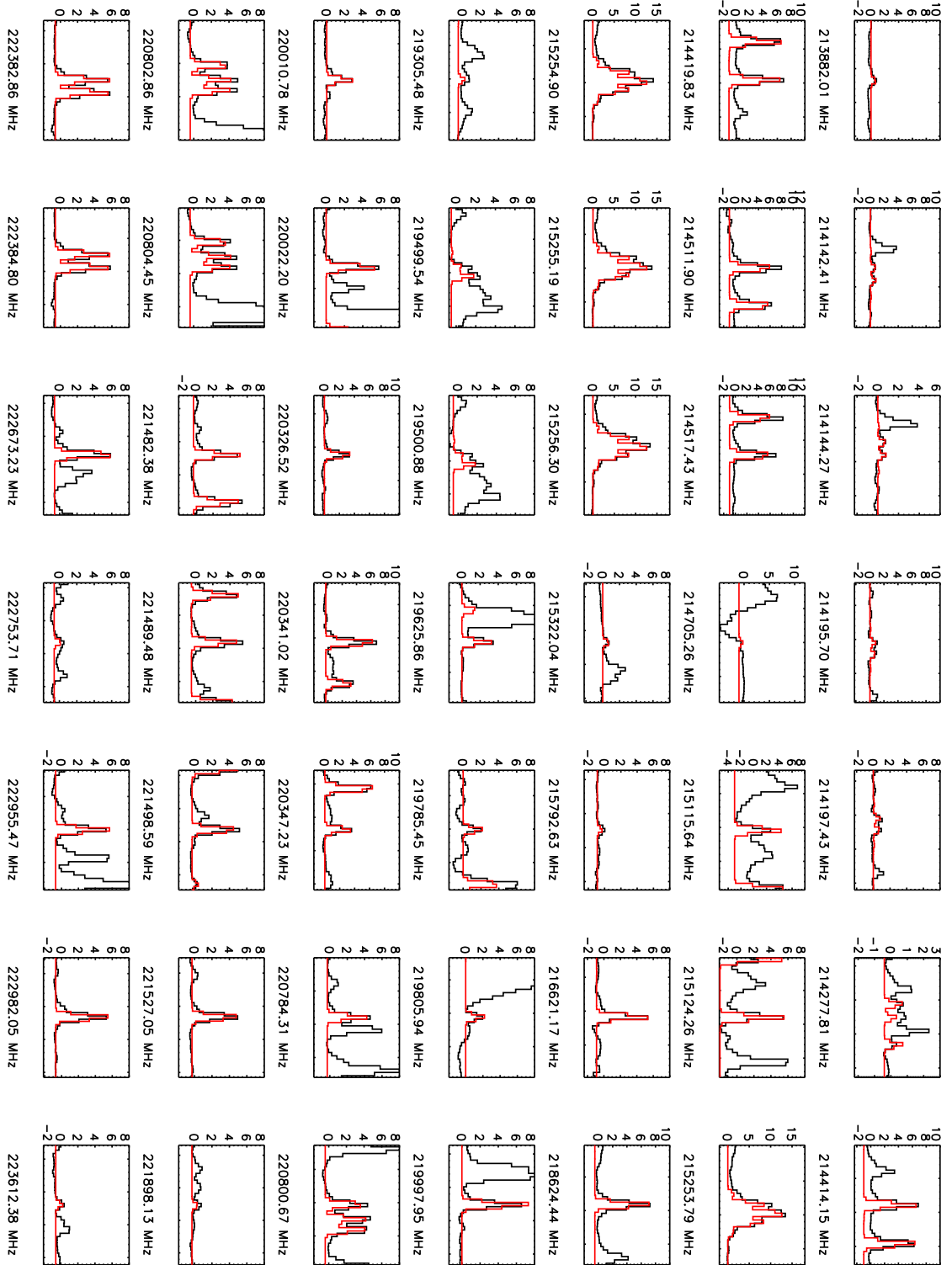


Fig. C-2.— $\text{H}^{13}\text{COOCH}_3$ spectra (black) towards the Compact Ridge component associated with Orion-KL and model (red), as observed with ALMA. The intensity scale is in T_{MB} (K). The x-axis scale is about ± 9.5 MHz centered on the line rest frequency, which is indicated below each plot.

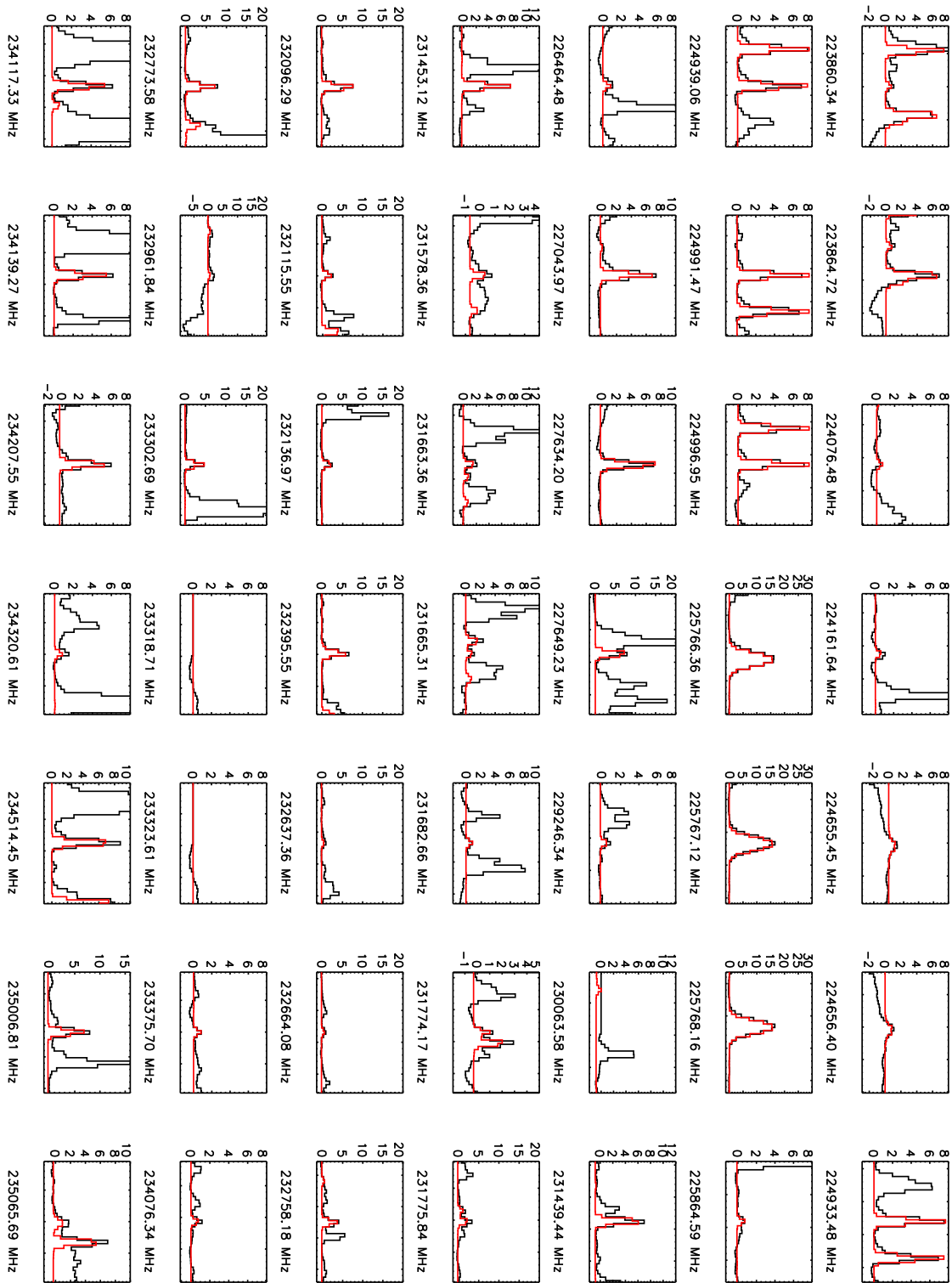


Fig. C-2.— Continue.

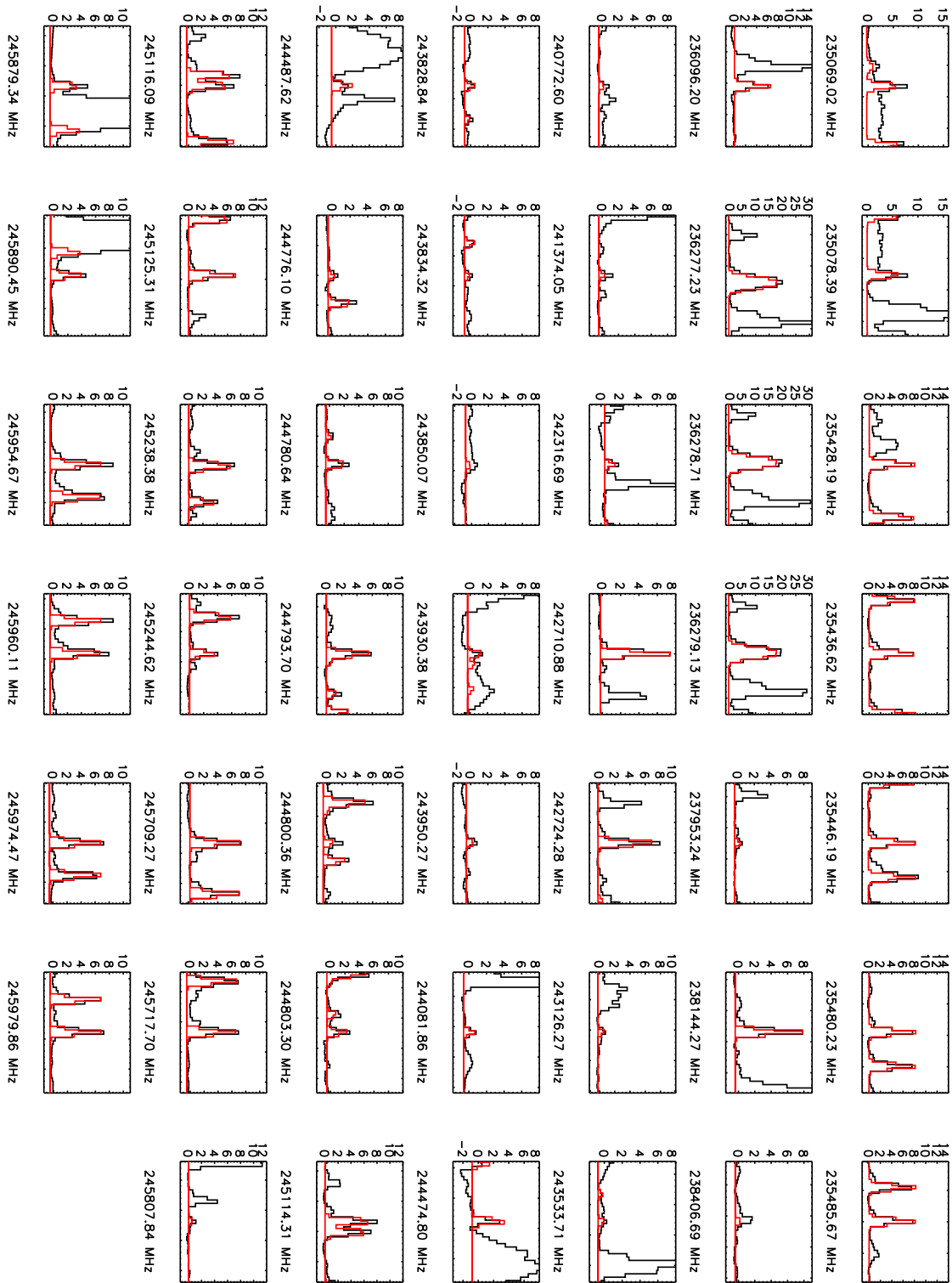


Fig. C-2.— Continue.

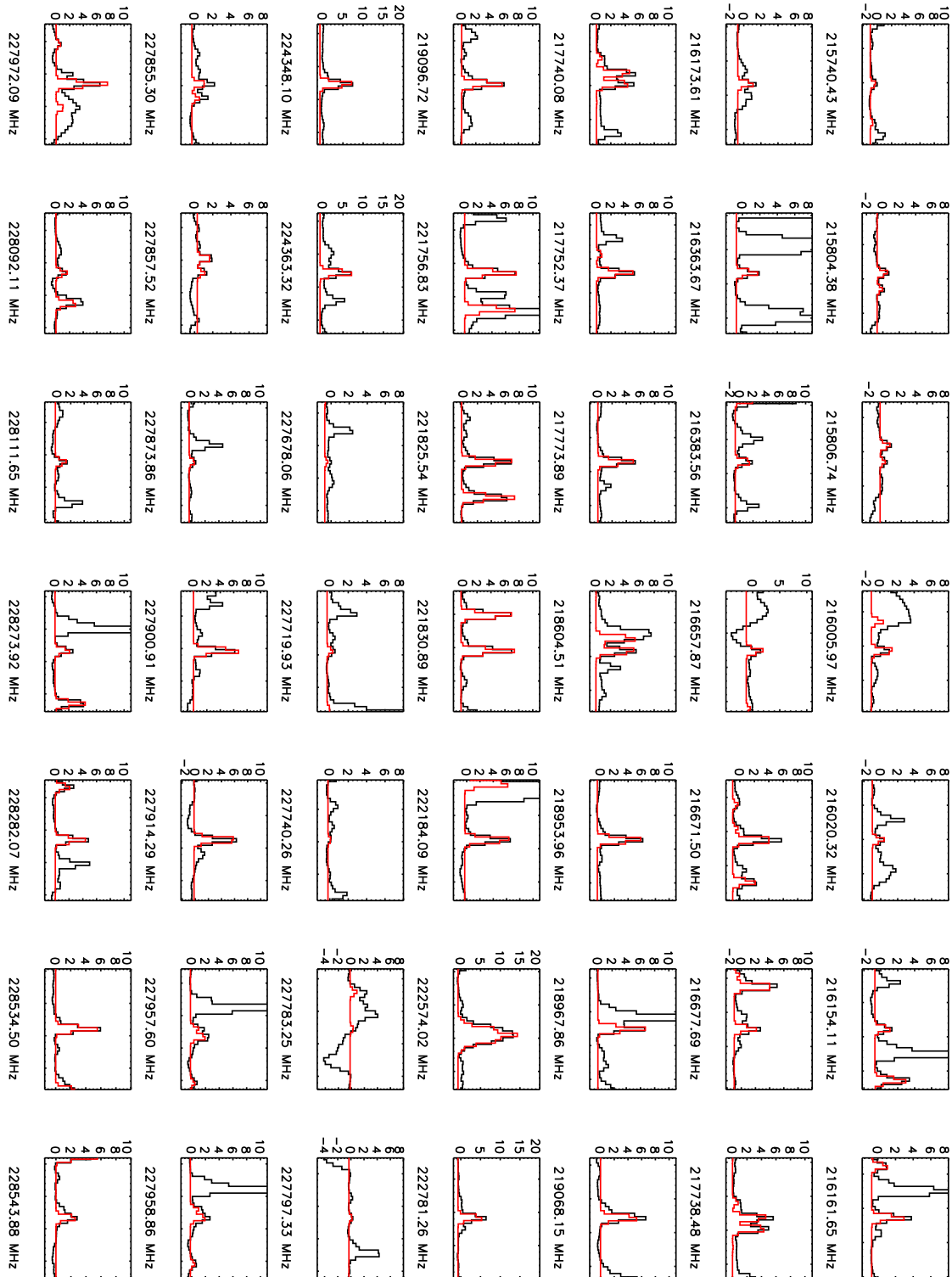


Fig. C-3.— $\text{HCOO}^{13}\text{CH}_3$ spectra (black) towards the Compact Ridge component associated with Orion-KL and model (red), as observed with ALMA. The intensity scale is in T_{MB} (K). The x-axis scale is about ± 9.5 MHz centered on the line rest frequency, which is indicated below each plot.

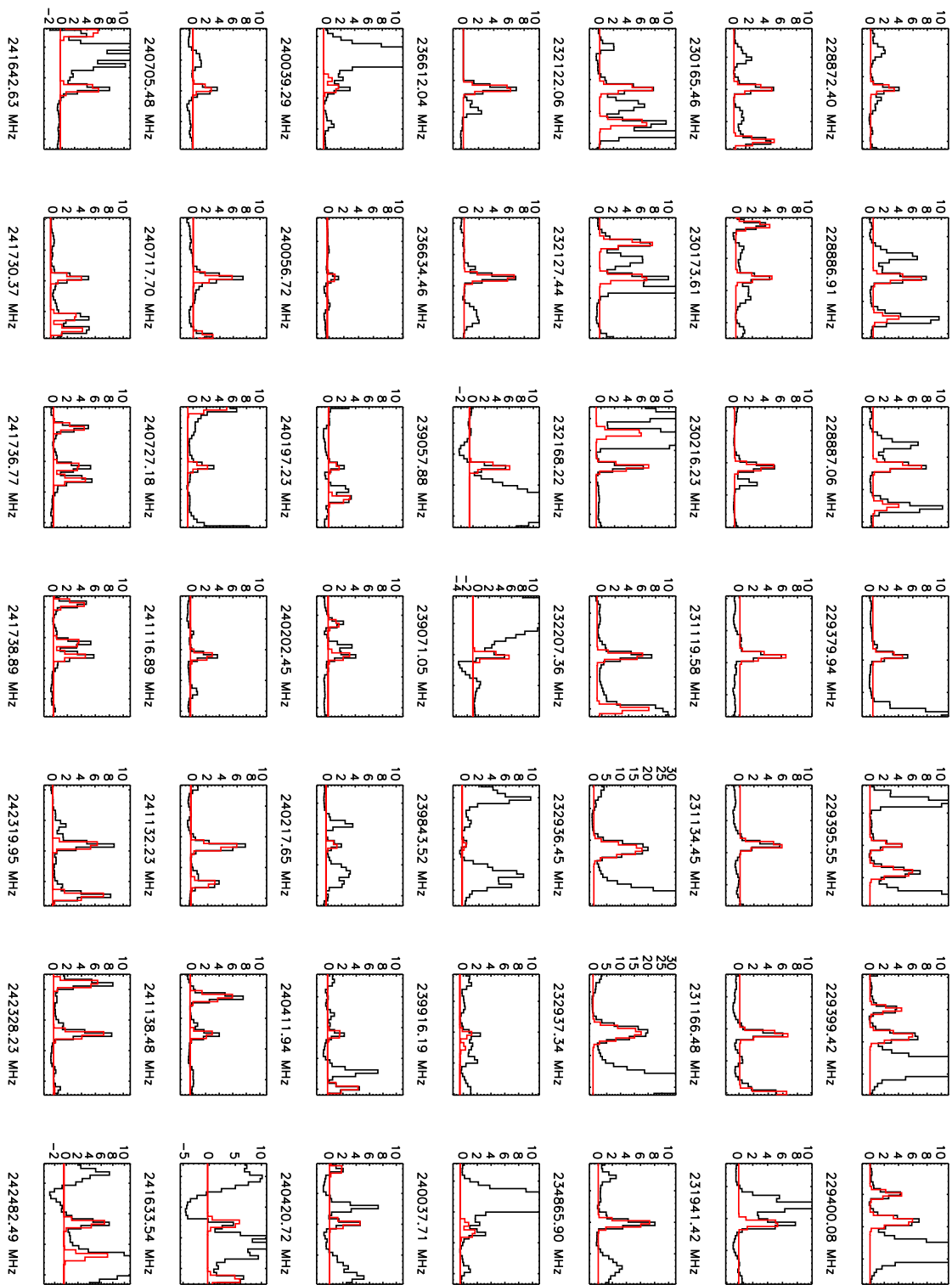


Fig. C-3.— Continue.

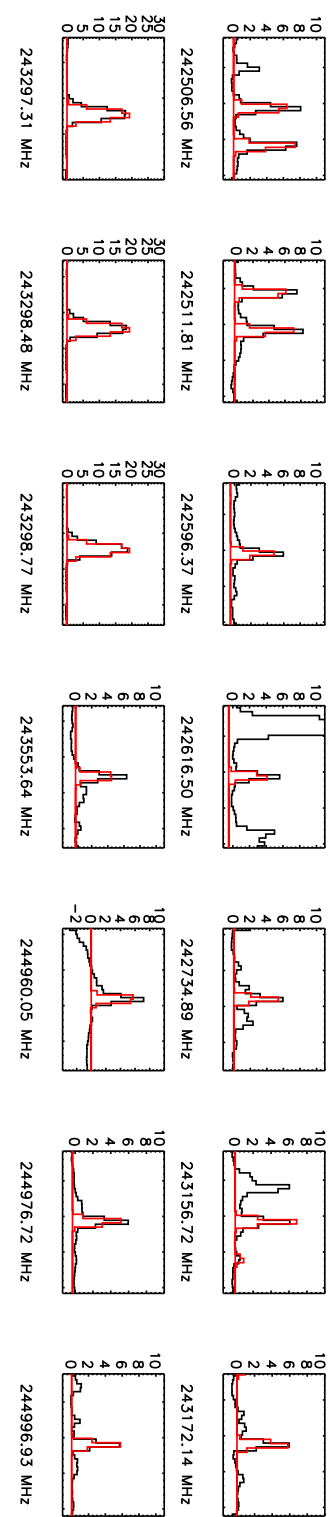


Fig. C-3.— Continue.

D. Methyl formate emission towards the Orion-KL Hot Core-SW as observed with ALMA

Figures D-1, D-2 and D-3 show the respective spectra of the detected HCOOCH_3 , $\text{H}^{13}\text{COOCH}_3$ and $\text{HCOO}^{13}\text{CH}_3$ transitions observed with ALMA toward the Orion-KL Hot Core-SW during the science verification program, along with our best models achieved using the XCLASS program.

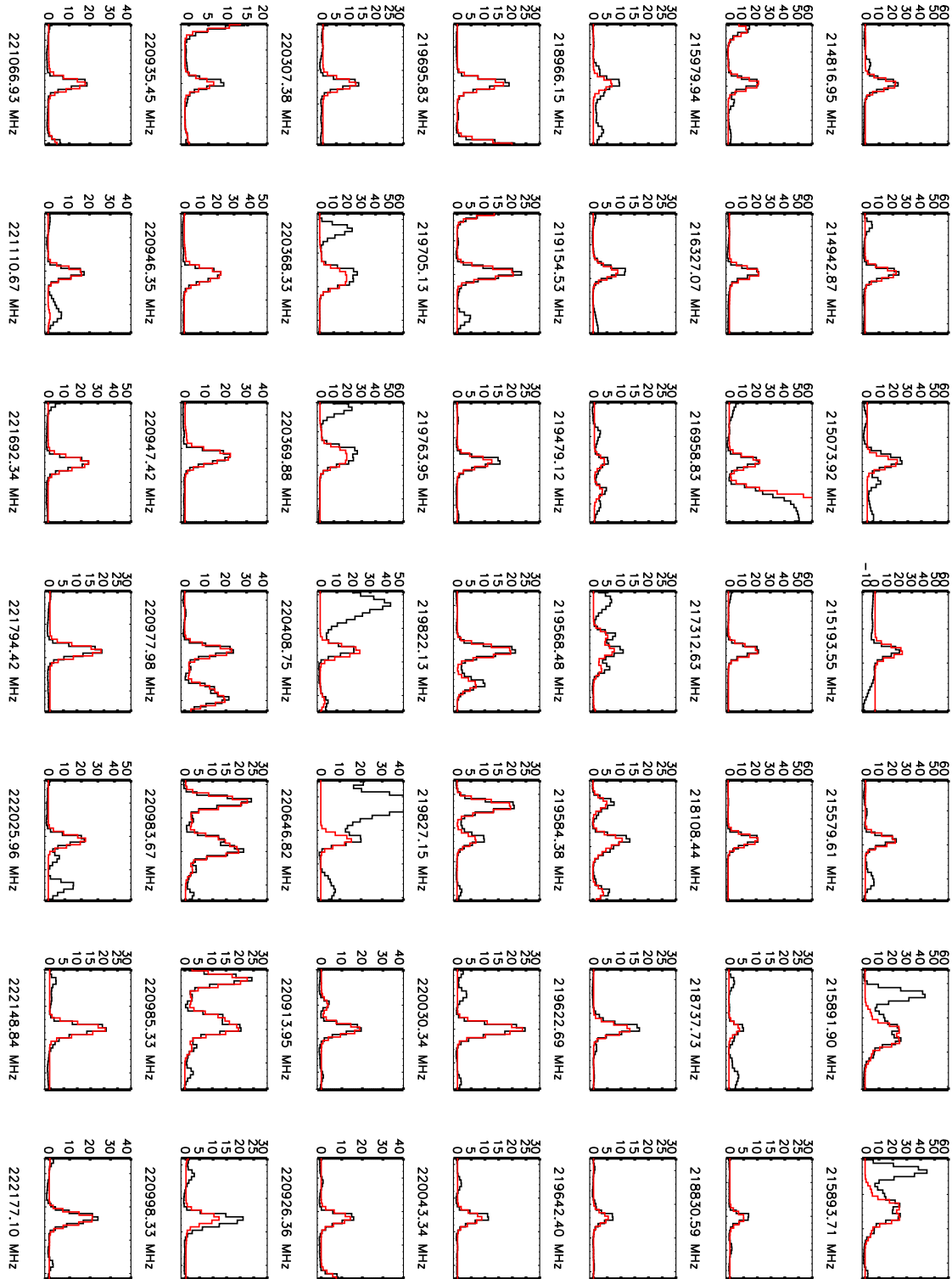


Fig. D-1.— HCOOCH_3 spectra (black) towards the Hot Core-SW component associated with Orion-KL and model (red), as observed with ALMA. The intensity scale is in T_{MB} (K). The x-axis scale is about ± 9.5 MHz centered on the line rest frequency, which is indicated below each plot.

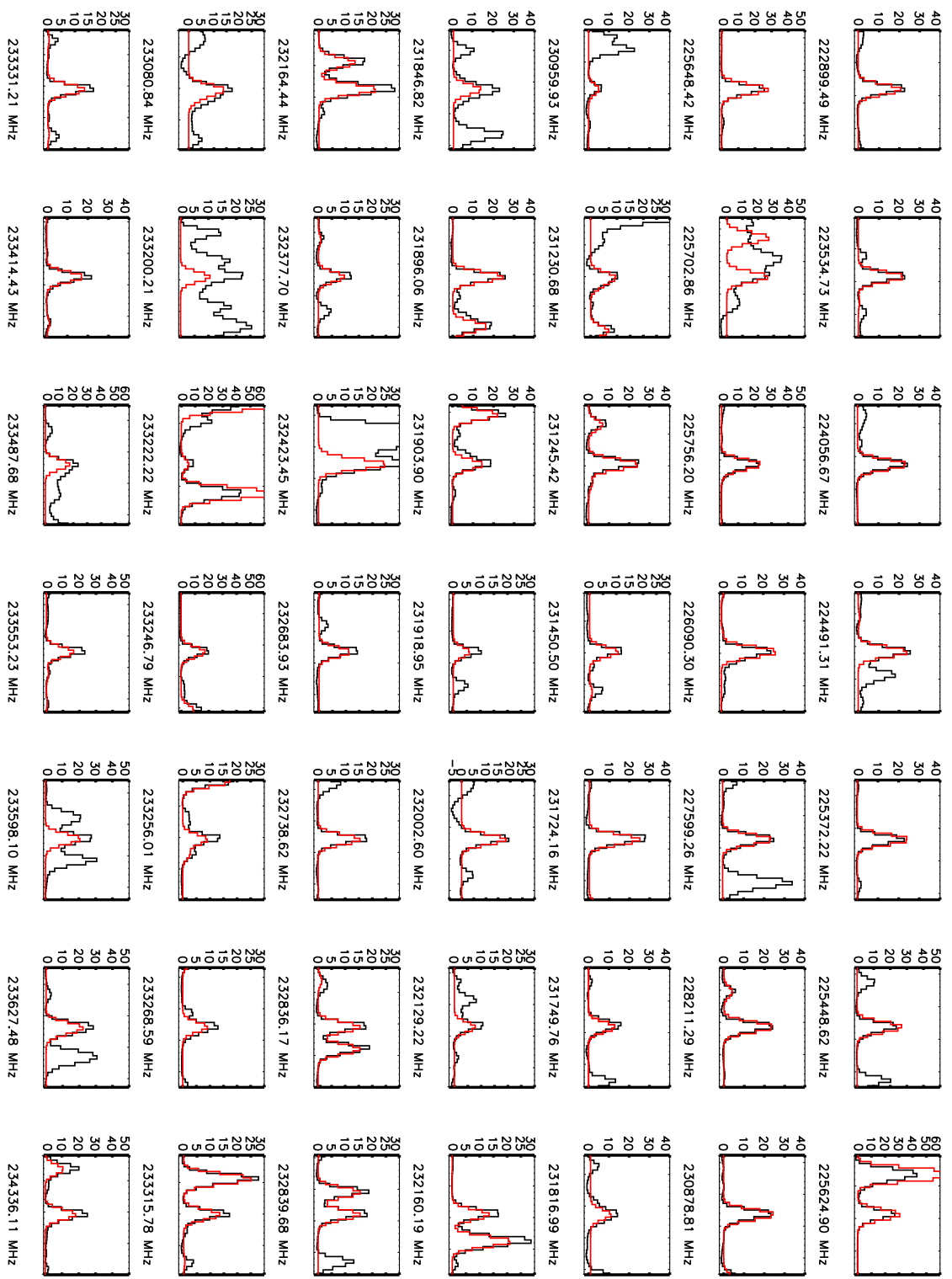


Fig. D-1.— Continue

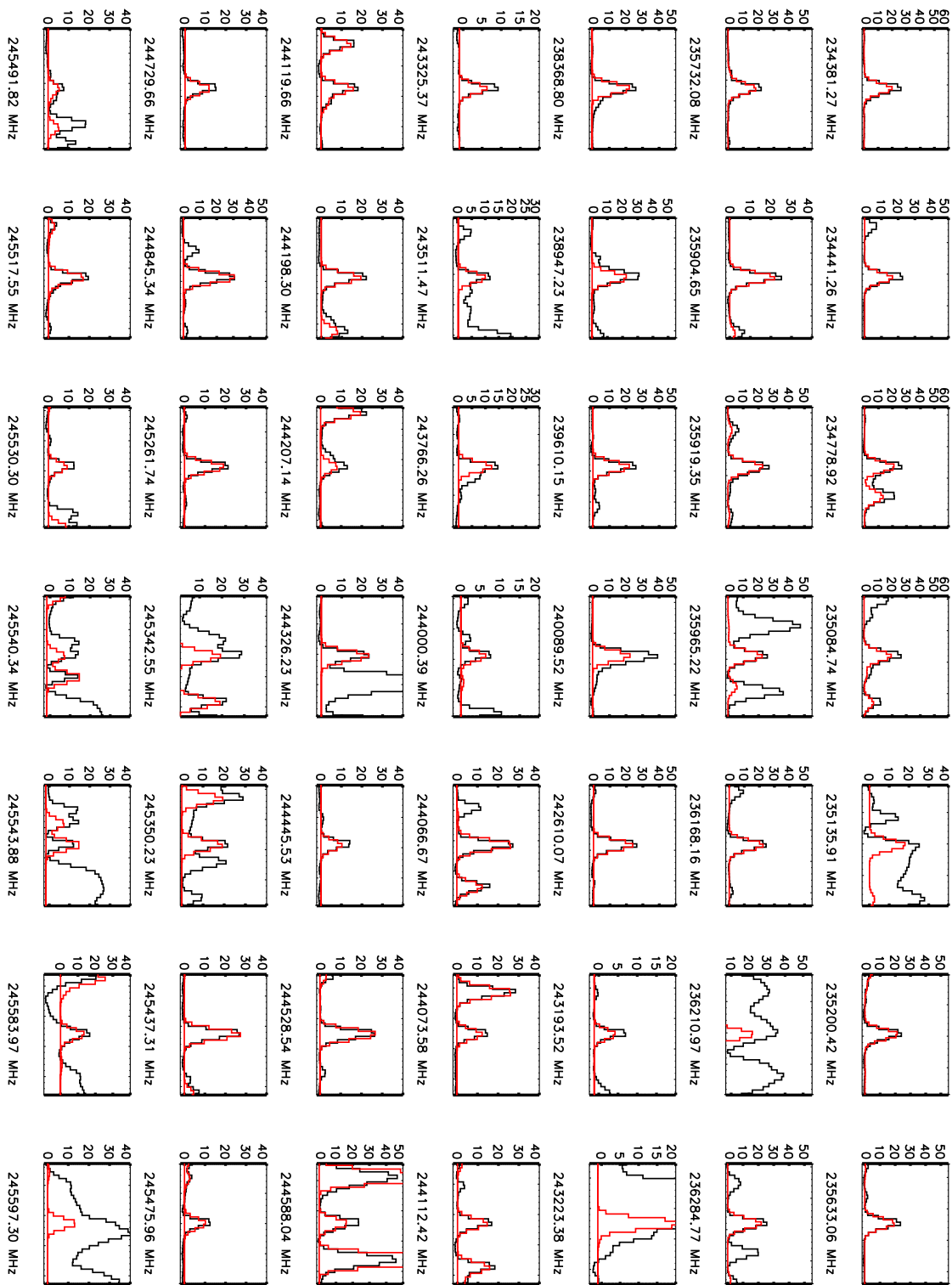


Fig. D-1.— Continue.

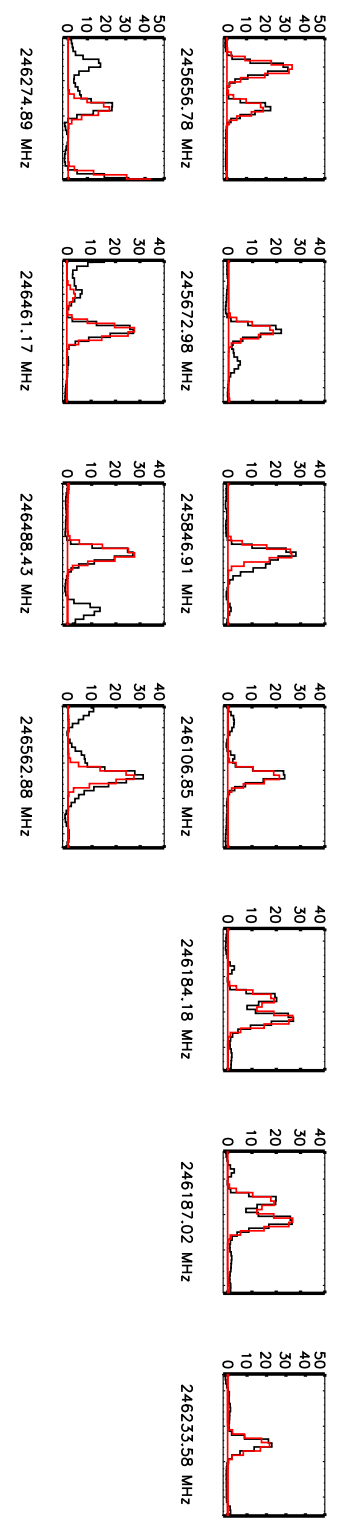


Fig. D-1.— Continue.

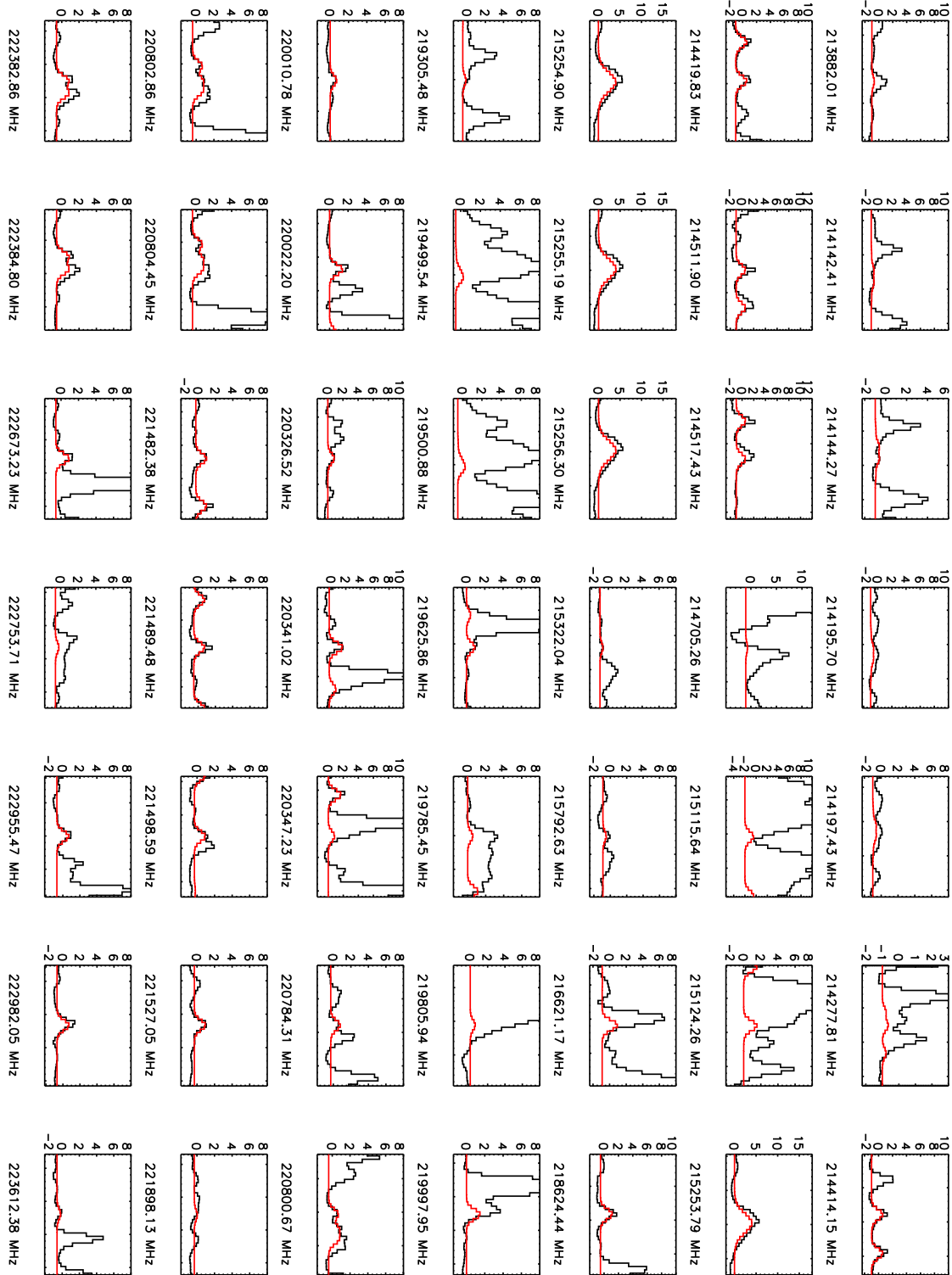


Fig. D-2.— $\text{H}^{13}\text{COOCH}_3$ spectra (black) towards the Hot Core-SW component associated with Orion-KL and model (red), as observed with ALMA. The intensity scale is in T_{MB} (K). The x-axis scale is about ± 9.5 MHz centered on the line rest frequency, which is indicated below each plot.

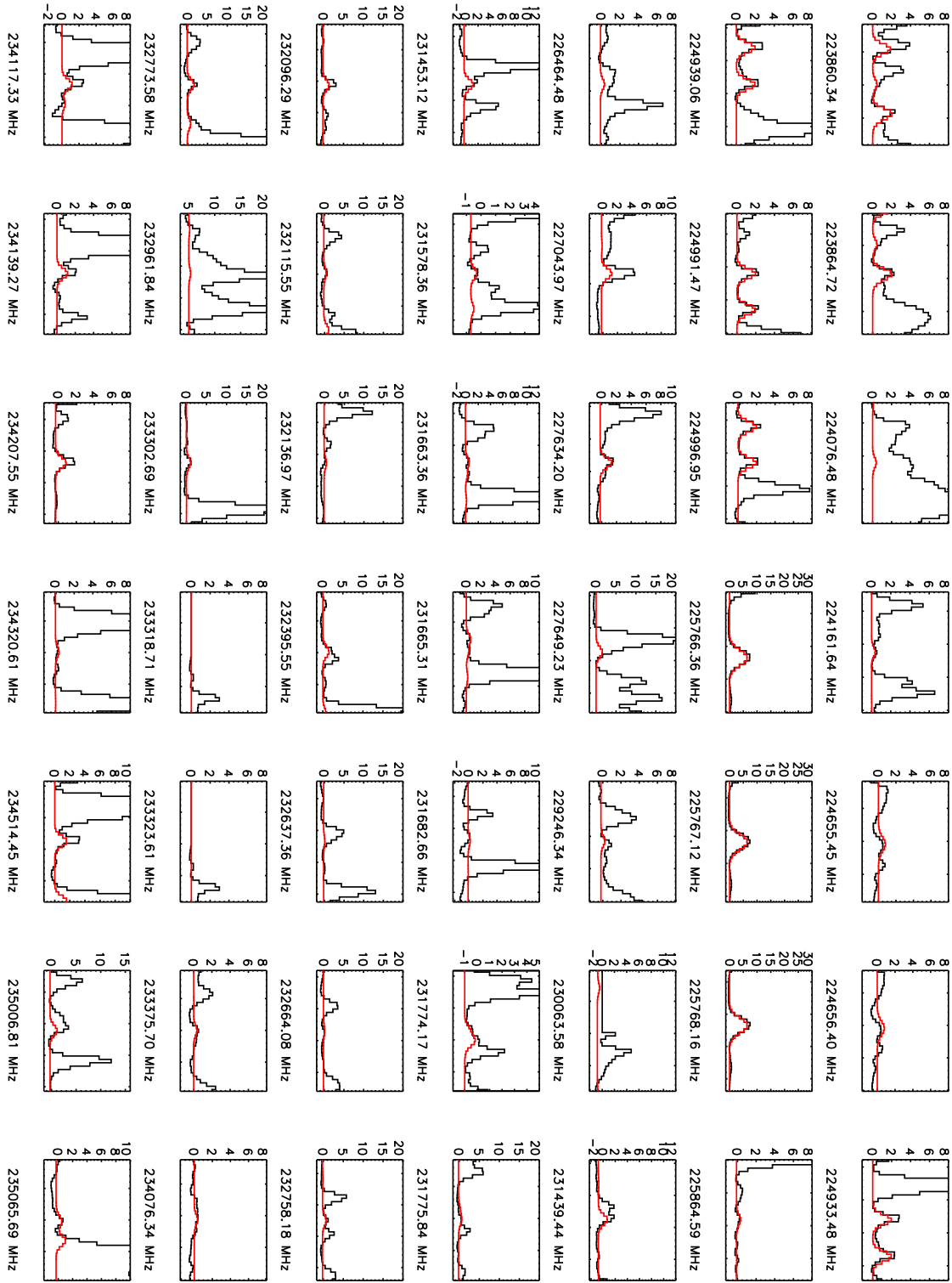


Fig. D-2.— Continue.

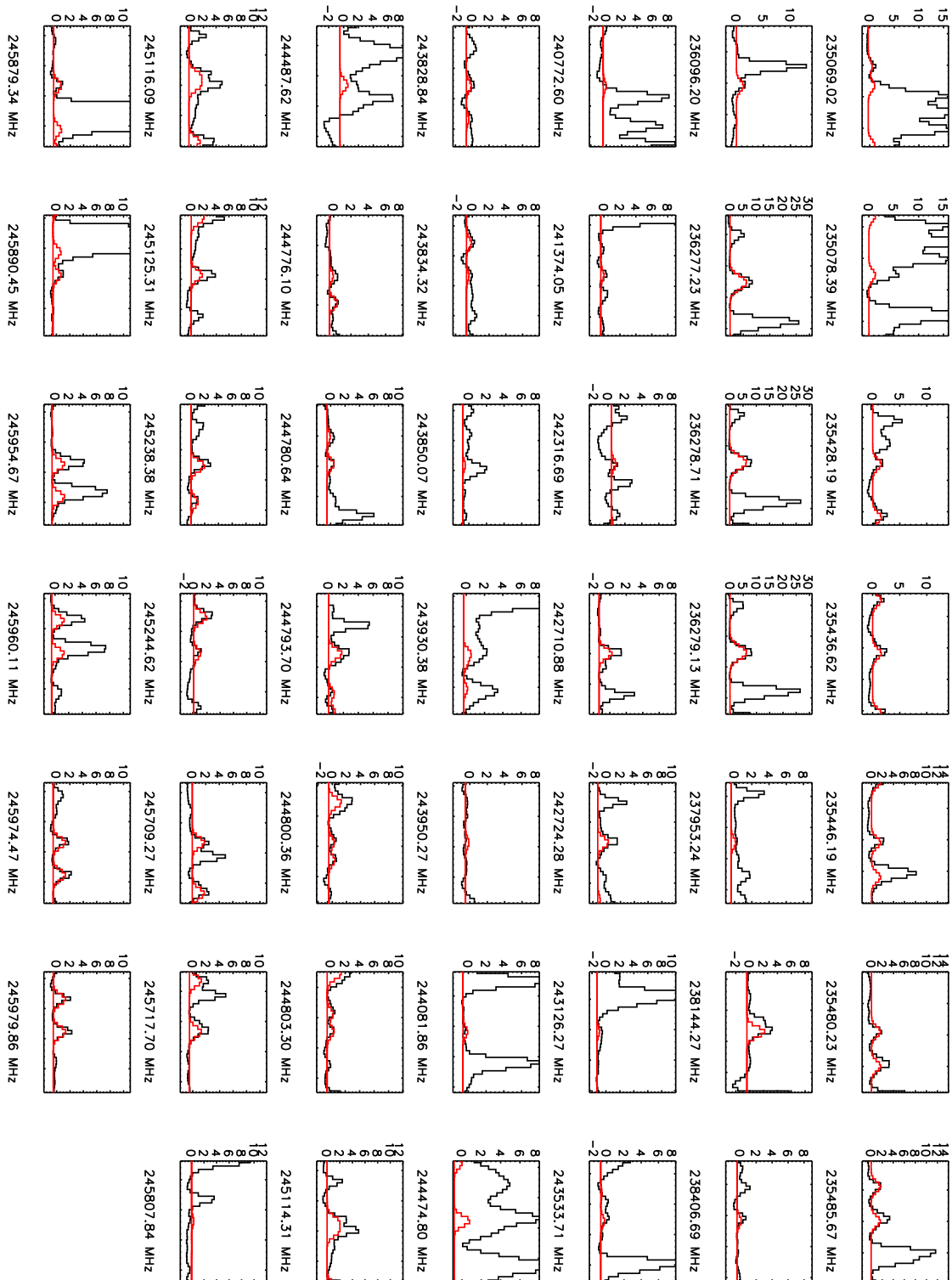


Fig. D-2.— Continue.

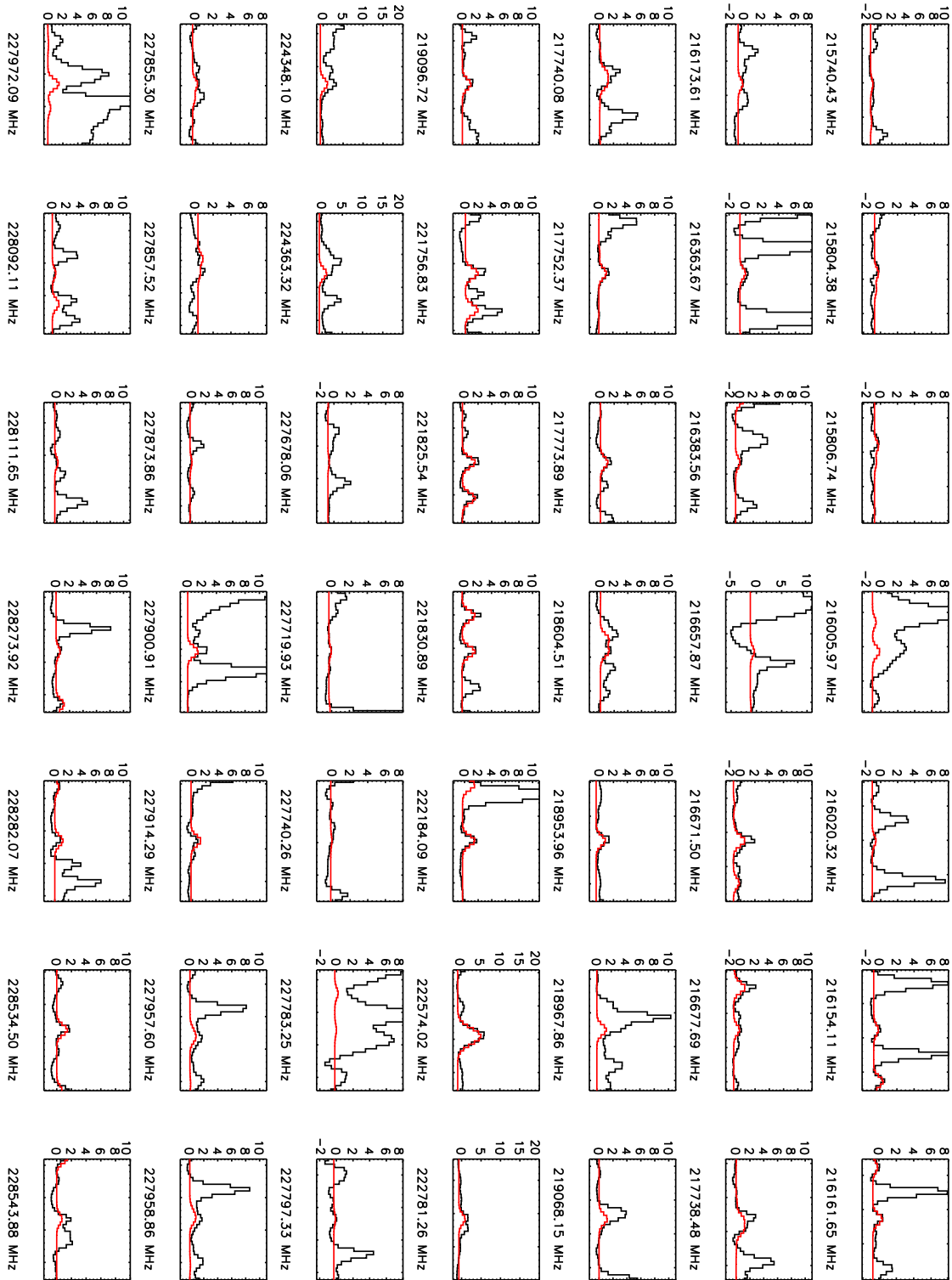


Fig. D-3.— $\text{HCOO}^{13}\text{CH}_3$ spectra (black) towards the Hot Core-SW component associated with Orion-KL and model (red), as observed with ALMA. The intensity scale is in T_{MB} (K). The x-axis scale is about ± 9.5 MHz centered on the line rest frequency, which is indicated below each plot.

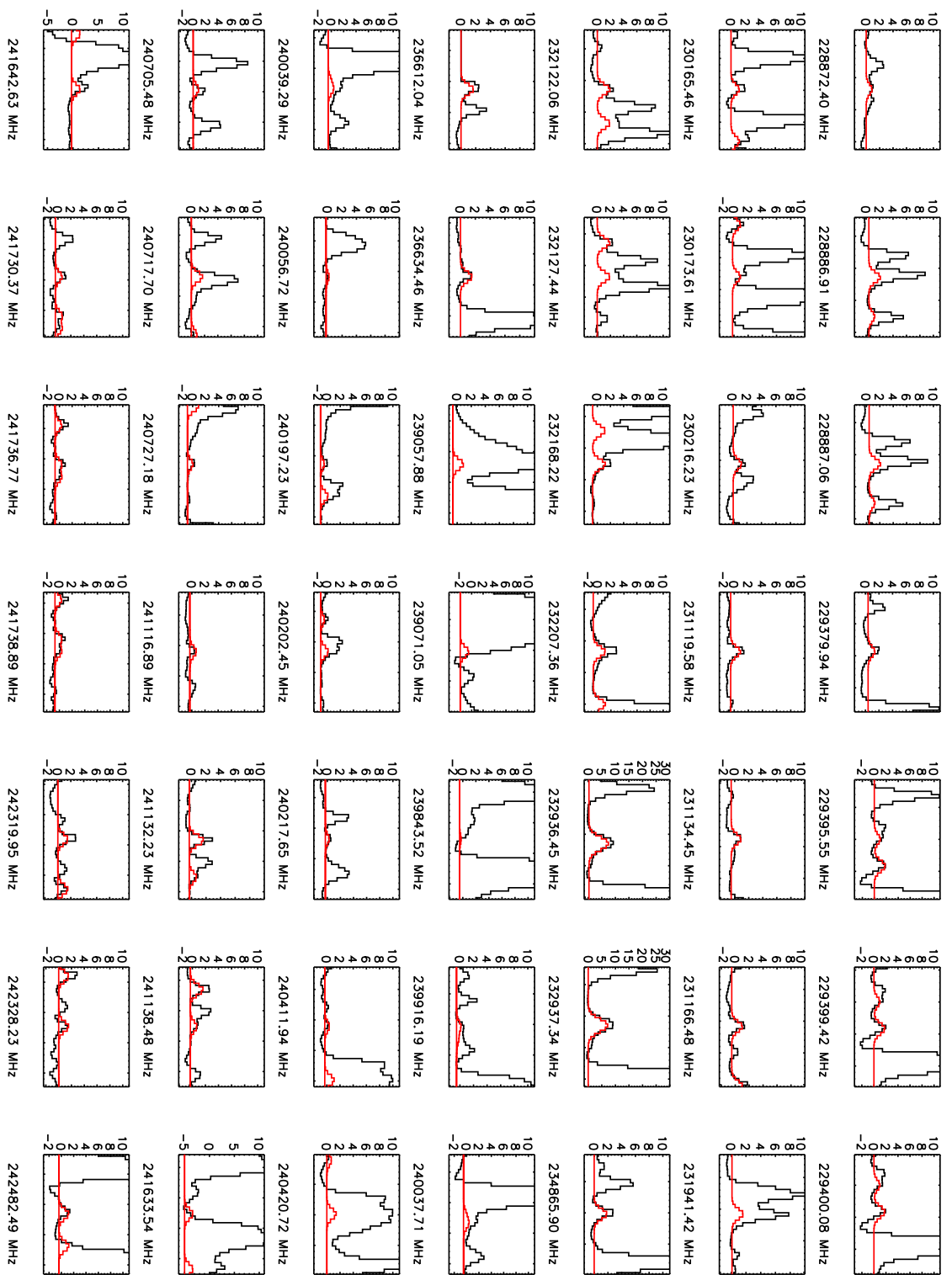


Fig. D-3.— Continue.

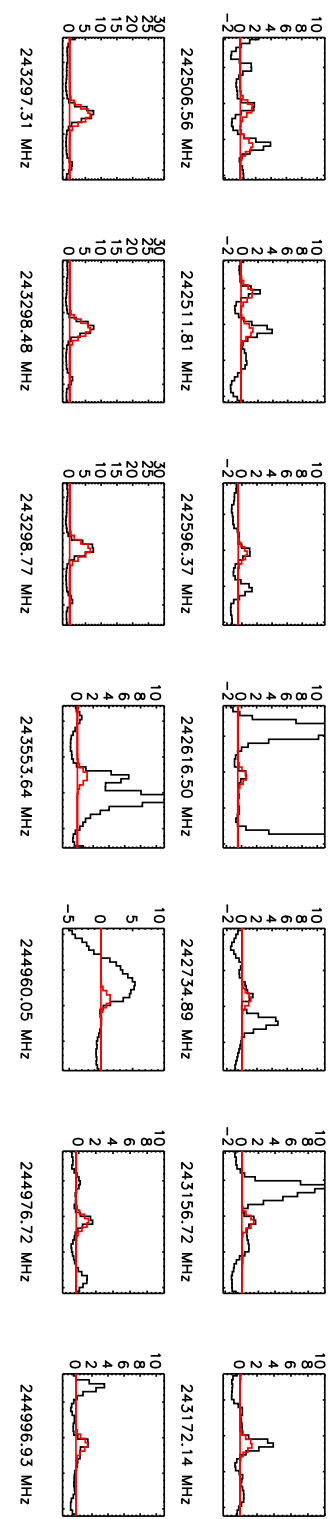


Fig. D-3.— Continue.

REFERENCES

- Belloche, A., Garrod, R. T., Müller, H. S. P., et al. 2009, *A&A*, 499, 215
- Belloche, A., Menten, K. M., Comito, C., et al. 2008, *A&A*, 482, 179
- Beltrán, M. T., Cesaroni, R., Zhang, Q., et al. 2011, *A&A*, 532, A91
- Bennett, C. J., & Kaiser, R. I. 2007, *ApJ*, 661, 899
- Bergin, E. A., Phillips, T. G., Comito, C., et al. 2010, *A&A*, 521, L20
- Beuther, H., Zhang, Q., Bergin, E. A., & Sridharan, T. K. 2009, *ApJ*, 137, 406
- Beuther, H., Zhang, Q., Bergin, E. A., et al. 2007, *A&A*, 468, 1045
- Beuther, H., Zhang, Q., Greenhill, L. J., et al. 2005, *ApJ*, 632, 355
- Bisschop, S. E., Jørgensen, J. K., van Dishoeck, E. F., & de Wachter, E. B. M. 2007, *A&A*, 465, 913
- Blake, G. A., Mundy, L. G., Carlstrom, J. E., et al. 1996, *ApJ*, 472, L49
- Blake, G. A., Sutton, E. C., Masson, C. R., & Phillips, T. G. 1987, *ApJ*, 315, 621
- Briggs, D. S. 1995, in Bulletin of the American Astronomical Society, Vol. 27, American Astronomical Society Meeting Abstracts, 1444
- Bunker, P. R., & Jensen, P., eds. 1998, Molecular symmetry and spectroscopy
- Carvajal, M., Kleiner, I., & Demaison, J. 2010, *ApJS*, 190, 315
- Carvajal, M., Willaert, F., Demaison, J., & Kleiner, I. 2007, Journal of Molecular Spectroscopy, 246, 158
- Carvajal, M., Margulès, L., Tercero, B., et al. 2009, *A&A*, 500, 1109
- Chao, J., Hall, K. R., Marsh, K. N., & Wilhoit, R. C. 1986, Journal of Physical and Chemical Reference Data, 15, 1369
- Charnley, S. B., Ehrenfreund, P., Millar, T. J., et al. 2004, *MNRAS*, 347, 157
- Charnley, S. B., & Rodgers, S. D. 2005, in IAU Symposium, Vol. 231, Astrochemistry: Recent Successes and Current Challenges, ed. D. C. Lis, G. A. Blake, & E. Herbst, 237–246
- Clark, B. G. 1980, *A&A*, 89, 377
- Crockett, N. R., Bergin, E. A., Wang, S., et al. 2010, *A&A*, 521, L21+
- Crockett, N. R., Bergin, E. A., Neill, J. L., et al. 2014, *ApJ*, 787, 112
- Cuppen, H. M., van Dishoeck, E. F., Herbst, E., & Tielens, A. G. G. M. 2009, *A&A*, 508, 275
- Demyk, K., Włodarczak, G., & Carvajal, M. 2008, *A&A*, 489, 589
- Favre, C., Despois, D., Brouillet, N., et al. 2011, *A&A*, 532, A32
- Fontani, F., Pascucci, I., Caselli, P., et al. 2007, *A&A*, 470, 639
- Friedel, D. N., & Snyder, L. E. 2008, *ApJ*, 672, 962
- Friedel, D. N., & Widicus Weaver, S. L. 2012, *ApJS*, 201, 17
- Garrod, R. T., & Herbst, E. 2006, *A&A*, 457, 927
- Garrod, R. T., Weaver, S. L. W., & Herbst, E. 2008, *ApJ*, 682, 283
- Groner, P., Winnewisser, M., Medvedev, I. R., et al. 2007, *ApJS*, 169, 28
- Haykal, I., Carvajal, M., Tercero, B., et al. 2014, *A&A*, 568, A58
- Herbst, E., Messer, J. K., de Lucia, F. C., & Helminger, P. 1984, Journal of Molecular Spectroscopy, 108, 42
- Herbst, E., & van Dishoeck, E. F. 2009, *ARA&A*, 47, 427
- Herzberg, G. 1991, Spectra and Molecular Structure: II. Infrared and Raman Spectra of Polyatomic Molecules (Krieger Pub. Co., Malabar, Florida)

- Hollis, J. M., Lovas, F. J., & Jewell, P. R. 2000, ApJ, 540, L107
- Hollis, J. M., Pedelty, J. A., Snyder, L. E., et al. 2003, ApJ, 588, 353
- Horn, A., Møllendal, H., Sekiguchi, O., et al. 2004, ApJ, 611, 605
- Hougen, J. T., Kleiner, I., & Godefroid, M. 1994, Journal of Molecular Spectroscopy, 163, 559
- Ilyushin, V., Kryvda, A., & Alekseev, E. 2009, Journal of Molecular Spectroscopy, 255, 32
- Kalenskii, S. V., & Johansson, L. E. B. 2010, Astronomy Reports, 54, 1084
- Kleiner, I. 2010, Journal of Molecular Spectroscopy, 260, 1
- Kobayashi, K., Ogata, K., Tsunekawa, S., & Takano, S. 2007, ApJ, 657, L17
- Kraemer, K. E., Jackson, J. M., & Lane, A. P. 1998, ApJ, 503, 785
- Langer, W. D., Graedel, T. E., Frerking, M. A., & Armentrout, P. B. 1984, ApJ, 277, 581
- Langer, W. D., & Penzias, A. A. 1990, ApJ, 357, 477
- . 1993, ApJ, 408, 539
- Liu, S., Girart, J. M., Remijan, A., & Snyder, L. E. 2002, ApJ, 576, 255
- Liu, S., Mehringer, D. M., & Snyder, L. E. 2001, ApJ, 552, 654
- Maeda, A., De Lucia, F. C., & Herbst, E. 2008a, Journal of Molecular Spectroscopy, 251, 293
- Maeda, A., Medvedev, I. R., De Lucia, F. C., Herbst, E., & Groner, P. 2008b, ApJS, 175, 138
- Margulès, L., Huet, T. R., Demaison, J., et al. 2010, ApJ, 714, 1120
- Mehringer, D. M., Snyder, L. E., Miao, Y., & Lovas, F. J. 1997, ApJ, 480, L71+
- Milam, S. N., Savage, C., Brewster, M. A., Ziurys, L. M., & Wyckoff, S. 2005, ApJ, 634, 1126
- Müller, H. S. P., Schlöder, F., Stutzki, J., & Winnewisser, G. 2005, Journal of Molecular Structure, 742, 215
- Müller, H. S. P., Thorwirth, S., Roth, D. A., & Winnewisser, G. 2001, A&A, 370, L49
- Neill, J. L., Steber, A. L., Muckle, M. T., et al. 2011, Journal of Physical Chemistry A, 115, 6472
- Neill, J. L., Bergin, E. A., Lis, D. C., et al. 2014, ApJ, 789, 8
- Oesterling, L. C., Albert, S., De Lucia, F. C., Sastry, K. V. L. N., & Herbst, E. 1999, ApJ, 521, 255
- Olmi, L., Cesaroni, R., Hofner, P., et al. 2003, A&A, 407, 225
- Persson, C. M., Olofsson, A. O. H., Koning, N., et al. 2007, A&A, 476, 807
- Pickett, H. M., Poynter, I. R. L., Cohen, E. A., et al. 1998, Journal of Quantitative Spectroscopy and Radiative Transfer, 60, 883
- Pickett, H. M., Poynter, R. L., & Cohen, E. A. 1992, NASA STI/Recon Technical Report N, 94, 13813
- Pratap, P., Megeath, S. T., & Bergin, E. A. 1999, ApJ, 517, 799
- Remijan, A., Shiao, Y., Friedel, D. N., Meier, D. S., & Snyder, L. E. 2004, ApJ, 617, 384
- Remijan, A., Snyder, L. E., Friedel, D. N., Liu, S., & Shah, R. Y. 2003, ApJ, 590, 314
- Remijan, A. J., Markwick-Kemper, A., & ALMA Working Group on Spectral Line Frequencies. 2007, BAAS, 38, 963
- Requena-Torres, M. A., Martín-Pintado, J., Rodríguez-Franco, A., et al. 2006, A&A, 455, 971
- Sato, M., Reid, M. J., Brunthaler, A., & Menten, K. M. 2010, ApJ, 720, 1055
- Savage, C., Apponi, A. J., Ziurys, L. M., & Wyckoff, S. 2002, ApJ, 578, 211
- Schilke, P., Groesbeck, T. D., Blake, G. A., & Phillips, T. G. 1997, ApJS, 108, 301

- Scoville, N., Kleinmann, S. G., Hall, D. N. B., & Ridgway, S. T. 1983, ApJ, 275, 201
- Senent, M. L., Villa, M., Meléndez, F. J., & Domínguez-Gómez, R. 2005, ApJ, 627, 567
- Shiao, Y., Looney, L. W., Remijan, A. J., Snyder, L. E., & Friedel, D. N. 2010, ApJ, 716, 286
- Snell, R. L., Scoville, N. Z., Sanders, D. B., & Erickson, N. R. 1984, ApJ, 284, 176
- Tercero, B., Cernicharo, J., & Pardo, J. R. 2005, in IAU Symposium, Vol. 235, IAU Symposium, 203P-+
- Tercero, B., Margulès, L., Carvajal, M., et al. 2012, A&A, 538, A119
- Tudorie, M., Ilyushin, V., Auwera, J. V., et al. 2012, J. Chem. Phys., 137, 064304
- Turner, B. E. 1991, ApJS, 76, 617
- Widicus Weaver, S. L., & Friedel, D. N. 2012, ApJS, 201, 16
- Willaert, F., Møllendal, H., Alekseev, E., et al. 2006, Journal of Molecular Structure, 795, 4
- Wilson, T. L. 1999, Reports on Progress in Physics, 62, 143
- Wilson, T. L., & Rood, R. 1994, ARA&A, 32, 191
- Wirström, E. S., Geppert, W. D., Hjalmarson, Å., et al. 2011, A&A, 533, A24
- Wouterloot, J. G. A., & Brand, J. 1996, A&AS, 119, 439
- Zernickel, A., Schilke, P., Schmiedeke, A., et al. 2012, A&A, 546, A87
- Ziurys, L. M., & McGonagle, D. 1993, ApJS, 89, 155